

USED FUEL DISPOSITION CAMPAIGN

Instrumentation: Nondestructive Examination for Verification of Canister and Cladding Integrity - FY2013 Status Update

Fuel Cycle Research & Development

*Prepared for
U.S. Department of Energy
Used Fuel Disposition Campaign*

*RM Meyer
AM Jones
AF Pardini
KM Denslow
SL Crawford
M Larche*

September 13, 2013

FCRD-UFD-2013-000337

PNNL-22734



DISCLAIMER

This information was prepared as an account of work sponsored by an agency of the U.S. Government. Neither the U.S. Government nor any agency thereof, nor any of their employees, makes any warranty, expressed or implied, or assumes any legal liability or responsibility for the accuracy, completeness, or usefulness, of any information, apparatus, product, or process disclosed, or represents that its use would not infringe privately owned rights. References herein to any specific commercial product, process, or service by trade name, trade mark, manufacturer, or otherwise, does not necessarily constitute or imply its endorsement, recommendation, or favoring by the U.S. Government or any agency thereof. The views and opinions of authors expressed herein do not necessarily state or reflect those of the U.S. Government or any agency thereof.

Reviewed by:

PNNL Project Manager

Signature on file

Brady Hanson

SUMMARY

This report documents FY13 efforts for two instrumentation subtasks under storage and transportation. These instrumentation tasks relate to developing effective nondestructive evaluation (NDE) methods and techniques to (1) verify the integrity of metal canisters for the storage of used nuclear fuel (UNF) and to (2) characterize hydrogen effects in UNF cladding to facilitate safe storage and retrieval. Efforts for the first task were focused on evaluating eddy current techniques for detecting and sizing stress corrosion cracks in canisters for UNF storage. In FY13, several specimens were collected that contained flaws for potential eddy current evaluation, and initial eddy current scans performed on these specimens indicate that eddy current is capable of detecting flaws that fall below the reliable detection limit for standard visual inspection technologies.

Finite element method (FEM) studies have been performed with the goal of identifying eddy current signal features that could be useful for characterizing stress corrosion cracking (SCC) flaws and to delineate the effects of notch depth, equivalent conductivity, and equivalent width based on models of SCC flaws proposed by Yusa and Miya (2009). In FY13, these studies focused on “short” notches (with aspect ratio of 3) and on the effects of notch depth and equivalent conductivity on eddy current signals. Several features were identified as candidate metrics for characterizing SCC flaws. Significant observations include:

- The location of the peak in normalized impedance curves with respect to frequency may be useful for characterizing the equivalent conductivity of a flaw. The frequency at which the peak exists appears to decrease with increasing conductivity.
- The location of zero crossings for change in normalized resistance (i.e., $\angle \Delta Z = 90^\circ$) versus frequency may be useful for characterizing the equivalent conductivity. The zero crossings are located at lower frequencies for 5 percent conductivity notches versus 0 percent conductivity notches.
- The existence and location of minimum values in the change in normalized resistance curves versus frequency may be useful for characterizing the equivalent conductivity of a flaw. For deeper flaws (i.e., 8.4 mm), this minima exists for 0-percent conductivity flaws but not 5-percent conductivity flaws.
- The phase angle of the change in normalized impedance indicates a monotonic behavior with respect to notch depth over the frequency range considered for 0-percent conductivity notches. However, for 5-percent conductivity notches, this trend is not as apparent.
- A metric defined as the ratio of the phase angle of the change in normalized impedance at 5 kHz to the phase angle of the change in normalized impedance at 100 kHz appears to provide a good discriminator of flaw conductivity regardless of notch depth.

Based on the results of the FEM analysis performed thus far, more studies should be performed to explore the following:

- Observe trends in eddy current probe signal features as a function of equivalent notch width and identify effective metrics for discriminating the effects of equivalent width from the effects of equivalent conductivity and notch depth.
- The intersection of the frequency sweep curves for both air-core and ferrite-core probes may provide useful information for the purposes of flaw characterization and should be explored more fully.

Instrumentation: Nondestructive Examination for Verification of Canister and Cladding Integrity – FY2013 Status Update

September 13, 2013

v

- The frequency sweep studies conducted thus far focused on “short” notches (i.e., aspect ratio of 3). Similar studies should be performed for “long” notches (i.e., notch length is much longer than notch depth or coil diameter).
- Extend the bounds of the frequency analysis to frequencies greater than 100 kHz and frequencies below 5 kHz.
- Explore the effectiveness of metrics for discriminating equivalent conductivity on a finer scale (i.e., discriminate between 0-percent and 1-percent equivalent conductivity or 1-percent and 2-percent equivalent conductivity, etc., or even finer scales).
- Explore other potential eddy current probe configurations such as the differential “plus-point” probe.

In addition to further FEM analysis, coils should be constructed to verify the findings of the FEM analysis conducted thus far on physical specimens and to verify that the model of SCC flaws proposed by (Yusa and Miya 2009) forming the basis of these studies is sufficient. In the case of atmospheric SCC flaw detection, more rigorous studies should be performed to quantify the reliability of eddy current techniques for detecting narrow SCC flaws, at least in the range of 0.016 mm to 0.030 mm crack opening displacement (COD), which is the range of median COD values observed for SCC flaw information obtained from failure analysis reports for the nuclear and non-nuclear industries (Wåle 2006). The extent to which FEM analysis can be leveraged to support this effort should be explored.

The status of FY13 efforts related to measurements of elastic properties of fuel cladding in an effort to characterize hydrogen effects is reflected in the bullets below. These bullets document several conclusions related to enhanced backscattering, resonant ultrasound spectroscopy (RUS), and Rayleigh velocity measurements performed or attempted in FY13:

- Enhanced backscattering was observed for a stainless steel tube specimen when immersed in multiple liquids.
- Backscatter peaks at the Rayleigh angle were not observed for Zr-4 tube specimens immersed in ethanol and water.
- The literature indicates that the amplitude of these backscatter peaks is dependent on the scattering inhomogeneity, perhaps caused by the surface roughness of the specimen or inherent material inhomogeneity in the specimen.
- Resonant ultrasound spectroscopy measurements performed on a parallelepiped specimen (UH06RM) of Zr-4 were consistent with vendor-provided specifications to within approximately 2.5% for the value of the stiffness coefficient c_{44} and within approximately 1.3% for Young’s modulus. However, larger discrepancies are observed for the c_{11} coefficient (approximately 5.6%) and the bulk modulus (approximately 8.7%).
- A tabulation of the measured dimensions and weights of nine initially prepared specimens exhibited considerable variability in the mass density calculated from those measurements. This indicates that the specimens exhibited significant deviations from ideal parallelepiped shapes and are a likely source of error observed.
- An apparatus and technique for performing Rayleigh velocity measurements on specimens has been demonstrated on a flat specimen of aluminum. The standard deviation of the measurements is reported to be on the order of 0.05 mm/ μ s.
- The literature indicates that ultrasonic velocity measurements have limited sensitivity to observe changes in hydrogen concentration with sensitivities on the order of 0.005 mm/ μ s change in velocity per 100 wppm of hydrogen concentration reported in the literature.

Based on these observations, several recommendations can be made with respect to future efforts.

Recommendations for future efforts include:

- Characterizing the surface roughness and microstructure of stainless steel and Zr-4 tube specimens used for enhanced backscatter measurements to determine if such measurements are feasible for Zr-4 materials (i.e., for instance, through appropriate surface polish or finish).
- Preparing better quality specimens for RUS measurements and exploring the possibility of performing RUS on more geometrically complex specimens (i.e., ring-shaped specimens representing cladding cross sections).
- Reducing the uncertainty in Rayleigh velocity measurements and attempting measurements on flat and tube-shaped Zr-4 specimens.
- Exploring the feasibility of performing $V(z)$ measurements of the Rayleigh velocity on specimens of interest, potentially using the same apparatus used for $V(x)$ measurements.
- Exploring non-linear Rayleigh wave measurements in an attempt to characterize hydrogen effects. Non-linear parameter measurements are typically more sensitive to distributed, pre-fracture forms of degradation than measurements of ultrasonic velocity.

CONTENTS

1.0	INTRODUCTION.....	1
1.1	Verification of Canister Integrity.....	1
1.2	Characterizing Hydrogen Effects in Cladding.....	2
1.3	Structure of Report.....	2
2.0	EDDY CURRENT FOR CANISTER EXAMINATIONS.....	3
2.1	Background Information.....	3
2.1.1	Eddy Current for SCC Depth Sizing.....	4
2.2	Collection of Specimens for Eddy Current Assessment.....	6
2.3	Finite Element Modeling.....	10
2.3.1	Initial Scoping Simulations.....	15
2.3.2	Parametric Analysis of Probe Parameters.....	19
2.3.3	Frequency Sweep Analysis.....	24
2.4	Summary of Accomplishments, Conclusions, and Future Efforts.....	32
3.0	CHARACTERIZING HYDROGEN EFFECTS IN CLADDING.....	35
3.1	Ultrasonic Characterization of Hydride Phenomena.....	36
3.2	Elastic Property Measurements.....	37
3.2.1	Rayleigh Wave Velocity.....	37
3.2.2	Enhanced Backscatter Effect.....	41
3.2.3	Resonant Ultrasound Spectroscopy.....	43
3.3	Status Update.....	44
3.3.1	Backscatter Measurements.....	44
3.3.2	Resonant Ultrasound Spectroscopy Measurements.....	50
3.3.3	Rayleigh Wave Velocity Measurements.....	55
3.4	Summary, Conclusions, and Future Efforts.....	58
4.0	REFERENCES.....	61
	Appendix A: Specimens for Eddy Current Evaluation.....	A.1
	Appendix B: Results of Parametric Study of Probe Dimensions.....	B.1
	Appendix C: Simulated Eddy Current Frequency Sweep Responses.....	C.1
	Appendix D: Zr-4 Tube Specimens.....	D.1

FIGURES

2.1. 2-dimensional “Ideal” Crack Approximation for Eddy Current Inversion (Bowler et al. 1994). Reprinted with permission from Bowler et al. (1994). Copyright 1994, AIP Publishing LLC.....	5
2.2. Highlighted Difference Between a Notch and Natural Crack (Yusa et al. 2002). Copyright 2002. Reprinted with permission from Elsevier.	6
2.3. Model of SCC Crack for Eddy Current Inversion (Yusa and Miya 2009). Copyright 2009. Reprinted with permission from Elsevier.	6
2.4. Example of a Plate Specimen (B-117) with a Thermal Fatigue Crack. The shows (a) the thermal fatigue crack, (b) an optical micrograph indicating that the crack has a crack opening displacement of 0.018 mm, (c) scanning of the specimen to obtain the eddy current image, and (d) the results of the eddy current scan.	8
2.5. Example of a Pipe Specimen (D-2) Containing an IGSCC Flaw Showing (a) the Original Pipe Specimen, (b) Removal of Section Containing Portion of IGSCC Flaw, (c) Optical Micrograph of the Crack, (d) Section of the Specimen with the Surface Shaved to Remove Effects of the Weld Geometry, and (e) Eddy Current Scan of the IGSCC Flaw with COD Estimated to be 220 μm	9
2.6. Depiction of the Case Study from Bowler et al. (1994) of a Pancake Coil over a Semi-Elliptical Notch Used to Benchmark FEM Described in this Section	10
2.7. Benchmark Comparison of FEM Results with Case Study for Semi-Elliptical Notch Considered in Bowler (1994). Reprinted with permission from Bowler (1994). Copyright 1994, AIP Publishing LLC.	12
2.8. Depiction of the Case Study from Bowler (1994) of A Pancake Coil over a Rectangular Notch Used to Benchmark FEM Described in this Section.....	13
2.9. Benchmark Comparison of FEM Results with Case Study Results for Rectangular Notch in Bowler et al. (1994). Reprinted with permission from Bowler et al. (1994). Copyright 1994, AIP Publishing LLC.	14
2.10. Benchmark Comparison of FEM Results with Case Study Results for Rectangular Notch in Burke (1988). With kind permission from Springer Science+Business Media © 1998: Burke (1988), 2.	15
2.11. Depiction of Notch Models Initially Explored Including Semi-Elliptical, Rectangular with Constant Length, and Rectangular with Aspect Ratio Held Constant at 3	16
2.12. Change in Resistance versus Notch Depth for Rectangular Notches of Constant Length for Frequencies of 500 Hz, 5 kHz, and 50 kHz	17
2.13. Change in Inductance versus Notch Depth for Rectangular Notches of Constant Length for Frequencies of 500 Hz, 5 kHz, and 50 kHz	17
2.14. Change in Impedance Phase Angle versus Notch Depth for Rectangular Notches of Constant Length for Frequencies of 500 Hz, 5 kHz, and 50 kHz	18
2.15. Change in Resistance versus Notch Depth for Rectangular Notches Aspect Ratio 3 for 5 kHz	18
2.16. Change in Resistance versus Notch Depth for Semi-Elliptical Notches of Aspect Ratio 3 for 5 kHz.....	19
2.17. Results of Parametric Analysis for 24 Variations of Probe Geometry Parameters for an Air-Core Probe over an Air-Filled Notch at 5 kHz	21

2.18. Results of Parametric Analysis for 24 Variations of Probe Geometry Parameters for an Air-Core Probe over an Air-Filled Notch at 50 kHz	21
2.19. Results of Parametric Analysis for 24 Variations of Probe Geometry Parameters for a Ferrite-Core Probe over an Air-Filled Notch at 5 kHz	22
2.20. Results of Parametric Analysis for 24 Variations of Probe Geometry Parameters for a Ferrite-Core Probe over an Air-Filled Notch at 50 kHz	22
2.21. Results of Parametric Analysis for 24 Variations of Probe Geometry Parameters for an Air-Core Probe over a Conductive Notch at 5 kHz.....	23
2.22. Results of Parametric Analysis for 24 Variations of Probe Geometry Parameters for an Air-Core Probe over a Conductive Notch at 50 kHz.....	23
2.23. Impedance Plane Representation of Signal Responses from 8.4-mm deep Notches. Frequency increases from 5 kHz to 100 kHz in the clockwise direction.....	25
2.24. Impedance Plane Representation of Signal Responses from 0% Conductivity Notches. Frequency increases from 5 kHz to 100 kHz in the clockwise direction.....	25
2.25. Impedance Plane Representation of Signal Responses from 5% Conductivity Notches. Frequency increases from 5 kHz to 100 kHz in the clockwise direction.....	26
2.26. Change in Normalized Impedance vs. Frequency for 8.4-mm Deep Notches	27
2.27. Change in Normalized Impedance vs. Frequency for 0% Conductivity Notches.....	27
2.28. Change in Normalized Impedance vs. Frequency for 5% Conductivity Notches.....	28
2.29. Change in Normalized Resistance vs. Frequency for 8.4-mm Deep Notches	29
2.30. Change in Normalized Resistance vs. Frequency for 0% Conductivity Notches	29
2.31. Change in Normalized Resistance vs. Frequency for 5% Conductivity Notches	30
2.32. Change in Impedance Phase Angle vs. Frequency for 8.4-mm Deep Notches.....	31
2.33. Change in Impedance Phase Angle vs. Frequency for 0% Conductivity Notches	31
2.34. Change in Impedance Phase Angle vs. Frequency for 5% Conductivity Notches	32
3.1. Depiction of (a) Circumferential Hydride Orientation and (b) Radial Hydride Orientation (Hanson et al. 2013).....	35
3.2. Illustration of Reflected Beam Components when the Incident Beam is at the Rayleigh Critical Angle. The two components include (1) a component of specular reflection and (2) a non-specular component associated with leaking Rayleigh waves (from Yu and Boseck 1995).....	39
3.3. Depiction of Double Ray Reflection Model for Scanning Acoustic Microscopy V(z) Scans (from Yu and Boseck 1995).....	40
3.4. Depiction of a V(z) Profile Obtained by Scanning Acoustic Microscopy Measurement (from Yu and Boseck 1995).....	40
3.5. Illustration of V(x) Method for Determination of V_R . Reprinted from Neuenschwander et al. (2006). Copyright (2006), with permission from Elsevier.....	41
3.6. Illustration of the Double-Peak Amplitude Profile as the Receiving Transducer is Scanned Along x. The first peak, Max 1, is associated with the component of specular reflection while the second peak, Max 2, is associated with the non-specular reflection component from leaky Rayleigh waves. Reprinted from Neuenschwander et al. (2006). Copyright (2006), with permission from Elsevier.	41

x

3.7. Depiction of Backscattering Peaks for Steel and Aluminum as Predicted by Nagy and Adler (1994). Reprinted with permission from Nagy and Adler (1994). Copyright 1994, Acoustical Society of America.	43
3.8. Depiction of Backscatter Measurements to Determine the Rayleigh Critical Angle for Tube Specimens	44
3.9. Photograph of Experimental Set-up Showing Placement of Specimen and Transducer in x-y Scanner of the SAM.....	45
3.10.SAM Images Obtained for Stainless Steel Specimen at 30 MHz (left) and 50 MHz (right)	45
3.11.SAM Image for Stainless Steel Specimen in Ethanol. The distance between backscatter peaks is measured across a section of the sample indicating a peak separation of 3.8 mm. Gating was adjusted for scans in ethanol to reduce the prominence of the reflection signal at normal incidence in the images.....	46
3.12.SAM Image for Stainless Steel Specimen in Water. The distance between backscatter peaks is measured across a section of the sample indicating a peak separation of 5.0 mm.	47
3.13.SAM Image Obtained for Zirc-4 Specimen 1a Immersed in Ethanol.....	48
3.14.SAM Image Obtained for Zirc-4 Specimen 2a Immersed in Ethanol.....	48
3.15.SAM Image for Stainless Steel Specimen in Bromobenzene	50
3.16.Photograph of Parallelepiped Specimens Fabricated from Zr-4 Plate (1.82 mm × 3 mm × 5 mm).....	51
3.17.Photograph of Zr-4 Coupons Prepared for Hydrogen Charging.....	51
3.18.Placement of Parallelepiped Specimen UH06RM between Piezoelectric Transducers for Performance of RUS Measurement	53
3.19.Example of Typical RUS Spectra Output; Obtained for Specimen UH1RM in this Case	54
3.20.Comparison of FEM Modeling Predictions for Location of Spectral Peaks with Experimental Observations	55
3.21.Apparatus for Performing Rayleigh Wave Velocity Measurements on Specimens	56
3.22.Persistence Scan of Scattered Profile for Flat Aluminum Specimen.....	57
3.23.Results of Two V(x) Scans Performed on Flat Aluminum Specimen. The slope of the curves represents the Rayleigh velocity (in./μsec.).....	57

TABLES

2.1. List of Specimens.....	7
2.2. List of Parameters for Semi-Elliptical Notch Case Study in Bowler et al. (1994)	11
2.3. List of Parameters for Rectangular Notch Case Study in Bowler (1994) and Burke (1988).....	13
2.4. Summary of Parameters Considered in Parametric Studies.....	20
2.5. Summary of Cases Exhibiting the Best or Nearly the Best Sensitivity for One or More of the Scenarios Simulated.....	24
2.6. Summary of Locations of Change in Normalized Impedance Maxima.....	28
2.7. Summary of Zero Crossing Locations for Change in Normalized Resistance vs. Frequency	30
2.8. Ratio of Change in Impedance Phase Angle at 5 kHz to Change in Impedance Phase Angle at 100 kHz.....	32
3.1. Summary of Backscatter Peak Analysis for Stainless Steel Specimen in Water and Ethanol.....	47
3.2. Summary of Relevant Properties for Potential Immersion Fluids (source: Cheeke 2002).....	49
3.3. Tabulation of Zr-4 Samples <i>Not</i> Charged with Hydrogen.....	52
3.4. Tabulation of c11 and c44 Measurements and Values of c11 and c44 from Vendor Specifications.....	55
3.5. Summary of V(x) Scan Data for a Flat Aluminum Specimen	58

ACRONYMS

ATI	Allegheny Technologies Inc.
COD	crack opening displacement
DCSS	dry cask storage system
DOE	U.S. Department of Energy
EDM	electro-discharge machined
FEM	finite element method
HR	hydride rims
IGSCC	intergranular stress corrosion crack
LUT	laser ultrasound technique
NDE	nondestructive evaluation
RI	resonant inspection
RUS	resonant ultrasound spectroscopy
SAM	scanning acoustic microscope
SCC	stress corrosion cracking
UFDC	Used Fuel Disposition Campaign
UNF	used nuclear fuel

Instrumentation: Nondestructive Examination for Verification of Canister and Cladding Integrity – FY2013 Status Update

1.0 INTRODUCTION

The U.S. Department of Energy (DOE) Office of Nuclear Energy, Office of Fuel Cycle Technology has established the Used Fuel Disposition Campaign (UFDC) to conduct the research and development activities related to storage, transportation, and disposal of used nuclear fuel (UNF) and high-level radioactive waste. Within the UFDC, the storage and transportation task has been created to address issues of extended or long-term storage and transportation. The near-term objectives of the storage and transportation task are to use a science-based, engineering-driven approach to

- develop the technical bases to support the continued safe and secure storage of UNF for extended periods
- develop the technical bases for retrieval of UNF after extended storage
- develop the technical bases for transport of high burn-up fuel, as well as low and high burn-up fuel after dry storage.

This report documents FY13 efforts for two instrumentation subtasks under storage and transportation. These instrumentation tasks relate to developing effective nondestructive evaluation (NDE) methods and techniques to (1) verify the integrity of metal canisters for the storage of UNF and (2) characterize hydrogen effects in UNF cladding to facilitate safe storage and retrieval.

1.1 Verification of Canister Integrity

A gap analysis report recently performed under the DOE's UFDC highlighted monitoring of dry cask storage systems (DCSSs) as a high-priority gap area to ensure the safe long-term storage of UNF (Hanson et al. 2012). Canister-based DCSSs for UNF are one of the two main types of designs for DCSSs of UNF. In these types of systems, UNF assemblies are loaded into a basket that is integrated into a relatively thin-walled cylindrical container (canister) that is then placed into a metal or concrete overpack. Most of the DCSSs in service in the United States use designs based on a separate welded canister placed inside of an overpack (Hanson et al. 2012). Atmospheric stress corrosion cracking (SCC) is considered a potential form of degradation in DCSS canisters located in coastal areas. Chloride deposits, in combination with a source of stress and susceptible material, provide the conditions necessary for atmospheric SCC to occur. Although no instances of atmospheric SCC in DCSS canisters have been reported, instances of similar degradation in other components in the nuclear power industry have been observed (NRC 2011) and experimental investigations to date have not been able to rule out the possibility of atmospheric SCC occurring in DCSS canisters located in coastal environments (Caseres and Mintz 2010).

Several NDE methods/techniques were considered in a review of methods and techniques for inspecting DCSS canisters including visual, bulk ultrasound, acoustic emission, guided ultrasonic waves, and eddy current (Meyer et al. 2013). A review of the current state of acoustic emission and guided ultrasonic wave technologies based on open literature indicates that further research and development is

required to determine or improve the efficacy of these techniques for atmospheric SCC detection in DCSS canisters. Also, assessments performed of the reliability of visual inspections for nuclear reactor applications indicates that many SCC flaws can have crack-opening displacements (CODs) that are too small to be detected reliably using cameras with specifications equivalent to what is commonly used in the field (Cumblidge et al. 2004; Cumblidge et al. 2007). Thus, at least in the near term, eddy current and bulk ultrasound techniques may be most viable for performing effective inspections of DCSS canisters. A part of this work focuses on the application of eddy current to the detection and sizing of flaws on the outside surface of DCSS canisters.

1.2 Characterizing Hydrogen Effects in Cladding

The absorption of hydrogen by fuel cladding during the course of reactor operation may result in compromised integrity of the fuel cladding, resulting in less resistance to failure under dry storage and transportation conditions. Two important effects of hydrogen absorption include the (1) reorientation of hydrides that precipitate in the cladding material above saturation and (2) formation of dense hydride rims near the outer diameter of the cladding. It has been shown that, at high temperatures and stress, the normally circumferential hydrides found in high burn-up cladding can reorient in the radial direction (Billone et al. 2008; Billone et al. 2013). Because the fracture resistance will be less in the direction of the hydride orientations, radially oriented hydrides could facilitate crack propagation through the cladding thickness. In addition, a comparison of cladding of high burn-up fuel with unirradiated specimens charged to approximately equal total hydrogen content showed significant differences in hydride distribution. Whereas the hydride distribution in unirradiated specimens was uniform, the hydride distribution in cladding of high burn-up fuel was uneven, with a much higher concentration near the cladding outer diameter (a hydride rim) (Billone et al. 2013). This region of dense hydride concentration is more brittle in nature than other areas of the cladding facilitating crack initiation. The ability to characterize these hydrogen effects (namely, hydride orientation and distribution) in fuel cladding would enable more effective management of UNF to ensure the safety of UNF for extended storage periods. Therefore, several techniques are investigated for effectively characterizing these hydrogen effects in fuel cladding through measurements of elastic properties.

1.3 Structure of Report

The rest of this report is organized into two sections with Section 2.0 devoted to summarizing FY13 efforts and progress related to investigating eddy current techniques for detecting and characterizing SCC flaws in canisters for UNF storage and Section 3.0 devoted to summarizing FY13 efforts and progress related to characterizing hydrogen effects in cladding based on measurements of elastic properties. The basic structure of each section includes (1) background material; (2) presentation of results; and (3) conclusions, summary of accomplishments, and recommendations for future efforts. In this respect, conclusions, summary of accomplishments, and recommendations for future efforts related the application of eddy current techniques for detecting and characterizing SCC flaws in canisters for UNF storage are included in Section 2.4, while analogous information for the task related to characterizing hydrogen effects through elastic property measurements is included in Section 3.4.

2.0 EDDY CURRENT FOR CANISTER EXAMINATIONS

This section documents FY13 efforts with respect to use of eddy current for nondestructive evaluation (NDE) of dry cask storage system (DCSS) canisters. The motivation of this effort is outlined in the introduction. Some brief background information is provided in Section 2.1 to define parameters related to eddy current probe responses, which the reader can refer to when reviewing results from finite element method (FEM) simulations presented in Section 2.3. In addition, Section 2.1 includes a summary of literature related to depth sizing of stress corrosion cracking (SCC) flaws in thick components. Section 2.2 discusses the collection of specimens for potential benchmarking and validating of FEM model results and also presents some detection results. Finally, Section 2.4 provides a brief summary of accomplishments and conclusions based on FY13 efforts and makes recommendations for future research efforts.

2.1 Background Information

The interaction of eddy current fields with defects is governed by a vector diffusion equation, with the depth of penetration of the fields determined by the diffusion length, or skin depth of the field. The skin depth is represented by

$$\delta = \sqrt{\frac{1}{\pi f \sigma \mu}}, \quad (2.1)$$

where f is the frequency of the exciting eddy current field, σ is the conductivity of the test material, and μ is the magnetic permeability of the test material. Detection of defects or flaws in test materials is based on changes in the impedance of an exciting eddy current coil that manifests as a result of the interaction of the eddy current field with impedance discontinuities in the test material. The change in impedance, ΔZ , is measured by subtracting the impedance of the coil for some baseline condition, Z_0 , from the impedance observed for the defect, Z_1 , where

$$Z_0 = R_0 + jX_0, \quad (2.2)$$

$$Z_1 = R_1 + jX_1, \quad (2.3)$$

$$\Delta Z = Z_1 - Z_0 = (R_1 - R_0) + j(X_1 - X_0). \quad (2.4)$$

In these equations, R_0 and R_1 represent the resistive components of Z_0 and Z_1 while X_0 and X_1 represent the reactive components of Z_0 and Z_1 , which are inductive in nature; thus,

$$X_0 = \omega L_0, \text{ and} \quad (2.5)$$

$$X_1 = \omega L_1, \quad (2.6)$$

where L_0 is the coil inductance measured for the baseline condition and L_1 is the coil inductance measured for the defect condition. The impedance measurements can be separated into components including the

4

resistive part, $Re(\Delta Z)$; reactive part, $Im(\Delta Z)$; the impedance magnitude, $|\Delta Z|$; and the impedance phase angle, $\angle \Delta Z$, where

$$Re(\Delta Z) = \Delta R = R_1 - R_0, \quad (2.7)$$

$$Im(\Delta Z) = \Delta X = X_1 - X_0, \quad (2.8)$$

$$|\Delta Z| = \sqrt{Re(\Delta Z)^2 + Im(\Delta Z)^2}, \quad (2.9)$$

$$\angle \Delta Z = Tan^{-1} \left(\frac{Re(\Delta Z)}{Im(\Delta Z)} \right). \quad (2.10)$$

In Section 2.3.1, results are presented as percentages of changes observed in the resistance, $\Delta R\%$, and inductance, $\Delta L\%$, where

$$\Delta R\% = \frac{R_1 - R_0}{R_0} \times 100, \quad (2.11)$$

$$\Delta L\% = \frac{L_1 - L_0}{L_0} \times 100. \quad (2.12)$$

In Sections 2.3.2 and 2.3.3, the eddy current responses are presented as normalized variables, normalized to the reactance of the baseline scenario, X_0 . As such, the change in normalized impedance, change in normalized resistance, and normalized reactance are defined as follows:

$$\text{change in normalized impedance} = \frac{\Delta Z}{X_0} = \frac{Z_1 - Z_0}{X_0} = \frac{\sqrt{(\Delta R)^2 + (\Delta X)^2}}{X_0} \quad (2.13)$$

$$\text{change in normalized resistance} = \frac{\Delta R}{X_0} = \frac{R_1 - R_0}{X_0} \quad (2.14)$$

$$\text{change in normalized reactance} = \frac{\Delta X}{X_0} = \frac{X_1 - X_0}{X_0} \quad (2.15)$$

2.1.1 Eddy Current for SCC Depth Sizing

Crack sizing and characterization based on eddy current signals is an inverse problem that is normally handled through iterative solutions to a forward model until an error function is minimized or decreases below a defined threshold. A review of eddy current modeling and inversion is provided by Auld and Moulder (1999). Analytical solutions to the forward model are available for simple flaw geometries in the thin skin depth or thick skin depth limits (skin depth is much less or much greater than the flaw depth, respectively). Numerical (finite element, finite difference, boundary element, etc.) techniques enable

modeling of more complex flaw geometries and arbitrary skin depth to flaw dimension ratios and many of the initial efforts focused on “ideal crack” approximations, which assume the flaw region is defined as having zero width (2-dimensional) and zero conductivity (see Figure 2.1) (Bowler 1994; Bowler et al. 1994; Bowler 2002).

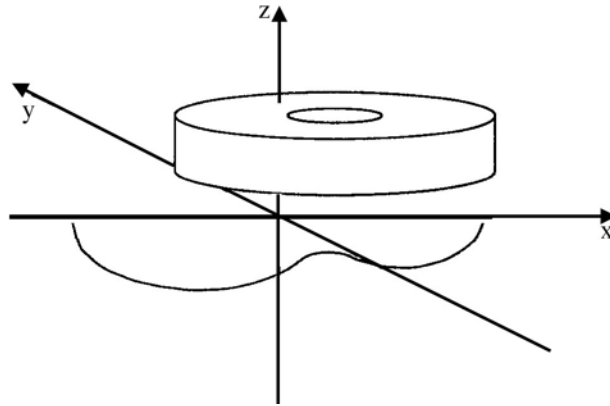


Figure 2.1. 2-dimensional “Ideal” Crack Approximation for Eddy Current Inversion (Bowler et al. 1994). Reprinted with permission from Bowler et al. (1994). Copyright 1994, AIP Publishing LLC.

Real cracks deviate from the ideal crack assumptions of zero width and zero conductivity (Beissner 1994). The deviation from zero conductivity is caused by partial contact between crack faces providing conduits for the flow of current through the crack plane (see Figure 2.2). Reconstruction techniques have been proposed to characterize SCC flaws in pressurized water reactor (PWR) steam generator tubes. These techniques model the crack profiles as assemblies of discretized regions of fixed width. In Huang and Takagi (2002), the crack region is assumed to be non-conducting, while Yusa et al. (2003) associate non-zero conductivity values with each discretized region. Reconstructed SCC flaw profiles are described as agreeing reasonably well with natural crack profiles for each of these techniques, although, in the case of assumed zero conductivity, a consistent under-sizing of crack depth is reported (Huang and Takagi 2002). Later studies have shown that it is necessary to model stress corrosion cracks as conductive regions for accurate characterization (Yusa et al. 2007b).

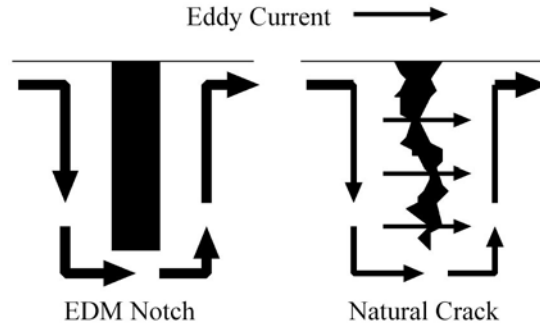


Figure 2.2. Highlighted Difference Between a Notch and Natural Crack (Yusa et al. 2002). Copyright 2002. Reprinted with permission from Elsevier.

An alternative model of real cracks is considered in which the cracks are defined as rectangular-shaped regions with a uniformly distributed non-zero conductivity and significant width dimension (i.e., a 3-dimensional profile) as illustrated in Figure 2.3 (Yusa and Miya 2009). The complexity introduced by requiring determination of equivalent width and equivalent conductivity in addition to depth results in an ill-posed problem, and accurate determination of depth may not be possible without additional information that may come from multiple eddy current measurements or using multiple NDE modalities (Yusa et al. 2007a).

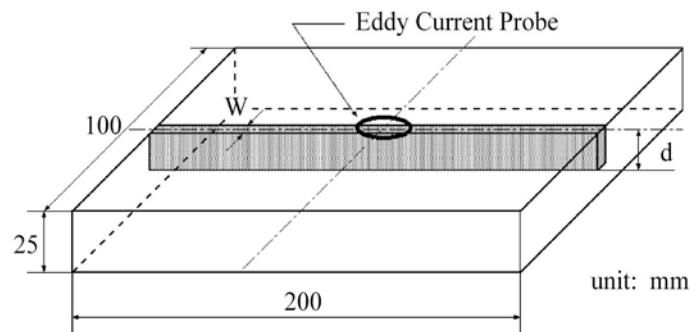


Figure 2.3. Model of SCC Crack for Eddy Current Inversion (Yusa and Miya 2009). Copyright 2009. Reprinted with permission from Elsevier.

2.2 Collection of Specimens for Eddy Current Assessment

To facilitate verification of eddy current and other proposed NDE methods or techniques for detection and characterization of flaws in DCSS canisters, it is necessary to identify specimens that adequately simulate the target inspection scenarios. For this purpose, several 304 stainless steel specimens with intergranular stress corrosion crack (IGSCC), thermal fatigue, or electro-discharge machined (EDM) flaws were collected from round-robin studies performed to assess the reliability of ultrasonic testing methods and techniques (Heasler et al. 1990; Heasler and Doctor 1996; Heasler and Doctor 2003). A list of collected specimens is provided in Table 2.1, which includes information about flaw type, material,

specimen geometry, and thickness. Although it is not indicated in the table, the pipe specimens were much smaller in diameter than a typical DCSS container, with pipe diameters as small as 10 inches.

Table 2.1. List of Specimens

Sample ID	Material	Type	Geometry	Wall (mm)	Flaw Type
EDM	SS	304	Plate	15.2	EDM Notch
B-211	SS	304	Pipe	12.5	Thermal Fatigue
B-212	SS	304	Pipe	12.5	Thermal Fatigue
B-213	SS	304	Pipe	12.5	Thermal Fatigue
B-214	SS	304	Pipe	12.5	Thermal Fatigue
B-215	SS	304	Pipe	12.5	Thermal Fatigue
B-216	SS	304	Pipe	12.5	Thermal Fatigue
B-217	SS	304	Pipe	12.5	IGSCC
D-101	SS	304	Pipe	14.0	IGSCC
D-102	SS	304	Pipe	14.0	IGSCC
D-105	SS	304	Pipe	14.0	IGSCC
D-107	SS	304	Pipe	14.0	IGSCC
D2	SS	304	Pipe	17.5	IGSCC
D3	SS	304	Pipe	17.5	IGSCC
D4	SS	304	Pipe	17.5	IGSCC
D5	SS	304	Pipe	17.5	IGSCC
B-117	SS	304	Plate	16.4	Thermal Fatigue
B-118	SS	304	Plate	15.3	Thermal Fatigue
07-343	SS	304L	Plate	12.3	Crack (unknown)

Examples of typical plate and pipe specimens are included in Figures 2.4 and 2.5, respectively. The plate specimen (B-117) contained thermal fatigue cracks and viewing under an optical microscope revealed that the main thermal fatigue crack had a crack opening displacement (COD) of approximately 0.018 mm. The eddy current image in Figure 2.4(d) was obtained using the configuration indicated in Figure 2.4(c) of the figure while scanning at a speed of 25.4 mm/s (1 in./s) using a pancake coil probe with inner diameter of 0.5 mm (0.02 in.) and an outer coil diameter of 1.57 mm (0.062 in.). The coil was wound around a ferrite core and the probe was operated at 6 MHz. The significance of this is that it demonstrates the capability of eddy current to detect cracks that are too narrow to detect reliably using standard visual testing technology. Assessments of visual testing have documented that the reliability of visual testing begins to drop for cracks with CODs below 0.1 mm, and that below 0.02 mm, cracks are very difficult to detect even under favorable conditions (Cumblidge et al. 2004; Cumblidge et al. 2007). A review of several failure analysis reports found that SCC flaws observed in nuclear and non-nuclear industries have median CODs in the range of 0.016 mm to 0.03 mm (Wåle 2006). To the best of the authors' knowledge, no eddy current reliability studies have been performed with respect to the COD parameter of cracks. An effort to determine the reliability of eddy current techniques to detect cracks with CODs at or below these values would be beneficial to the given application.

8

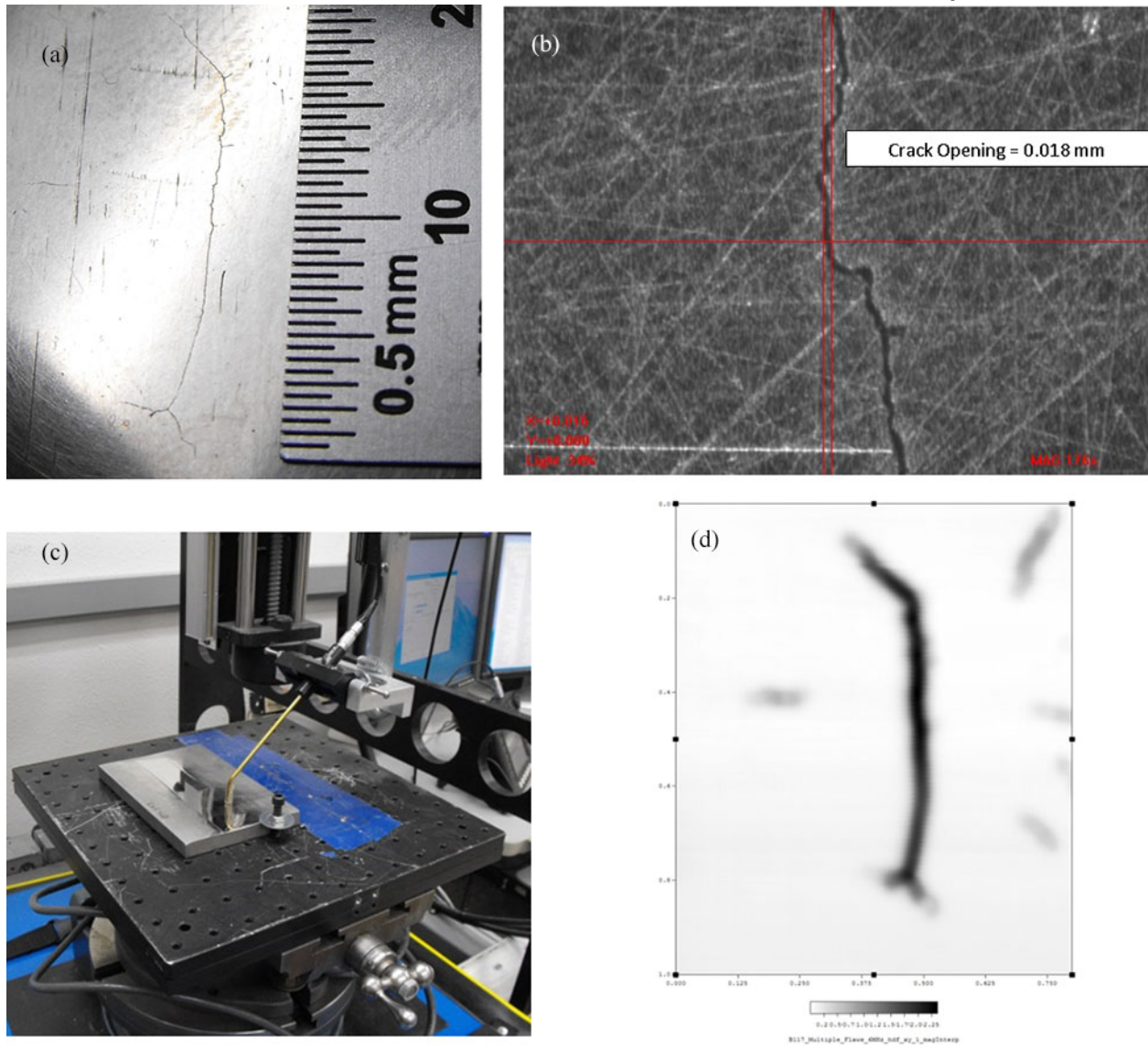


Figure 2.4. Example of a Plate Specimen (B-117) with a Thermal Fatigue Crack. The figure shows (a) the thermal fatigue crack, (b) an optical micrograph indicating that the crack has a crack opening displacement of 0.018 mm, (c) scanning of the specimen to obtain the eddy current image, and (d) the results of the eddy current scan.

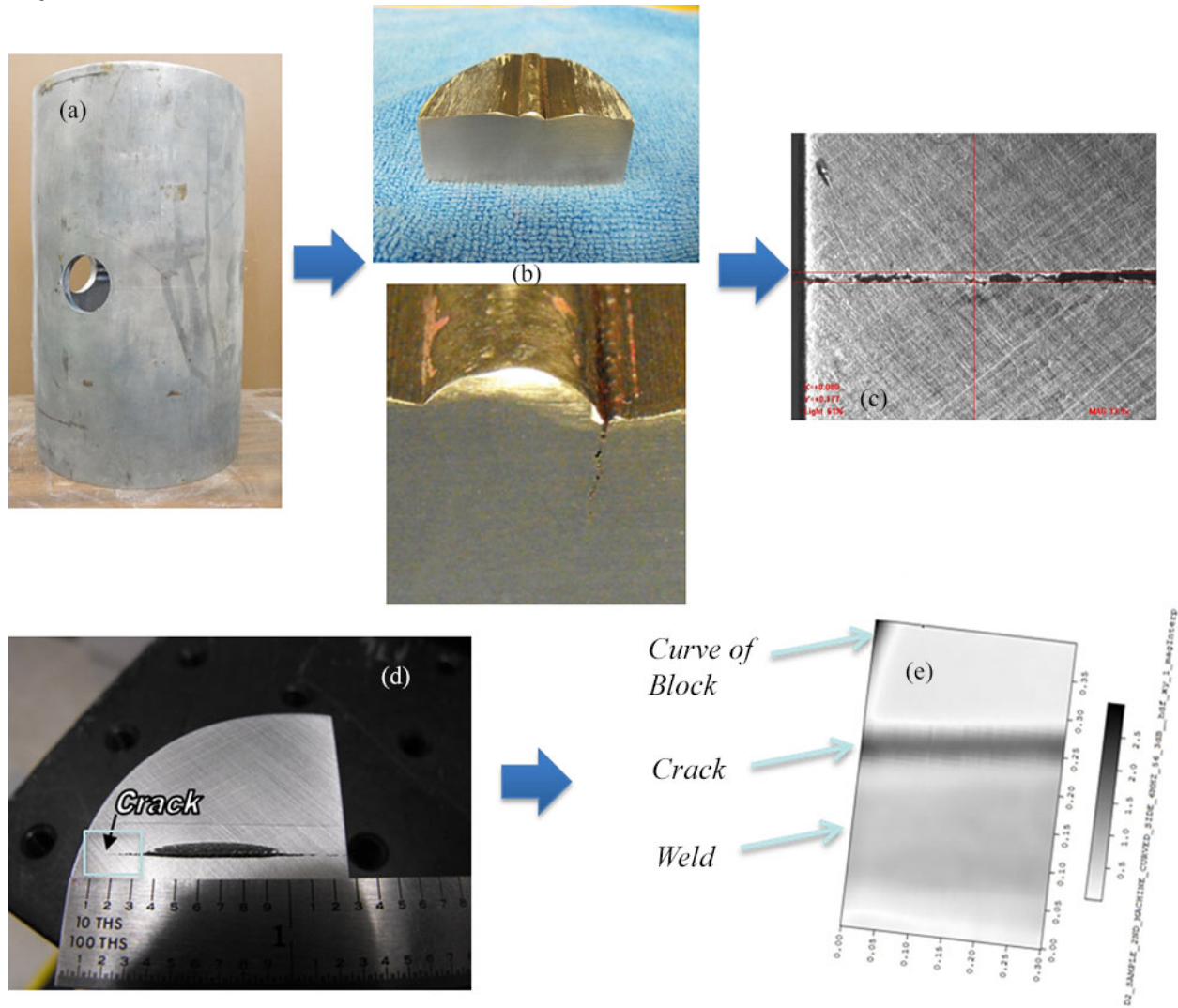


Figure 2.5. Example of a Pipe Specimen (D-2) Containing an IGSCC Flaw Showing (a) the Original Pipe Specimen, (b) Removal of Section Containing Portion of IGSCC Flaw, (c) Optical Micrograph of the Crack, (d) Section of the Specimen with the Surface Shaved to Remove Effects of the Weld Geometry, and (e) Eddy Current Scan of the IGSCC Flaw with COD Estimated to be 220 μm

Specimen D-2, a pipe specimen with an IGSCC crack, was also scanned. In this case, eddy current scanning was performed on a circular section removed from the weld of the pipe (see Figure 2.5). The specimen surface was shaved flat, removing the weld profile (Figure 2.5(d)). In this case, the COD of the IGSCC flaw was estimated at 0.22 mm based on optical microscope measurements. Appendix A includes a compilation of several more specimens including photos, illustrations of flaw locations and dimensions, and the results of eddy current scans.

2.3 Finite Element Modeling

Finite element modeling has been performed in an initial assessment of the potential for sizing defects from eddy current probe measurement signals. These efforts began with consideration of air-filled notches and pancake coil-style probes with air-filled cores. The model is initially benchmarked with measurements and boundary element modeling solutions for a semi-elliptical notch provided in Bowler et al. (1994). A depiction of the case study in Bowler et al. (1994) is provided in Figure 2.6. Table 2.2 summarizes the parameters assumed for the coil and for the flaw specimen, and the results of the FEM modeling are displayed side-by-side with measurements and modeling results reported in Bowler et al. (1994) in Figure 2.7 indicating reasonable agreement.

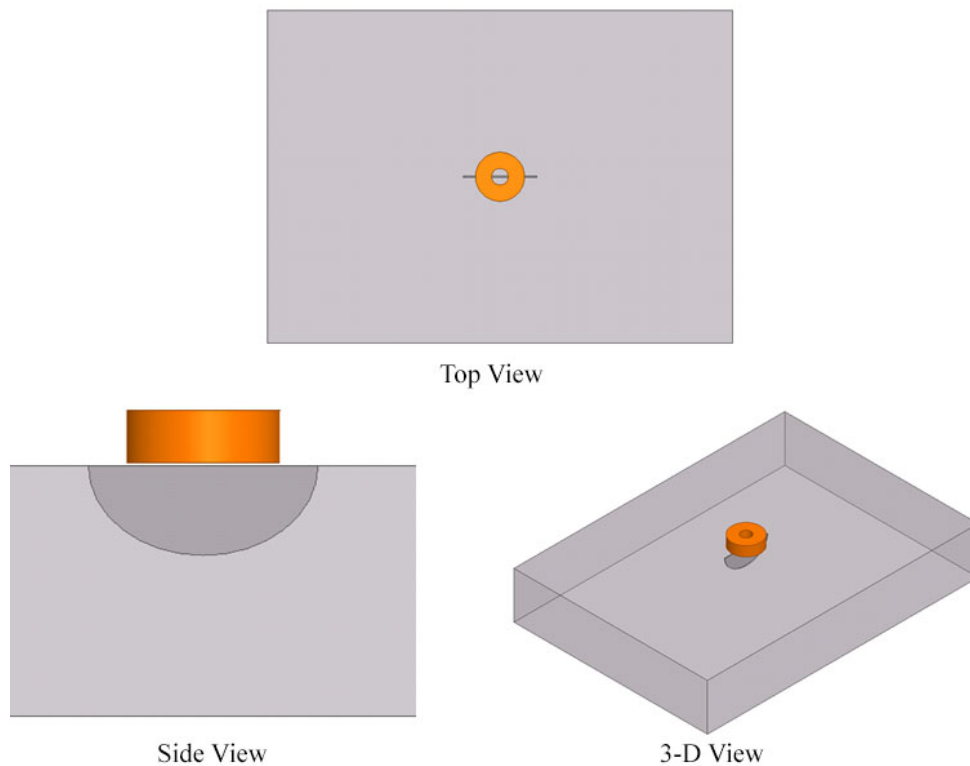


Figure 2.6. Depiction of the Case Study from Bowler et al. (1994) of a Pancake Coil over a Semi-Elliptical Notch Used to Benchmark FEM Described in this Section

The FEM model was also benchmarked for rectangular-shaped notches using the benchmark data provided in Bowler (1994) and Burke (1988). A depiction of the case study for rectangular notches is provided in Figure 2.8 and the parameters of the rectangular notch case study are provided in Table 2.3. Results for the FEM simulations for the rectangular notch case study are compared with results reported in in Bowler (1994) and Burke (1988) in Figures 2.9 and 2.10, respectively, demonstrating reasonably good agreement.

Table 2.2. List of Parameters for Semi-Elliptical Notch Case Study in Bowler et al. (1994)

Probe Parameters	
Inner radius	2.51 ± 0.01 mm
Outer radius	7.38 ± 0.01 mm
Height	4.99 ± 0.01 mm
Lift-off	0.313 ± 0.01 mm
Frequency	350 Hz
Specimen Parameters	
Conductivity	22.62 ± 0.06 MS/m
Thickness	24 mm
Flaw shape	Semi-elliptical
Flaw length	22.1 ± 0.02 mm
Flaw depth	8.61 ± 0.05 mm
Flaw width	0.33 ± 0.01 mm

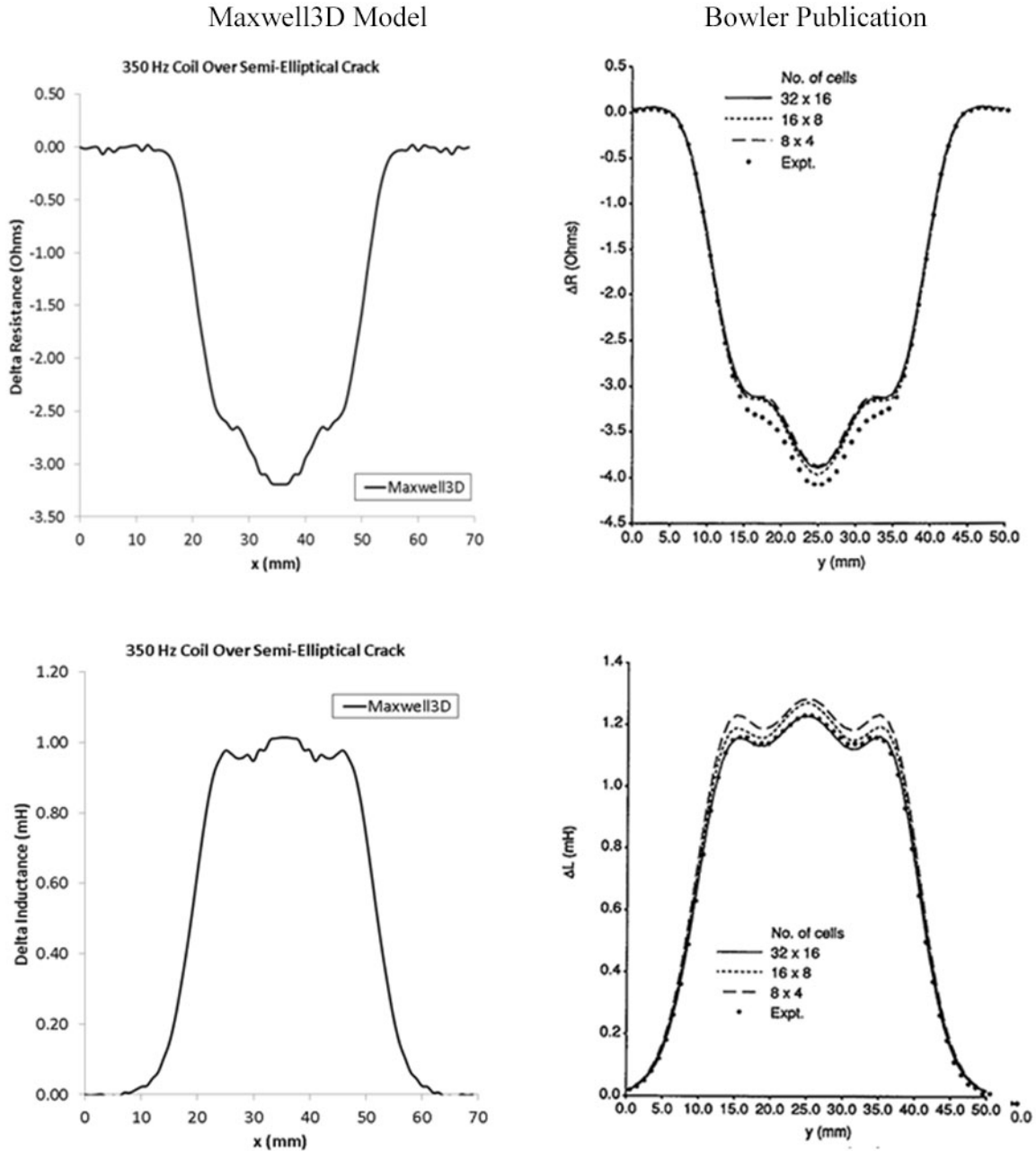


Figure 2.7. Benchmark Comparison of FEM Results with Case Study for Semi-Elliptical Notch Considered in Bowler (1994). Reprinted with permission from Bowler (1994). Copyright 1994, AIP Publishing LLC.

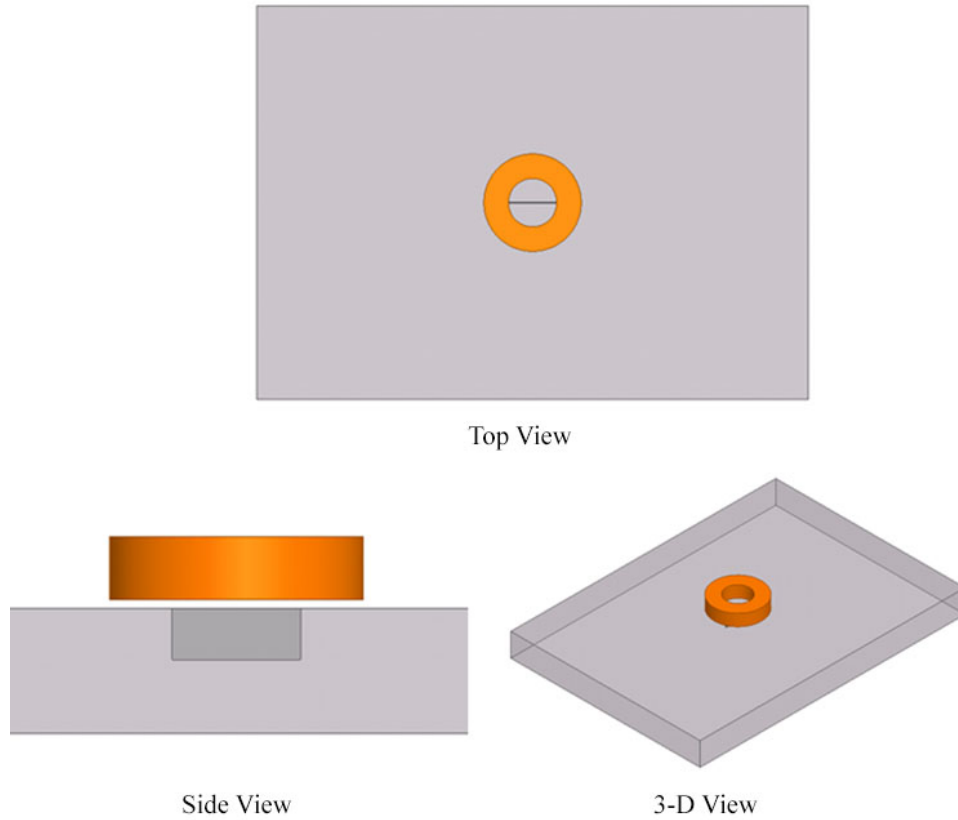


Figure 2.8. Depiction of the Case Study from Bowler (1994) of A Pancake Coil over a Rectangular Notch Used to Benchmark FEM Described in this Section

Table 2.3. List of Parameters for Rectangular Notch Case Study in Bowler (1994) and Burke (1988)

Probe Parameters	
Inner radius	6.15 ± 0.05 mm
Outer radius	12.4 ± 0.05 mm
Height	6.15 ± 0.01 mm
Lift-off	0.88 mm
Frequency	900 Hz
Specimen Parameters	
Conductivity	30.6 ± 0.02 MS/m
Thickness	12.22 ± 0.02 mm
Flaw shape	Rectangular
Flaw length	12.6 ± 0.02 mm
Flaw depth	5.0 ± 0.05 mm
Flaw width	0.28 ± 0.01 mm

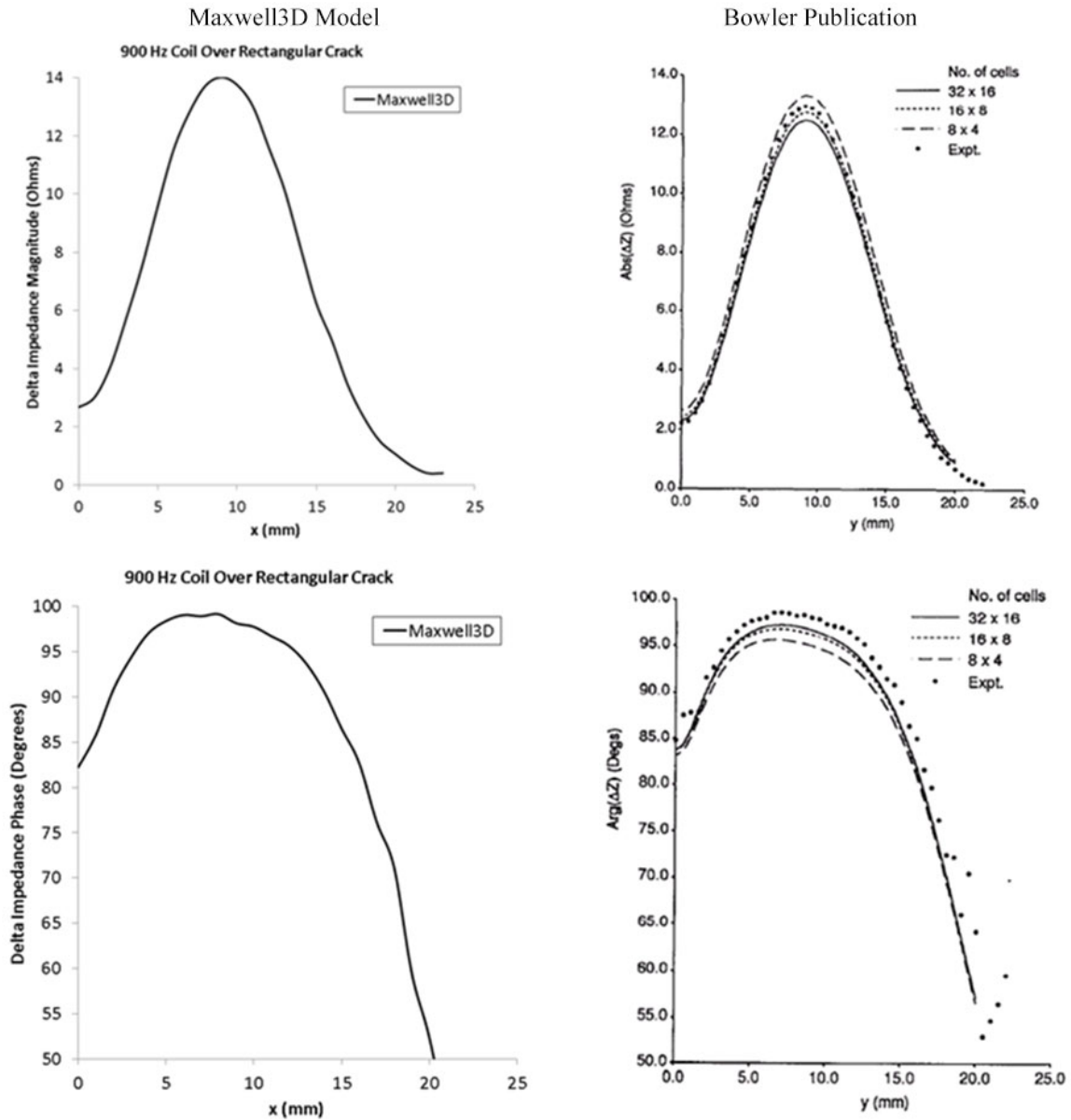


Figure 2.9. Benchmark Comparison of FEM Results with Case Study Results for Rectangular Notch in Bowler et al. (1994). Reprinted with permission from Bowler et al. (1994). Copyright 1994, AIP Publishing LLC.

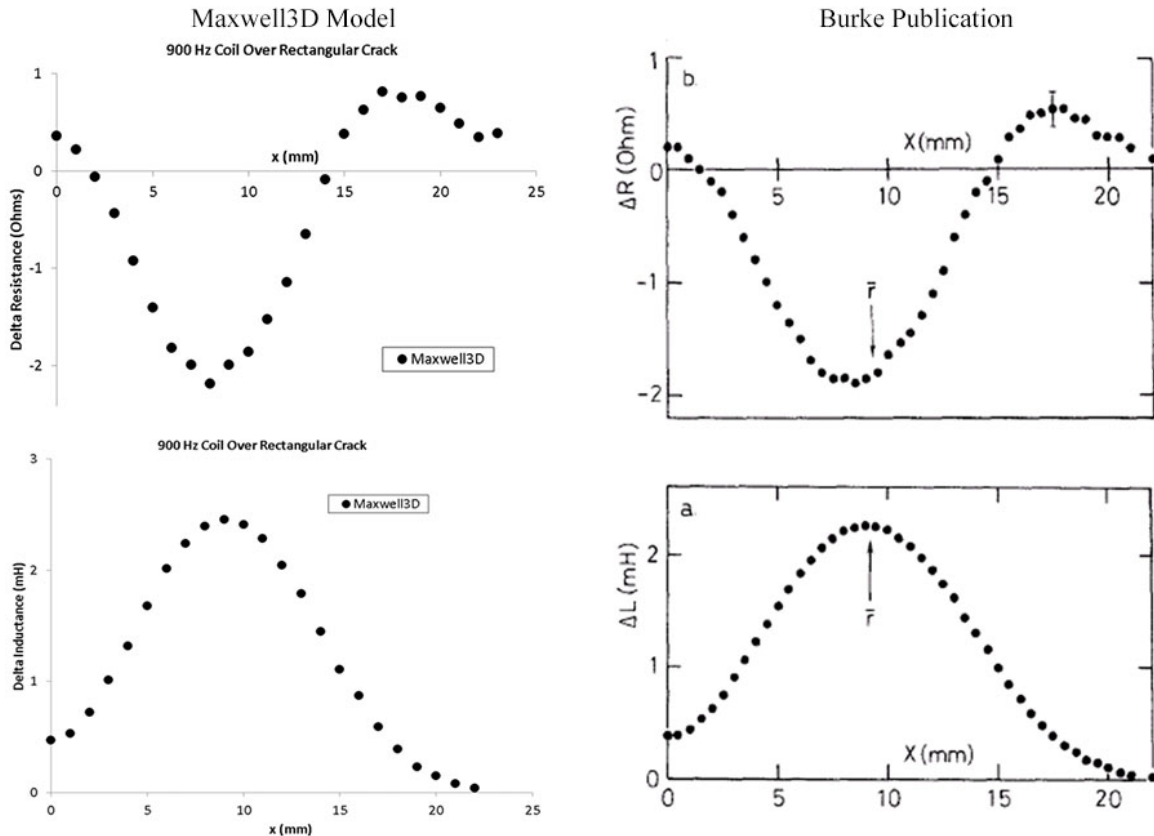


Figure 2.10. Benchmark Comparison of FEM Results with Case Study Results for Rectangular Notch in Burke (1988). With kind permission from Springer Science+Business Media © 1998: Burke (1988), Figure 2.

2.3.1 Initial Scoping Simulations

Simulations were conducted to observe the relationship between measurement signals and notch depth, considering rectangular-shaped notches of constant length, rectangular-shaped notches of constant aspect ratio (equal to 3), and semi-elliptical notches. Depictions of the different notch types (i.e., semi-elliptical, rectangular constant length, and rectangular with constant aspect ratio of 3) are included in Figure 2.11. Simulations were performed using probe dimensions summarized in Table 2.2. Profiles of signal amplitude versus notch depth are included in Figures 2.12 through 2.14 for rectangular notches of constant length showing the change in resistance, inductance, and phase angle versus notch depth for frequencies of 500 Hz, 5 kHz, and 50 kHz. The probe is positioned to achieve maximum change in signal amplitude. At 5 kHz, the resistance exhibits a monotonic trend of signal amplitude versus notch depth with approximately 1% change in resistance per 1 mm of notch depth, in this case. Figures 2.15 and 2.16 display the amplitude of the resistance versus notch depth for semi-elliptical and rectangular notches with aspect ratios of 3. Although there are some minor variations in shapes, the curves are similar to the curve for rectangular notches of constant length, exhibiting monotonic behavior and approximately 1% change in signal per 1 mm of notch depth.

Generally, all signals for the frequencies considered exhibit some monotonic relationship over a limited range of flaw depth. Even at 500 Hz, a monotonic relationship is observed for notches up to 2 mm in depth. The information provided by signals at several frequencies may be useful in enabling a characterization of SCC flaw depth. For instance, Figure 2.12 shows that the change in AC resistance increases with frequency for a given notch depth from 500 Hz to 50 kHz for notches less than 6 mm in depth. However, for notches greater than 6 mm in depth, Figure 2.12 indicates that the change in AC resistance peaks between 500 Hz and 50 kHz for a notch of given depth.

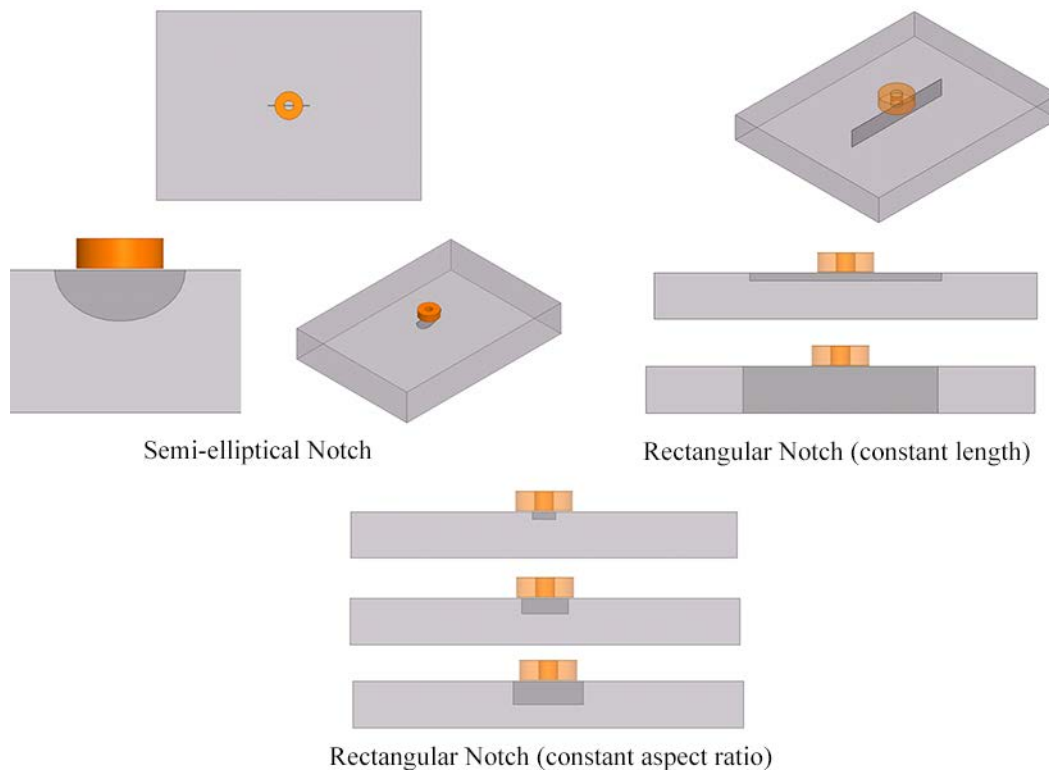


Figure 2.11. Depiction of Notch Models Initially Explored Including Semi-Elliptical, Rectangular with Constant Length, and Rectangular with Aspect Ratio Held Constant at 3

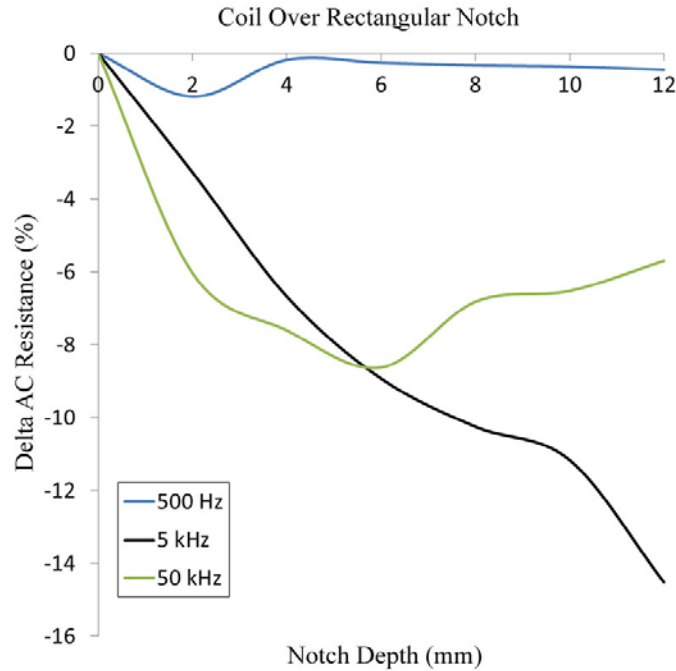


Figure 2.12. Change in Resistance versus Notch Depth for Rectangular Notches of Constant Length for Frequencies of 500 Hz, 5 kHz, and 50 kHz

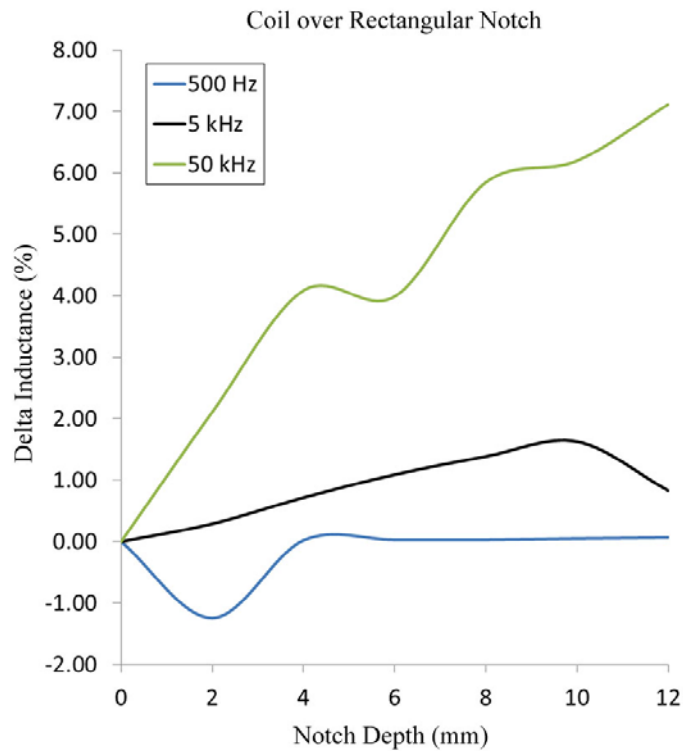


Figure 2.13. Change in Inductance versus Notch Depth for Rectangular Notches of Constant Length for Frequencies of 500 Hz, 5 kHz, and 50 kHz

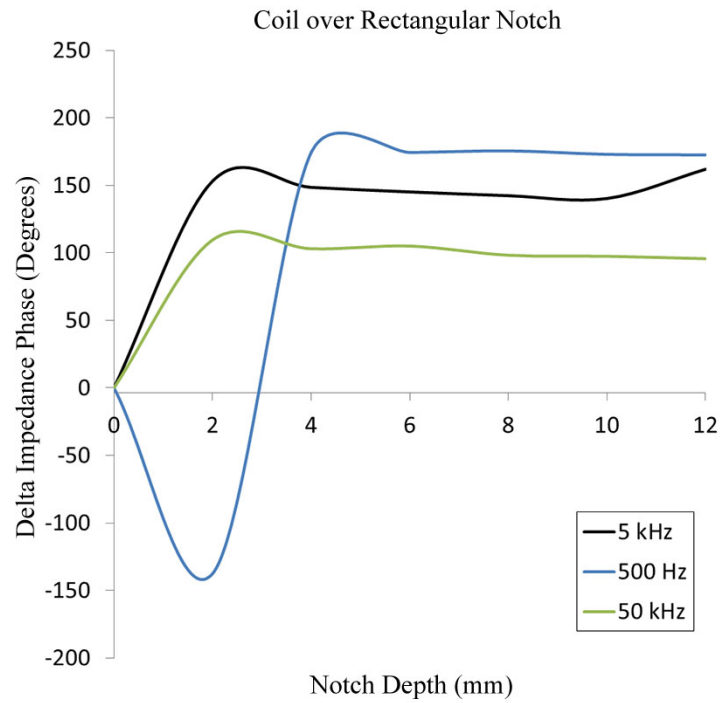


Figure 2.14. Change in Impedance Phase Angle versus Notch Depth for Rectangular Notches of Constant Length for Frequencies of 500 Hz, 5 kHz, and 50 kHz

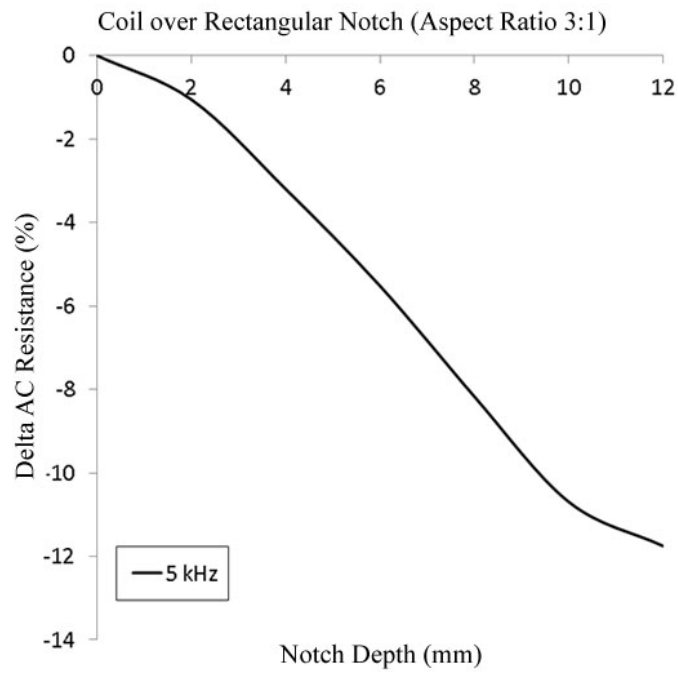


Figure 2.15. Change in Resistance versus Notch Depth for Rectangular Notches Aspect Ratio 3 for 5 kHz

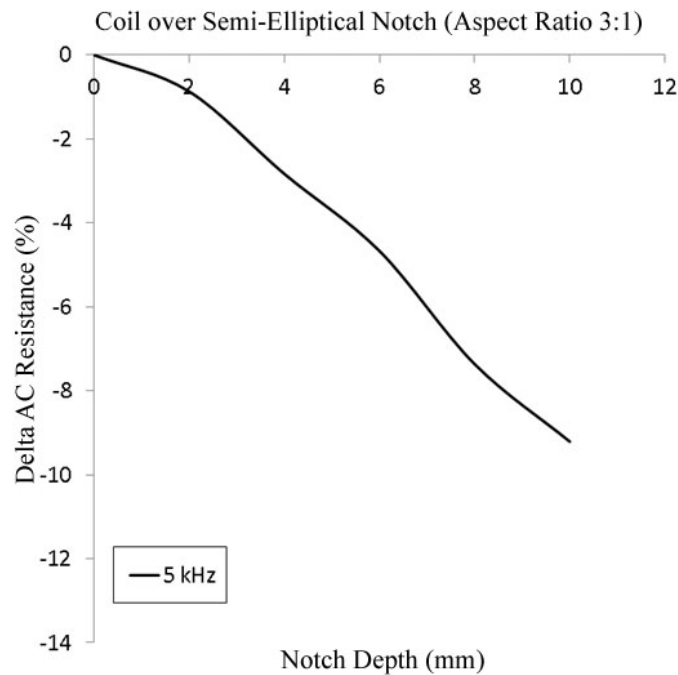


Figure 2.16. Change in Resistance versus Notch Depth for Semi-Elliptical Notches of Aspect Ratio 3 for 5 kHz

2.3.2 Parametric Analysis of Probe Parameters

A parametric study was performed, initially with the intention of exhaustively searching for optimum probe parameters for the purpose of flaw depth sizing. The change in signals for 4.2-mm deep flaws (approximately 33% through-wall depth) versus 8.4-mm deep flaws (approximately 67% through-wall depth) is used as a figure-of-merit to judge a given pancake coil design for depth sizing. Thus, in the case of the results presented in this sub-subsection and in Appendix B, $Z_0 = Z_{4.2\text{mm}}$ and $Z_1 = Z_{8.4\text{mm}}$. A reduced set of simulations was eventually performed because of greater-than-anticipated computational resource requirements. A summary of the cases considered is included in Table 2.4. Essentially, probe geometry parameters were varied for a total of 24 cases. These cases were then repeated for frequencies of 5 Hz, 25 kHz, and 50 kHz. In addition, the cases were repeated for the conditions of an air-core probe and a ferrite-core probe and for the conditions of an air-filled notch and a conducting notch with conductivity of 5% of the surrounding base metal.

Table 2.4. Summary of Parameters Considered in Parametric Studies

	Minimum Value	Maximum Value	Step Size	Units	Instances
Probe Parameters					
Inner radius	2	8	2	mm	4
Width	3	7	2	mm	3
Height	3	5	2	mm	2
Core	air	ferrite	---	---	2
Frequency		5, 25, 50		kHz	3
Defect Parameters					
Depth	4.2	8.4	4.2	mm	2
Aspect ratio	3	3	---	none	1
Width	0.15	0.15	---	mm	1
Conductivity	0	7.0E+04	7.0E+04	S/m	2
Shape	rectangular	rectangular	N/A	none	1
Specimen Parameters					
Thickness	12.7	12.7	---	mm	1
Conductivity (SS304)	1.4E+06	1.4E+06	---	S/m	1

Some results of the parametric analysis are provided in Figures 2.17 through 2.22. Figures 2.17 and 2.18 include results for simulations of an air-core probe over an air-filled notch at frequencies of 5 kHz and 50 kHz, respectively. Figures 2.19 and 2.20 include results for simulations of a ferrite-core probe over an air-filled notch at 5 kHz and 50 kHz, respectively. Finally, Figures 2.21 and 2.22 include results for an air-core probe over a conductive notch at 5 kHz and 50 kHz, respectively. From these simulations, it is clear that assuming a conductivity of 5% base metal results in a significant reduction of probe signals. Based on the results of this study, four cases that exhibit the best or nearly the best sensitivity for one or more of the scenarios (i.e., ferrite-core, air-core, air-filled notch, and conductive notch) include cases 3, 5, 9, and 11. The geometry parameters for these four pancake probe designs are summarized in Table 2.5. In all of these cases, the probe height is 3 mm, which is the lower of two probe height values considered in this study. The complete results from this parametric study are provided in Appendix B including the results for the 25-kHz case, and plots of the changes in the normalized resistance, the normalized reactance, and sum of the changes in the normalized resistance and normalized reactance in addition to changes in the normalized impedance.

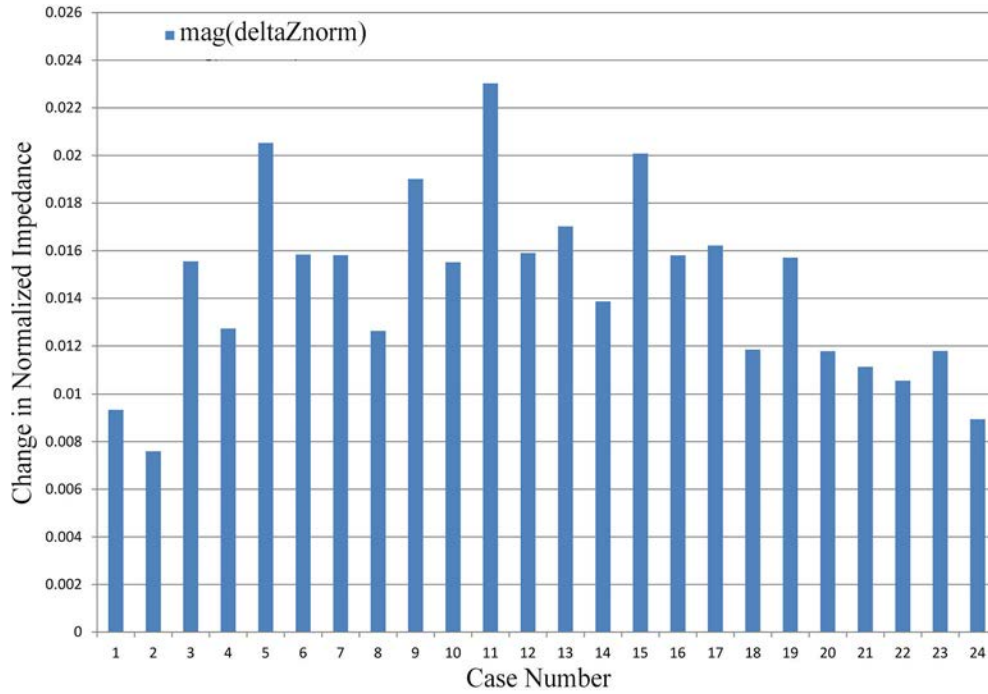


Figure 2.17. Results of Parametric Analysis for 24 Variations of Probe Geometry Parameters for an Air-Core Probe over an Air-Filled Notch at 5 kHz

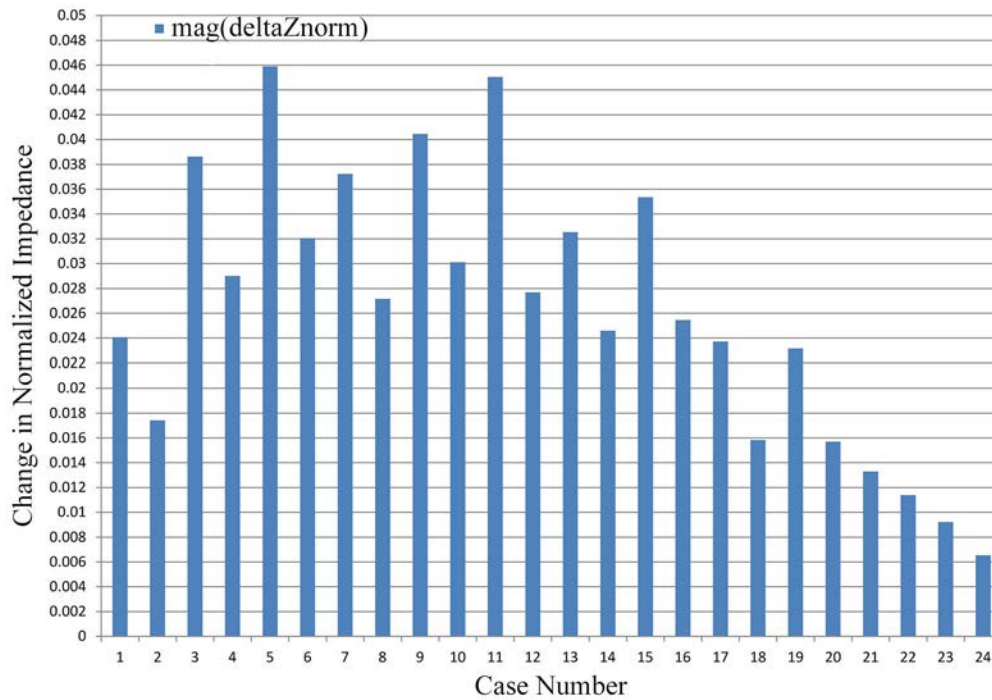


Figure 2.18. Results of Parametric Analysis for 24 Variations of Probe Geometry Parameters for an Air-Core Probe over an Air-Filled Notch at 50 kHz

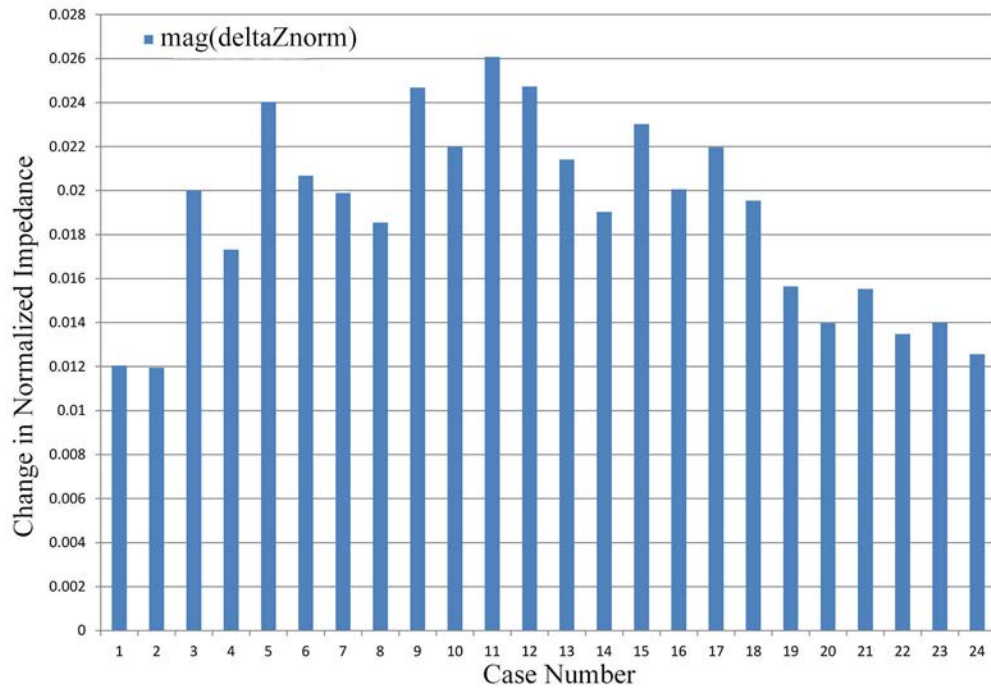


Figure 2.19. Results of Parametric Analysis for 24 Variations of Probe Geometry Parameters for a Ferrite-Core Probe over an Air-Filled Notch at 5 kHz

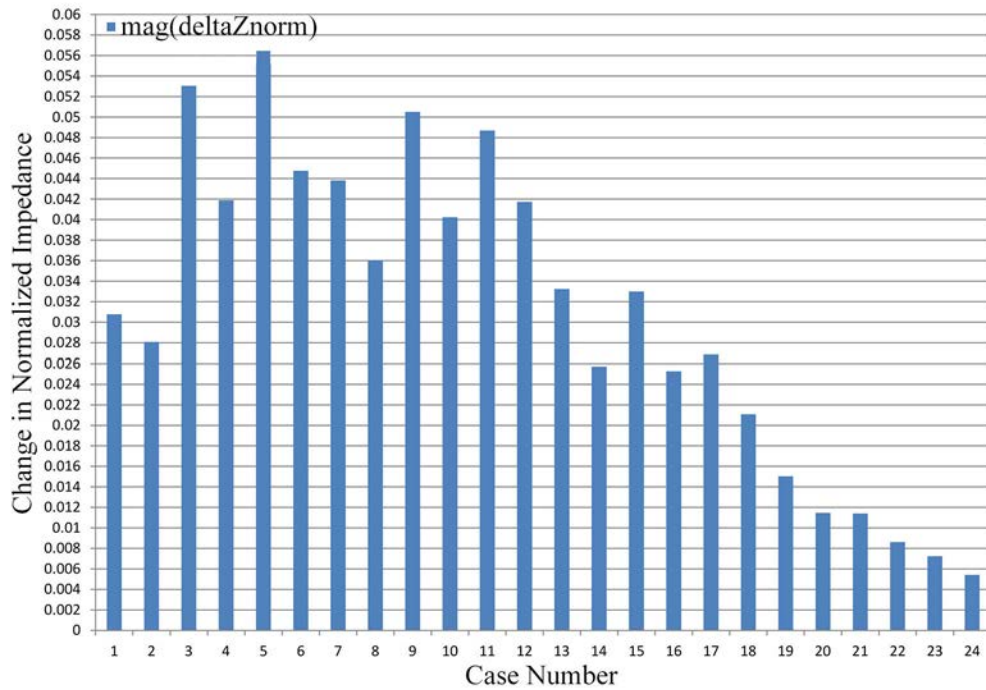


Figure 2.20. Results of Parametric Analysis for 24 Variations of Probe Geometry Parameters for a Ferrite-Core Probe over an Air-Filled Notch at 50 kHz

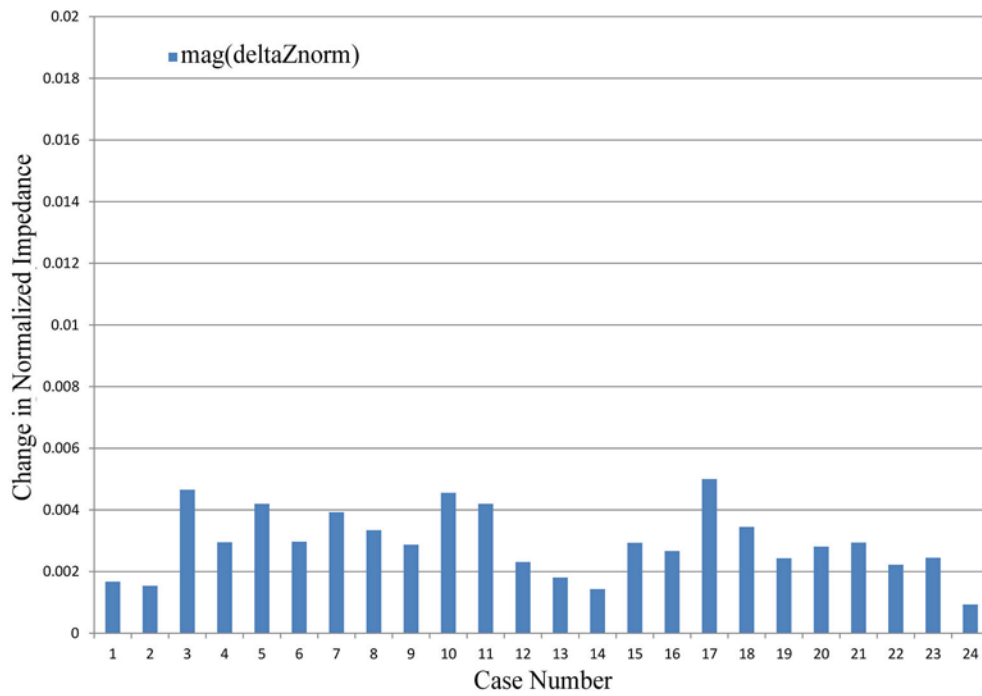


Figure 2.21. Results of Parametric Analysis for 24 Variations of Probe Geometry Parameters for an Air-Core Probe over a Conductive Notch at 5 kHz

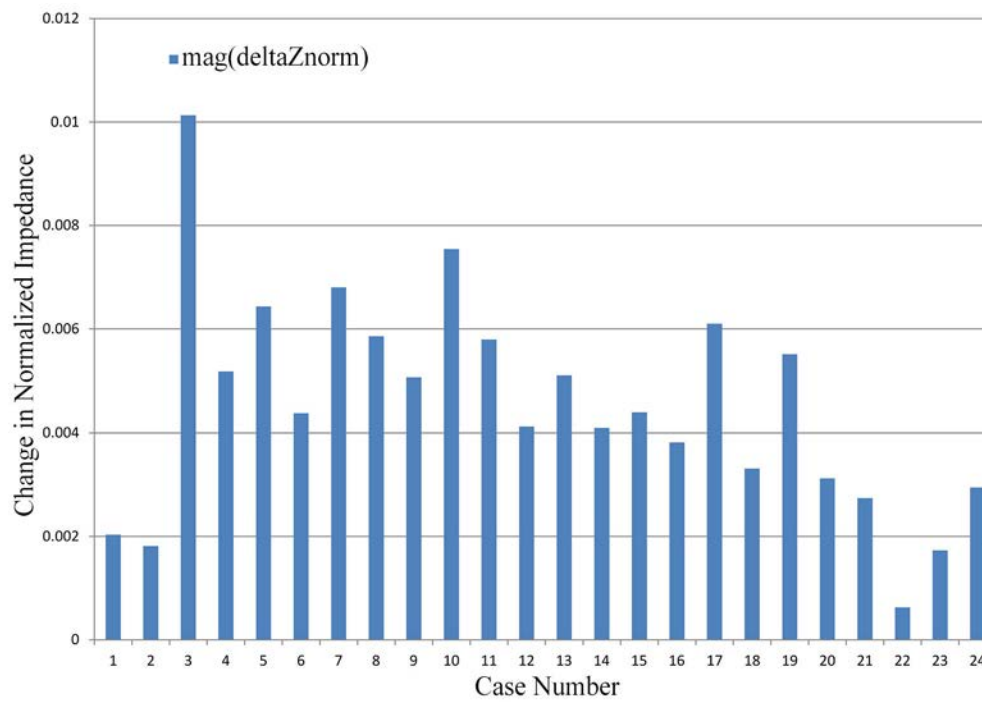


Figure 2.22. Results of Parametric Analysis for 24 Variations of Probe Geometry Parameters for an Air-Core Probe over a Conductive Notch at 50 kHz

Table 2.5. Summary of Cases Exhibiting the Best or Nearly the Best Sensitivity for One or More of the Scenarios Simulated

Case	Inner radius (mm)	Height (mm)	Width (mm)
3	2	3	5
5	2	3	7
9	4	3	5
11	4	3	7

2.3.3 Frequency Sweep Analysis

It has been noted that the SCC flaw model depicted in Figure 2.3 introduces additional unknown parameters that result in an inverse problem that is ill-posed. It has been suggested that additional pieces of information from multiple eddy current scans or by applying multiple NDE methods or techniques may provide the necessary additional information to find a unique solution (Yusa et al. 2007a). This section documents the results of initial efforts to identify features in swept frequency curves for eddy current responses that may be used to separate the effects of the multiple parameters (i.e., notch depth, notch conductivity, and notch width) and, thus, accurately determine the depth of SCC flaws in thick components. For results presented in this sub-subsection and in Appendix C, $Z_0 = Z_{\text{noflaw}}$ and $Z_1 = Z_{\text{flaw}}$.

Swept frequency signatures from 5 kHz to 100 kHz are plotted and displayed in several formats, including as curves in the impedance plane, as plots of change in normalized impedance versus frequency, change in normalized resistance versus frequency, change in normalized reactance versus frequency, and change in phase angle versus frequency. In addition, plots of the first derivatives of these curves versus frequency are obtained. This sub-subsection presents the plots of change in normalized impedance versus frequency, change in normalized resistance versus frequency, change in phase angle versus frequency and the impedance plane results. The rest of the plots are provided in Appendix C. For each case, the results of three different parametric studies are presented. Results are presented for the case of notches of constant depth (8.4 mm) for air-filled notches and 5% conductivity notches assuming air core and ferrite core probes. Results are also presented to display the trend in probe responses versus notch depths assuming 0% conductivity notches and 5% conductivity notches.

Figures 2.23 through 2.25 display results of frequency sweeps as curves in the impedance plane. In this case, the curves are traced out from 5 kHz to 100 kHz in the clockwise direction. In these cases, the vertical axes in these plots actually represent the normalized reactance, X_1/X_0 , and the horizontal axes actually represent the change in resistance, $(R_1 - R_0)/R_0$. It is clear from Figures 2.23 and 2.24 that an “elbow” exists in the curves for 0% conductivity notches on the left-hand side that correlates with a minimum in the change in normalized resistance near 10 kHz and that this elbow does not exist for the 8.4-mm deep 5% conductivity notches. However, Figure 2.25 indicates that this feature is also evident in shallow notches (4.2 mm and 2 mm for 5% conductivity).

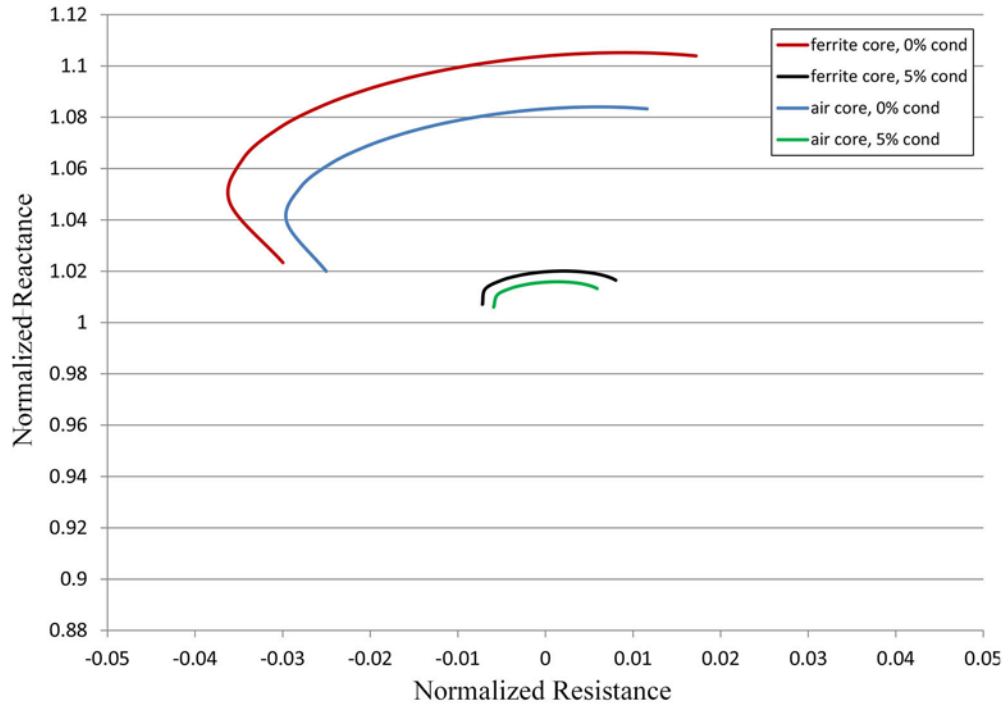


Figure 2.23. Impedance Plane Representation of Signal Responses from 8.4-mm deep Notches. Frequency increases from 5 kHz to 100 kHz in the clockwise direction.

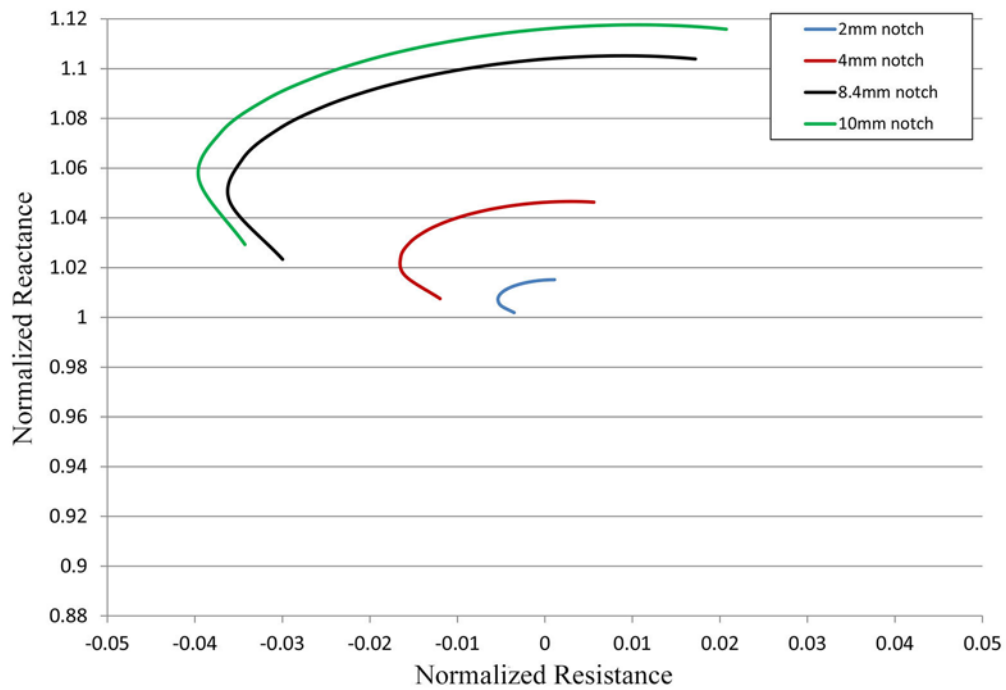


Figure 2.24. Impedance Plane Representation of Signal Responses from 0% Conductivity Notches. Frequency increases from 5 kHz to 100 kHz in the clockwise direction.

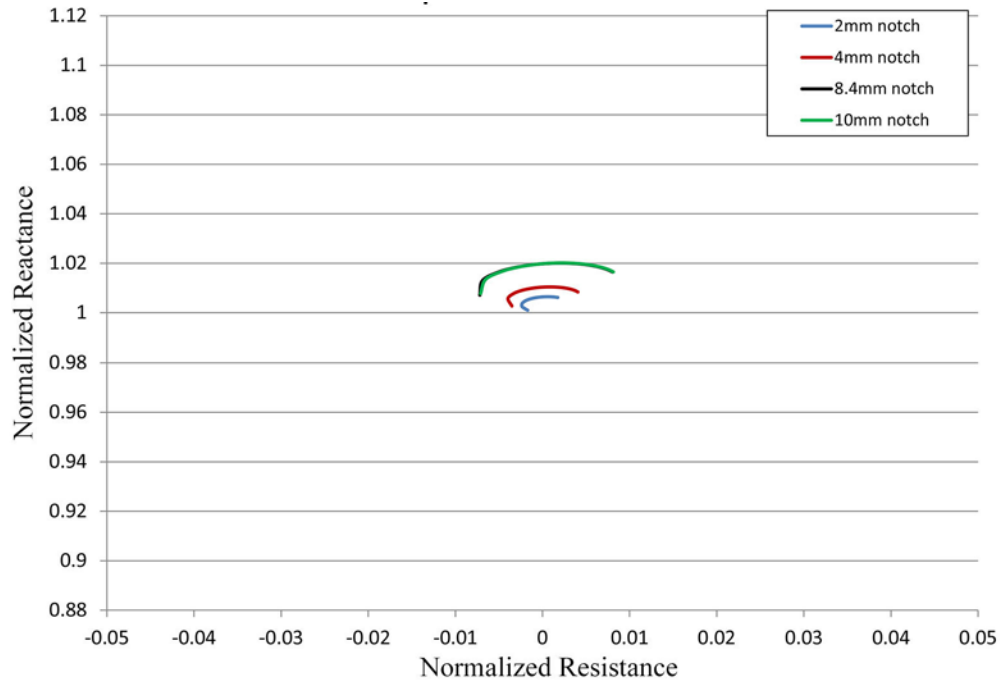


Figure 2.25. Impedance Plane Representation of Signal Responses from 5% Conductivity Notches. Frequency increases from 5 kHz to 100 kHz in the clockwise direction.

Plots of the change in normalized impedance versus frequency are displayed in Figures 2.26 to 2.28. The curves indicate a monotonic trend with respect to notch depth with the exception of the case of 5% conductivity notches, in which the 8.4-mm and 10-mm deep notches produce nearly identical signals. An additional feature of these curves that may be useful for characterizing defects is a peak in the curves with respect to frequency. In this case, the peak is more distinct in curves for the 5% conductivity notches than the curves for the 0% conductivity notches. Table 2.6 provides a summary of where the maxima in the normalized impedance are located on the frequency axis for 0% conductivity and 5% conductivity notches with depths of 2 mm, 4 mm, 8.4 mm, and 10 mm. Based on this data, it is apparent that the conductivity of the flaw has the most significant influence on the location of the peak.

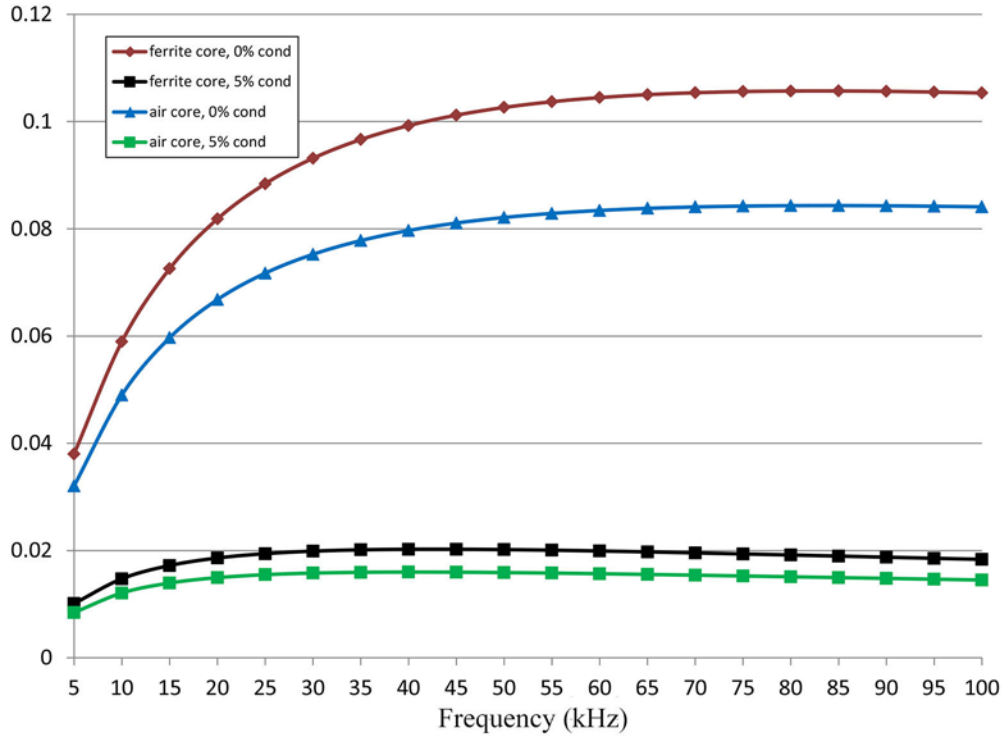


Figure 2.26. Change in Normalized Impedance vs. Frequency for 8.4-mm Deep Notches

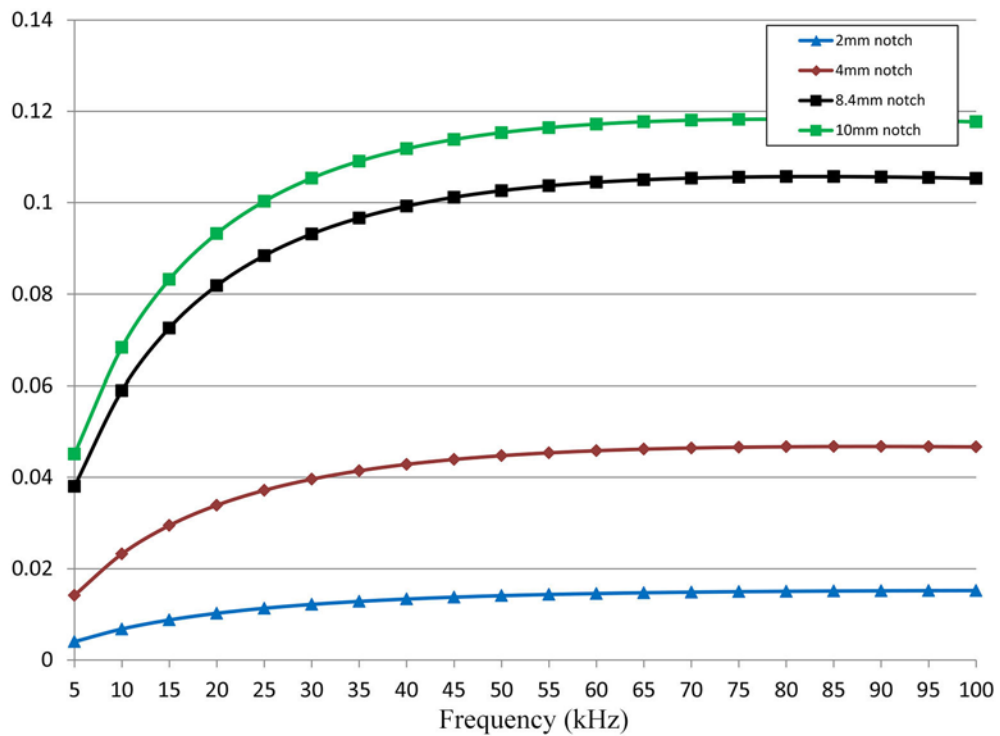


Figure 2.27. Change in Normalized Impedance vs. Frequency for 0% Conductivity Notches

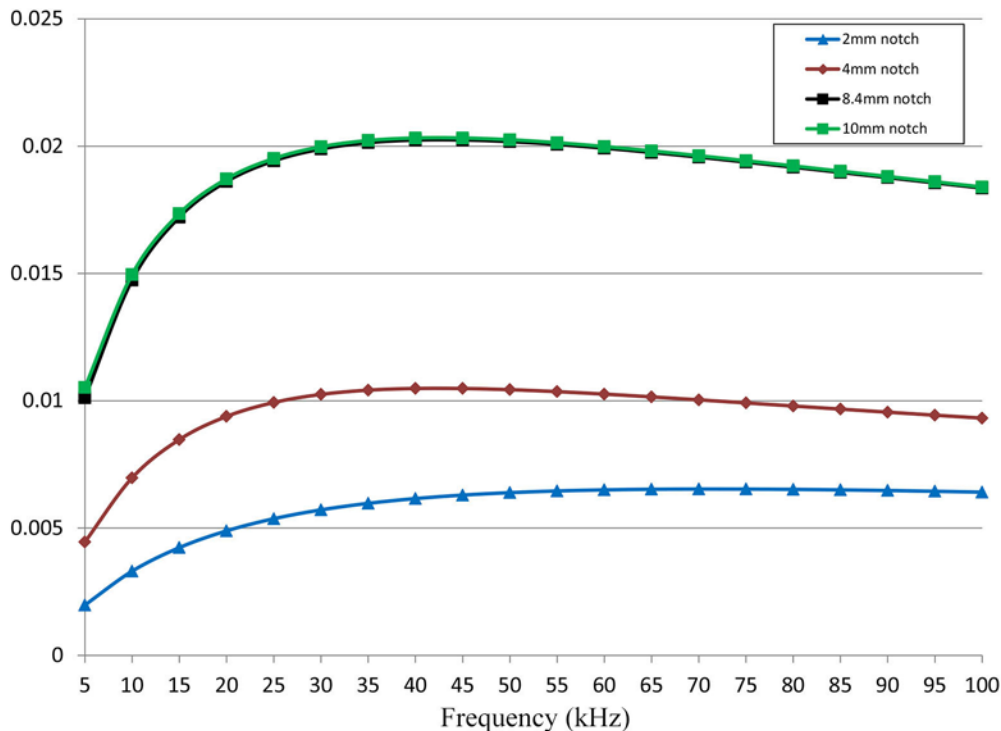


Figure 2.28. Change in Normalized Impedance vs. Frequency for 5% Conductivity Notches

Table 2.6. Summary of Locations of Change in Normalized Impedance Maxima

Notch Depth	0% Conductivity	5% Conductivity
2 mm	>100 kHz	75 kHz
4 mm	90–95 kHz	45 kHz
8.4 mm	85–90 kHz	45 kHz
10 mm	80–85 kHz	45 kHz

Change in normalized resistance versus frequency is included in Figures 2.29 through 2.31. Several interesting features may be observed in these plots including the location of the zero crossings, and the intersection of the curves for ferrite and air-core probes. In addition, the curves for 0% conductivity notches show a distinct minimum near 10 kHz that is also evident in the impedance plane plots in Figures 2.23 and 2.25. Table 2.7 summarizes where the zero crossings for the normalized resistance are located with respect to the frequency axis for 0% conductivity and 5% conductivity notches with depths of 2 mm, 4 mm, 8.4 mm, and 10 mm. In this case, the location of the zero crossing (i.e., 90° phase angle for change in impedance) is dependent on both the depth and conductivity of the notch.

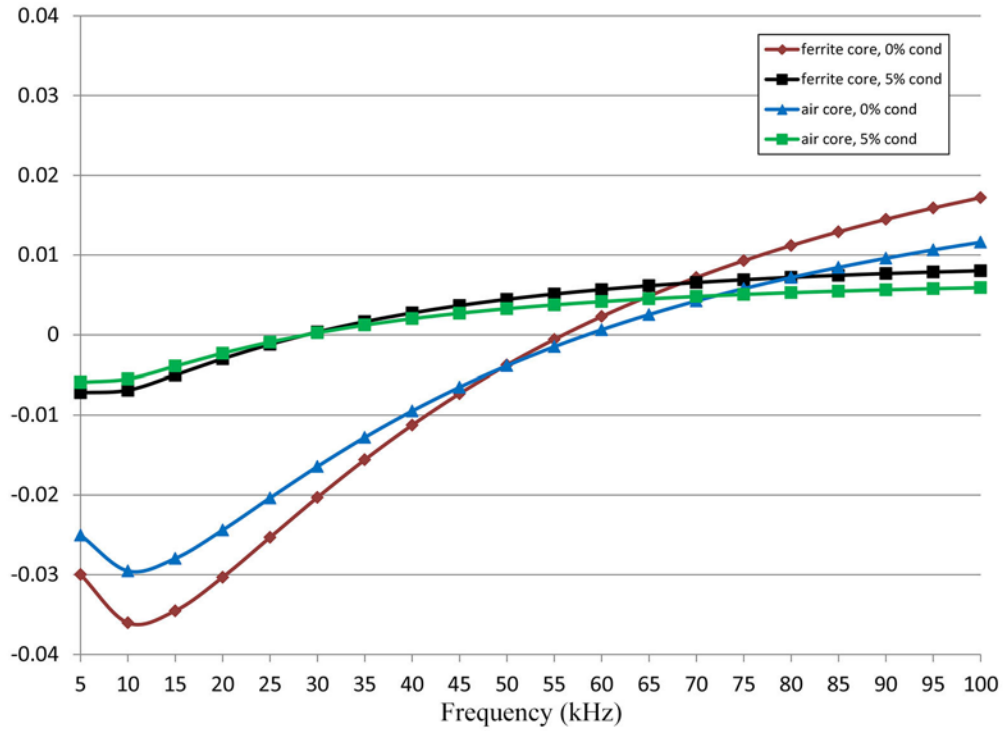


Figure 2.29. Change in Normalized Resistance vs. Frequency for 8.4-mm Deep Notches

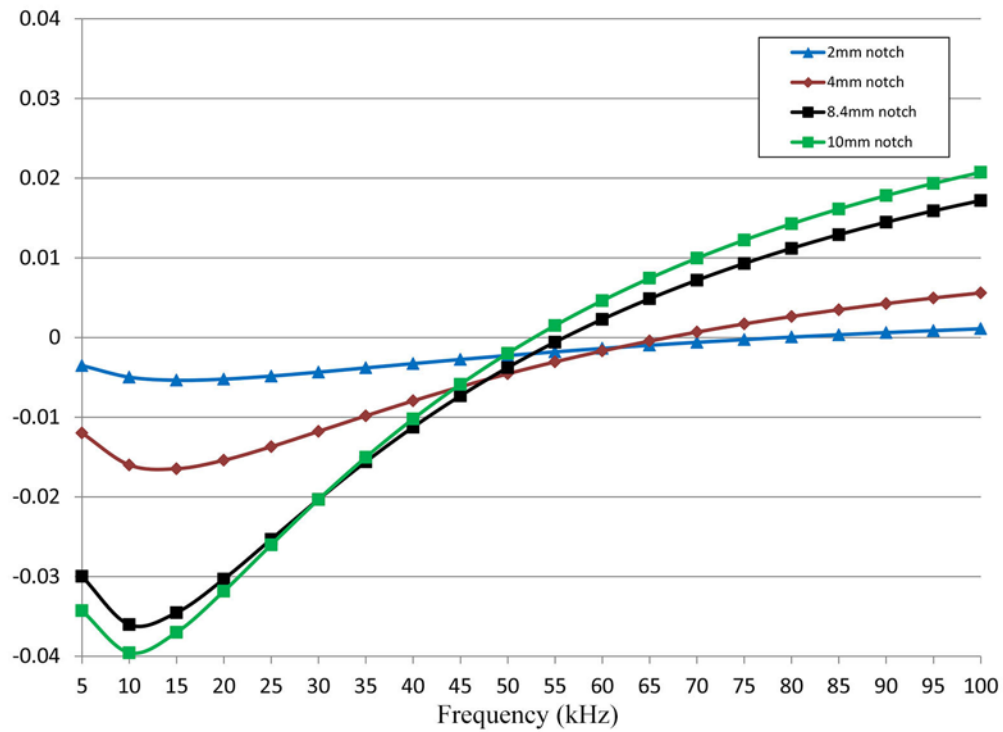


Figure 2.30. Change in Normalized Resistance vs. Frequency for 0% Conductivity Notches

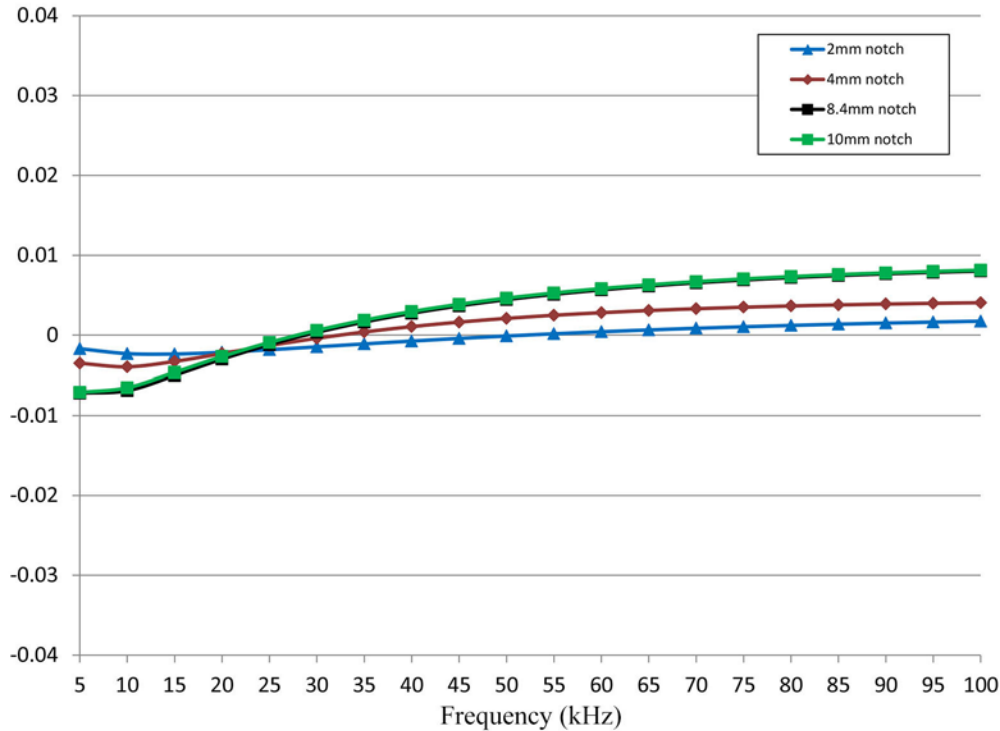


Figure 2.31. Change in Normalized Resistance vs. Frequency for 5% Conductivity Notches

Table 2.7. Summary of Zero Crossing Locations for Change in Normalized Resistance vs. Frequency

Notch Depth	0% Conductivity	5% Conductivity
2 mm	75–80 kHz	50–55 kHz
4 mm	65–70 kHz	30–35 kHz
8.4 mm	55–60 kHz	25–30 kHz
10 mm	50–55 kHz	25–30 kHz

Finally, the plots for change in impedance phase angle versus frequency are provided in Figures 2.32 through 2.34. A monotonic trend can be observed with respect to the value of the change in impedance phase angle with respect to notch depth for the 0% conductivity notches. However, for 5% conductivity notches, the 4-mm, 8.4-mm, and 10-mm deep notches appear to be much more difficult to distinguish based on phase, particularly at higher frequencies. A metric can be created from this data, which is the ratio of the change in impedance phase angle at 5 kHz to the change in impedance phase angle at 100 kHz [i.e., $\Delta Z(5\text{kHz})/\Delta Z(100\text{kHz})$]. Table 2.8 summarizes this ratio for 0% conductivity and 5% conductivity notches with depths of 2 mm, 4 mm, 8.4 mm, and 10 mm, indicating that this metric may provide a reliable method for characterizing the equivalent conductivity of flaws.

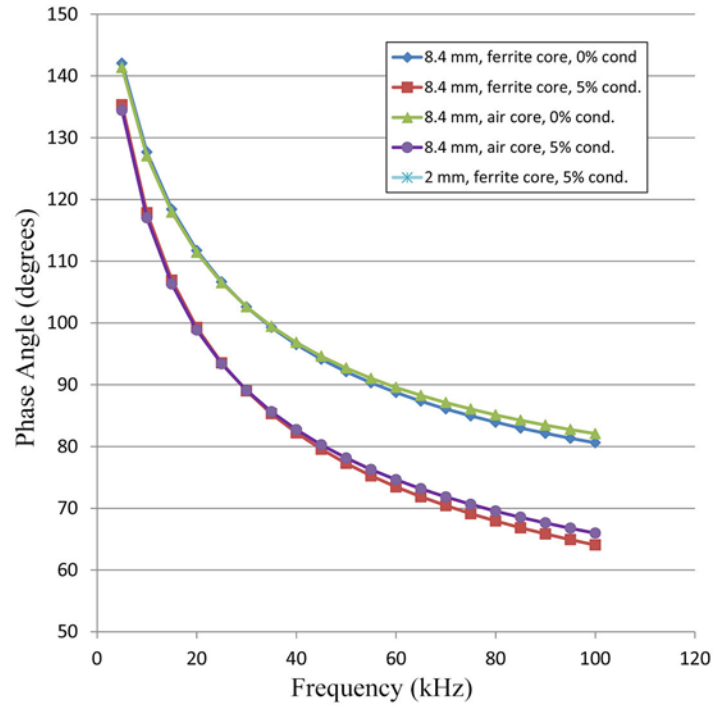


Figure 2.32. Change in Impedance Phase Angle vs. Frequency for 8.4-mm Deep Notches

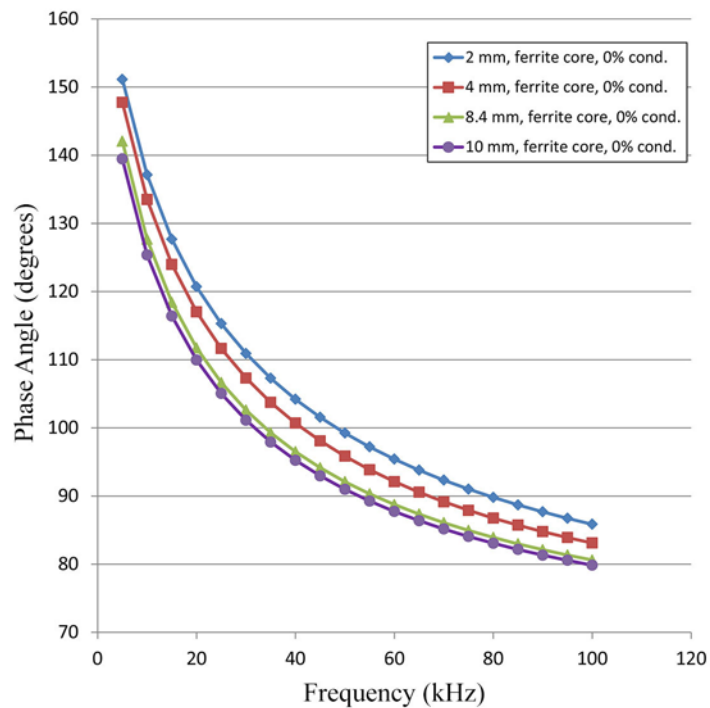


Figure 2.33. Change in Impedance Phase Angle vs. Frequency for 0% Conductivity Notches

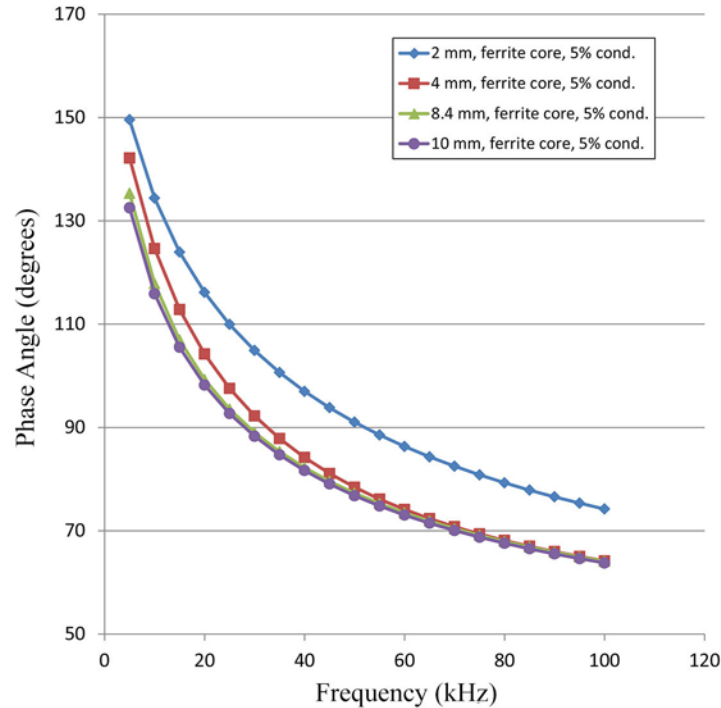


Figure 2.34. Change in Impedance Phase Angle vs. Frequency for 5% Conductivity Notches

Table 2.8. Ratio of Change in Impedance Phase Angle at 5 kHz to Change in Impedance Phase Angle at 100 kHz

Notch Depth	0% Conductivity	5% Conductivity
2 mm	1.76	2.02
4 mm	1.78	2.22
8.4 mm	1.76	2.11
10 mm	1.75	2.08

2.4 Summary of Accomplishments, Conclusions, and Future Efforts

FEM studies have been performed with the goal of identifying eddy current signal features that could be useful for characterizing SCC flaws and to delineate the effects of notch depth, equivalent conductivity, and equivalent width based on models of SCC flaws proposed by Yusa and Miya (2009). In FY13, these studies focused on “short” notches (with aspect ratio of 3) and on the effects of notch depth and equivalent conductivity on eddy current signals. Several features were identified as candidate metrics for characterizing SCC flaws. Significant observations include:

- The location of the peak in normalized impedance curves with respect to frequency may be useful for characterizing the equivalent conductivity of a flaw. The frequency at which the peak exists appears to decrease with increasing conductivity.
- The location of zero crossings for change in normalized resistance (i.e., $\angle \Delta Z = 90^\circ$) versus frequency may be useful for characterizing the equivalent conductivity. The zero crossings are located at lower frequencies for 5% conductivity notches versus 0% conductivity notches.

- The existence and location of minimum values in the change in normalized resistance curves versus frequency may be useful for characterizing the equivalent conductivity of a flaw. For deeper flaws (i.e., 8.4 mm) this minima exists for 0% conductivity flaws but not 5% conductivity flaws.
- The phase angle of the change in normalized impedance indicates a monotonic behavior with respect to notch depth over the frequency range considered for 0% conductivity notches. However, for 5% conductivity notches, this trend is not as apparent.
- A metric defined as the ratio of the phase angle of the change in normalized impedance at 5 kHz to the phase angle of the change in normalized impedance at 100 kHz appears to provide a good discriminator of flaw conductivity regardless of notch depth.

Based on the results of the FEM analysis performed thus far, more studies should be performed to explore the following:

- Observe trends in eddy current probe signal features as a function of equivalent notch width and identify effective metrics for discriminating effects of equivalent width from the effects of equivalent conductivity and notch depth.
- The intersection of the frequency sweep curves for both air-core and ferrite-core probes may provide useful information for the purposes of flaw characterization and should be explored more fully.
- The frequency sweep studies conducted thus far focused on “short” notches (i.e., aspect ratio of 3). Similar studies should be performed for “long” notches (i.e., notch length is much longer than notch depth or coil diameter).
- Extend the bounds of the frequency analysis to frequencies greater than 100 kHz and frequencies below 5 kHz.
- Explore the effectiveness of metrics for discriminating equivalent conductivity on a finer scale (i.e., discriminate between 0% and 1% equivalent conductivity or 1% and 2% equivalent conductivity, etc., or even finer scales).
- Explore other potential eddy current probe configurations such as the differential “plus-point” probe.

In addition to the FEM analysis, it is prudent to construct coils to verify the findings of the FEM analysis conducted thus far on physical specimens and to verify that the model of SCC flaws proposed by Yusa and Miya (2009) forming the basis of these studies is sufficiently accurate. This may be feasible using specimens collected thus far, or may require fabrication of additional specimens. In addition, eddy current scans performed on specimen B-117 containing a thermal fatigue crack with measured COD of 0.018 mm indicate that eddy current methods and techniques can detect flaws that are too narrow to detect reliably using standard visual testing equipment. Assessments of visual testing have documented that the reliability of visual testing begins to drop for cracks with CODs below 0.1 mm, and that below 0.02 mm, cracks are very difficult to detect even under favorable conditions (Cumblidge et al. 2004; Cumblidge et al. 2007). A review of several failure analysis reports found that SCC flaws observed in nuclear and non-nuclear industries have median CODs in the range of 0.016 mm to 0.03 mm (Wåle 2006). Studies that assess the reliability of eddy current to detect SCC flaws with CODs in this range or lower could provide a supporting technical basis for use of eddy current to inspect DCSS canister surfaces. In this case, modeling efforts should be leveraged to the extent possible to minimize the burden of performing tests on physical specimens.

3.0 CHARACTERIZING HYDROGEN EFFECTS IN CLADDING

A brief discussion of the cladding hydriding phenomenon and hydrogen effects in cladding is provided in the report by Hanson et al. (2013). In this report, it is explained that during reactor operations, Zircaloy fuel cladding is in contact with the high-temperature and high-pressure reactor coolant (water and/or steam) and corrodes according to the reaction,



Some amount of the hydrogen is absorbed in the cladding. The amount of absorbed hydrogen can depend on several factors, the most significant of which are described as the chemical composition of the cladding material and the presence and integrity of oxide layers on the cladding surface. For instance, alloys of zirconium (known as Zircaloy) are extensively used for nuclear fuel cladding. It is known that the presence of Ni in Zircaloy-2 (Zr-2) promotes the absorption of hydrogen, while Zircaloy-4 (Zr-4) was developed in which the Ni is replaced with additional Fe to maintain corrosion resistance.

At concentrations above the solubility limit, absorbed hydrogen precipitates to form “platelets.” In Zircaloy, the hydrides tend to form on the basal plane of the hexagonal unit cell (Hanson et al. 2013). Depending on manufacturing processes and environmental exposures (i.e., temperature, stress, and radiation), these hydrides can orient themselves in the circumferential or radial directions (see Figure 3.1). Billone et al. (2008, 2013) have shown that at high temperatures and stress, the normally circumferential hydrides found in high burn-up (i.e., >45 gigawatt-days per metric ton uranium) cladding can reorient in the radial direction. Fracture resistance is reduced in the direction of the hydrides; thus, through-wall crack propagation is significantly more likely for radially oriented hydrides than circumferentially oriented hydrides. Thus, cladding with radially oriented hydrides is expected to have less resistance to failure under dry storage and transportation conditions.

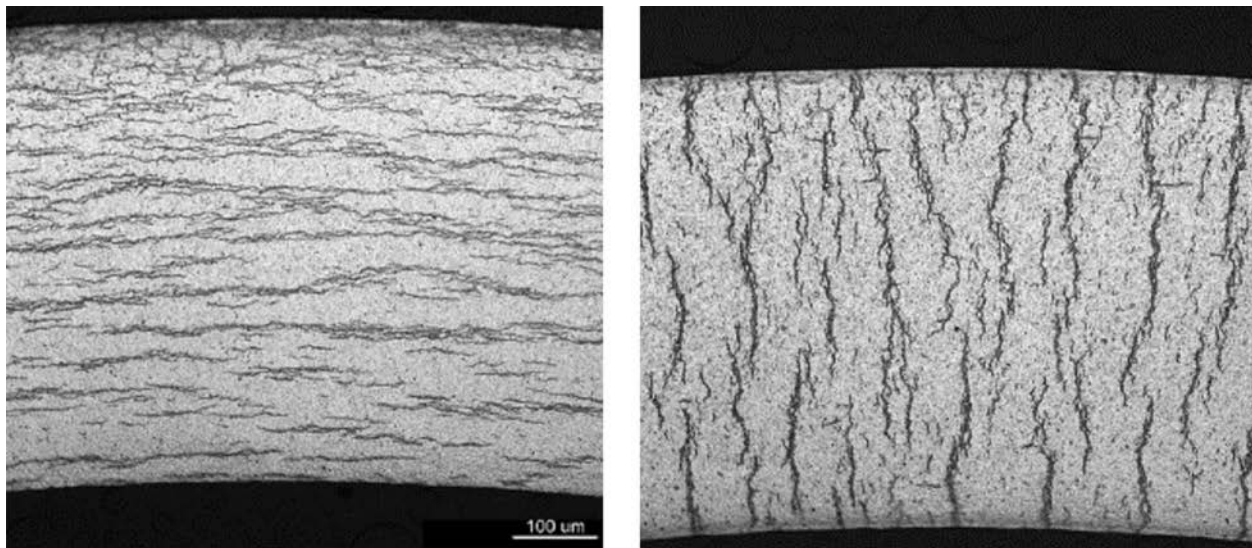


Figure 3.1. Depiction of (a) Circumferential Hydride Orientation and (b) Radial Hydride Orientation (Hanson et al. 2013)

The mechanical integrity of fuel cladding can be significantly influenced by the distribution of hydrides in addition to hydride platelet orientation. A comparison of cladding of high burn-up fuel with unirradiated specimens charged to approximately equal total hydrogen content showed significant differences in hydride distribution. Whereas the hydride distribution in unirradiated specimens was uniform, the hydride distribution in cladding of high burn-up fuel was uneven, with a much higher concentration near the cladding outer diameter (a hydride rim) (Billone et al. 2013). This region of dense hydride concentration is more brittle in nature than other areas of the cladding facilitating crack initiation.

3.1 Ultrasonic Characterization of Hydride Phenomena

A review of open literature highlights previous efforts to characterize the hydride phenomenon in nuclear fuel cladding ultrasonically. De et al. (1998) performed ultrasonic velocity measurements on plate shaped (3-mm thick) Zr-2 samples uniformly charged with hydrogen to levels in the range of 50 to 1150 mg/kg. Velocity measurements exhibited a decreasing trend up to hydrogen concentrations of 100 mg/kg, while the ratio of longitudinal to shear velocity wave speed was a parameter found to correlate with hydrogen concentration up to the range of approximately 100 to 200 mg/kg. Also, attenuation measurements were found to be useful for estimating higher levels of hydrogen content. Ultrasonic velocity measurements were performed by Gómez et al. (2006) on Zr-4 samples charged with hydrogen up to concentrations of 550 ppm. In this case, rectangular samples were prepared with thickness of 6.3 mm. Above 200 ppm, velocity measurements at 10 MHz are described as providing a useful assessment parameter and showed an approximately linear increase with hydrogen concentration (from 4635 to 4665 m/s), but the error in the measurement has prohibited accurate measurements below 200 ppm. A logarithmic fit was observed between attenuation measurements and hydrogen concentration at 10 MHz; whereas, at 30 MHz, no clear trend could be observed.

In Yang and Huang (2004), leaky lamb wave measurements in Zr-4 tubes having 0.64-mm wall thickness were measured using low-frequency transducers operated in Z-scan mode. A curve is shown demonstrating a linear relationship between the velocity of the A0 mode at 1.6 MHz and hydrogen concentration having a slope of 5.022 m/s per 100 ppm of hydrogen. The technique was able to determine hydrogen concentration in tubes with resolution better than 300 ppm. Liu and Yang (2006) report on the use of the laser ultrasound technique (LUT) for the characterization of hydride rims (HR) in Zircaloy cladding tubes establishing relationships between dispersion curves and HR thicknesses. Hydride rims with thicknesses from 20 microns to 80 microns are characterized with an accuracy of 10%. In Liu and Yang (2008), the application of LUT is presented for characterizing the elastic modulus and wall thickness of Zircaloy tubes with different levels of hydrogen charging. The capability to measure wall thickness to within 1.78% is reported. Efforts to characterize hydrogen-charged Zircaloy tube samples are also described by Yang and Lai (2006) and the method is described as capable of measuring hydrogen concentration over the range of 0 to 1200 ppm with a resolution of 200 ppm based on ultrasonic velocity measurements. In Yeh and Yang (2010), a LUT method is used to excite circumferentially guided waves in hydrogen charged Zr-4 tubes in an attempt to measure the ratio of radially to circumferentially oriented hydrides. The technique is described as being able to discriminate between different values of this ratio and the observation is made that the bulk elastic modulus increases as the value of this ratio increases.

3.2 Elastic Property Measurements

Several measurement techniques are attempted in this effort to correlate hydrogen effects with elastic properties in cladding. These techniques include measurements of the Rayleigh wave velocity, enhanced backscatter measurements, and resonant ultrasound spectroscopy measurements. This subsection provides background information related to each of these measurement techniques.

3.2.1 Rayleigh Wave Velocity

The elastic properties of a material can be determined from measurements of the velocities of ultrasonic signals propagating through the material. For homogenous, isotropic media, the elastic moduli can be related to the longitudinal and shear velocities, V_L and V_T ,

$$E = \rho V_T^2 \frac{3V_L^2 - 4V_T^2}{V_L^2 - V_T^2}, \quad (3.2)$$

$$G = \rho V_T^2, \quad (3.3)$$

$$\nu = \frac{1 - 2\left(\frac{V_T}{V_L}\right)^2}{2\left(1 - \left(\frac{V_T}{V_L}\right)^2\right)}, \quad (3.4)$$

where E , G , and ν represent the Young's modulus, Shear modulus, and Poisson's ratio, respectively and ρ is the mass density of the material. In terms of the stiffness coefficients, c_{11} and c_{44} , respectively, the E and ν may be expressed as,

$$E = c_{44} \left[\frac{3c_{11} - 4c_{44}}{c_{11} - c_{44}} \right], \text{ and} \quad (3.5)$$

$$\nu = \frac{c_{11} - 2c_{44}}{2(c_{11} - c_{44})}. \quad (3.6)$$

Measurements of the longitudinal and shear wave velocity components, V_L and V_T , can be made based on time-of-flight techniques relying on a back wall reflection. Measurements of V_L are relatively straight forward in that they can be performed by the immersion technique in pulse-echo mode. Separate measurements of the specimen thickness are required to determine the path length traveled by the ultrasonic beam within the test specimen. Measurements of V_T are more complicated because they either require the application of a viscous fluid for coupling of the transducer or an immersion technique with angle of incidence above the first critical angle for longitudinal wave propagation in the cladding material, but less than the critical angle for shear wave propagation. The former case has some drawbacks because the coupling may be inconsistent and it does not facilitate easy scanning. In the latter case, the length of the beam path within the test specimen may be difficult to accurately determine. An alternative to performing measurements of V_T includes performing measurements of the Rayleigh

38

velocity, V_R . V_T can be determined from measurements of V_L and V_R by solving the following polynomial equation for V_T ,

$$V_T^8 - (V_L^2 + V_R^2)V_T^6 + \frac{3}{2}V_L^2V_R^2V_T^4 - \frac{1}{2}V_L^2V_R^4V_T^2 + \frac{1}{16}V_L^2V_R^6 = 0 \quad (3.7)$$

which is valid for,

$$0 \leq V_T \leq \frac{V_L}{\sqrt{2}}. \quad (3.8)$$

Rayleigh waves are a type of acoustic wave that propagates on the surface of solids. Rayleigh waves are typically described as having ellipsoidal polarization with displacements in directions both longitudinal and transverse to the material's surface. When the surface of a solid is adjacent to a liquid, Rayleigh waves traveling along this interface are referred to as leaky Rayleigh waves because they radiate from the surface of the solid into the liquid and experience attenuation, as a result.

Rayleigh waves (including leaky) can be generated using angle beam ultrasonic transducers. Ultrasonic waves are refracted when they pass through the boundary of two media with different elastic properties at an angle. This refraction process is governed by Snell's Law,

$$\frac{\sin \theta_1}{\sin \theta_2} = \frac{V_1}{V_2}, \quad (3.9)$$

where θ_1 is the angle of incidence on the boundary at the interface between media 1 and 2, θ_2 is the angle of the refracted wave in media 2, while V_1 and V_2 are the sound velocities in media 1 and 2, respectively. The angle of incidence at which Rayleigh waves are generated can be determined by setting $\theta_2 = 90^\circ$ in Eq. (3.9) and solving for θ_1 ,

$$\theta_1 = \sin^{-1}\left(\frac{V_1}{V_2}\right) = \theta_{CR}. \quad (3.10)$$

This angle is the Rayleigh critical angle, θ_{CR} . Similarly, the Rayleigh velocity, V_R can be determined by solving Eq. (3.10) for V_2 ,

$$V_2 = \frac{V_1}{\sin \theta_{CR}} = V_R. \quad (3.11)$$

In essence, when a finite size beam is incident at a liquid-solid interface at θ_{CR} , two components of reflection are produced: (1) a component of specular reflection and (2) a non-specular component that represents the leaking Rayleigh waves. This phenomenon is illustrated in Figure 3.2, showing the two components separated by a "null" zone because of the lateral displacement of the leaky Rayleigh wave component.

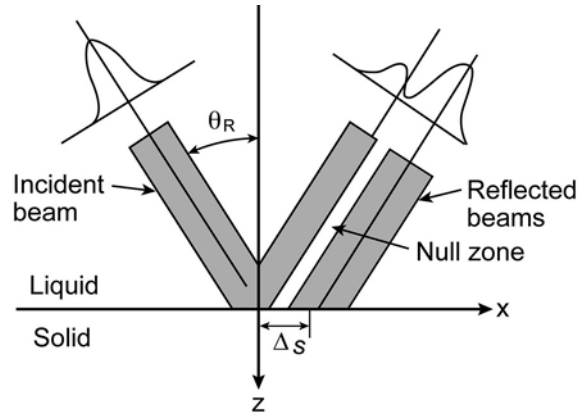


Figure 3.2. Illustration of Reflected Beam Components when the Incident Beam is at the Rayleigh Critical Angle. The two components include (1) a component of specular reflection and (2) a non-specular component associated with leaking Rayleigh waves (from Yu and Boseck 1995).

The presence of the two components of reflection is exploited in scanning acoustic microscopy and the $V(z)$ type measurement often employed for materials characterization (Yu and Boseck 1995). In the case of $V(z)$ type measurements, a large aperture transducer is typically employed oriented at a normal angle of incidence, and operates in pulse-echo mode. The large size of the aperture ensures that the transducer receives the component of specular reflection and the leaky Rayleigh wave component (see Figure 3.3). Because of lateral propagation of the leaky Rayleigh wave component, a path length difference exists between the two components. As the transducer is translated closer to or farther from the interface (in the z -direction), this interference results in an oscillatory pattern of the received signal amplitude as depicted by Figure 3.4. The period of this oscillation can be used to determine θ_{CR} and V_R through the following equations,

$$\Delta z = \frac{\lambda_1}{2(1 - \cos \theta_{CR})}, \text{ and} \quad (3.12)$$

$$V_R = \frac{V_1}{\left[1 - \left(1 - V_1 / (2f \Delta z)\right)^2\right]^{1/2}}. \quad (3.13)$$

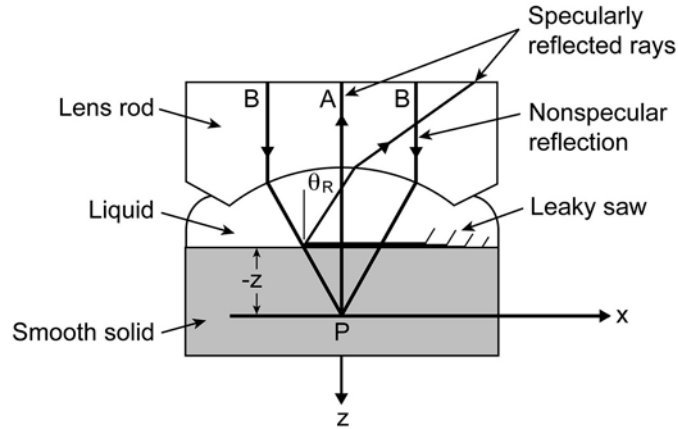


Figure 3.3. Depiction of Double Ray Reflection Model for Scanning Acoustic Microscopy $V(z)$ Scans (from Yu and Boseck 1995)

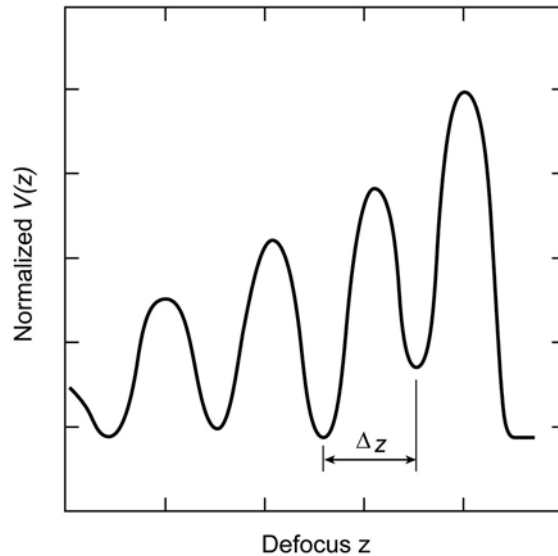


Figure 3.4. Depiction of a $V(z)$ Profile Obtained by Scanning Acoustic Microscopy Measurement (from Yu and Boseck 1995)

Alternatively, V_R can also be determined from $V(x)$ scans using a pitch-catch arrangement of transducers oriented at θ_{CR} (Neuenschwander et al. 2006). In this case, the path length of the propagating Rayleigh wave can be difficult to determine, complicating time-of-flight measurements. However, one can increment the position of the receiving transducer by Δx , parallel to the surface of the test piece. In doing so, a delay, Δt , is observed in the received signal from the additional path length, Δx , of the Rayleigh wave propagating on the test specimen surface. This arrangement is illustrated in Figure 3.5. In this case, V_R can be calculated from,

$$V_R = \frac{\Delta x}{\Delta t} \quad (3.14)$$

The existence of a specular reflection component and a non-specular reflected leaky Rayleigh wave component leads to an interesting profile for the amplitude of the receiving signal if the receiver is scanned over the direction x , parallel to the surface of the test specimen. An example of the amplitude profile received is provided in Figure 3.6. The first peak, Max 1, is associated with the component of specular reflection while the second peak, Max 2, is associated with the non-specular reflection component due to leaky Rayleigh waves. When performing $V(x)$ measurements of V_R , it is important to ensure the non-specular component is received, associated with Max 2 and the leaky Rayleigh waves.

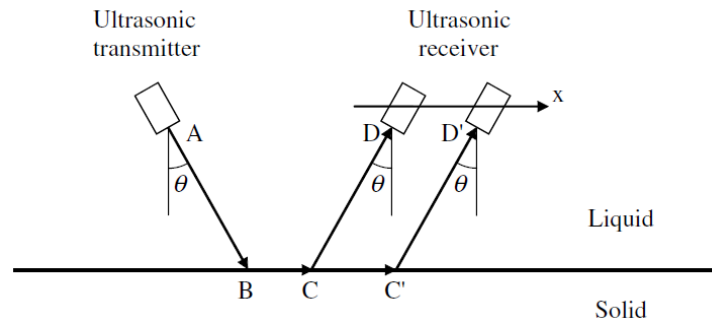


Figure 3.5. Illustration of $V(x)$ Method for Determination of V_R . Reprinted from Neuenschwander et al. (2006). Copyright (2006), with permission from Elsevier.

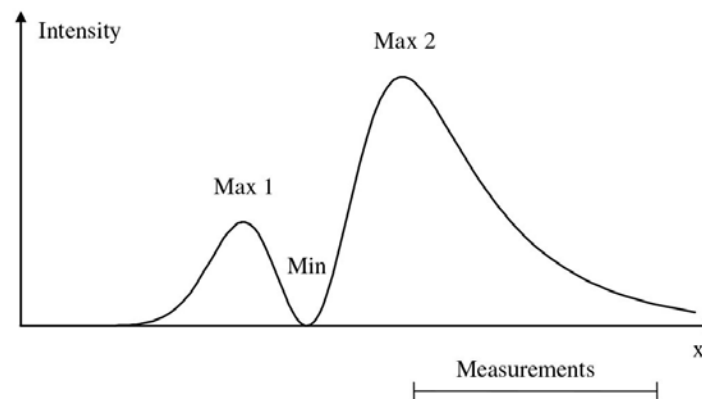


Figure 3.6. Illustration of the Double-Peak Amplitude Profile as the Receiving Transducer is Scanned Along x . The first peak, Max 1, is associated with the component of specular reflection while the second peak, Max 2, is associated with the non-specular reflection component from leaky Rayleigh waves. Reprinted from Neuenschwander et al. (2006). Copyright (2006), with permission from Elsevier.

3.2.2 Enhanced Backscatter Effect

It is noted that significant backscatter of acoustic radiation at the Rayleigh angle has been observed during investigations of the Schoch displacement effect associated with the propagation of leaky Rayleigh waves (Norris 1983). Subsequent investigations into the backscatter of ultrasonic waves from liquid-solid

interfaces confirmed these observations (de Billy and Adler 1982; de Billy and Quentin 1982; Nagy and Adler 1989, 1994). de Billy and Adler (1982) noted that the observed backscattering phenomenon may be used to measure the Rayleigh velocity at liquid-solid interfaces and that the spatial distribution of the reflected ultrasonic energy at the liquid-solid interface agrees with the theory of Bertoni and Tamir (1973); namely, that the reflected field consists of two components: (1) a component of coherent reflection and (2) a component of incoherent scattering from radiation of leaky Rayleigh waves, as depicted in Figure 3.2. Norris (1983) attempted to model the backscatter phenomena by considering finite beam effects on coherent scattering. The model predicted a proportional relationship between the backscatter amplitude and the Schoch displacement and an inversely proportional relationship between the backscatter amplitude and beam width. This was in apparent agreement with the experimental observations of de Billy and Adler (1982). However, the model of Norris (1983) predicted backscatter for all angles of incidence, not just the Rayleigh angle.

Nagy and Adler (1989) investigated the backward radiation effect at a liquid-solid interface at the Rayleigh angle and distinguished between the two components of backward radiation caused by back reflection as a finite beam effect and backscattering from inherent material inhomogeneity. They concluded that backscattering from inherent material inhomogeneity was the exclusive contributor to the observed backward radiation effect producing a peak at the Rayleigh angle. They describe the backscattering of energy at the Rayleigh angle from inherent material inhomogeneity as closely related to a similar phenomenon observed by de Billy and Quentin (1982) for randomly rough surfaces. In further investigation, Nagy and Adler (1989) also performed a series of experiments to test a hypothesis that the observed backscattering peak at the Rayleigh angle is caused by an increase in the strength of the evanescent field in the solid. Constructive interference between shear and longitudinal partial waves at the Rayleigh angle results in a resonance effect that reduces the impedance of the solid material. In essence, backward-propagating leaky Rayleigh waves are transmitted most efficiently into the liquid media at the Rayleigh angle because of a dip in the impedance caused by resonance. Further, they explain that the previously observed inverse relationship between beam width and backscatter peak amplitude was an artifact of measurements, and not a consequence of the underlying phenomenon. They explored variables impacting the amplitude and width of the backscatter peak observed at the Rayleigh angle. Based on the hypothesis and measurements, it was concluded that the width of the peak is determined by the density ratio between the solid and the liquid and that amplitude of the peak depends on the scattering inhomogeneity and does not depend on the average material properties. Modeling results from Nagy and Adler (1994) for steel and aluminum are shown in Figure 3.7.

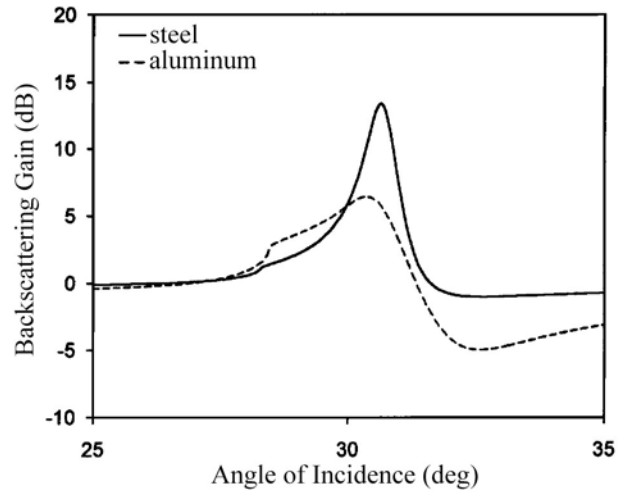


Figure 3.7. Depiction of Backscattering Peaks for Steel and Aluminum as Predicted by Nagy and Adler (1994). Reprinted with permission from Nagy and Adler (1994). Copyright 1994, Acoustical Society of America.

3.2.3 Resonant Ultrasound Spectroscopy

Resonant ultrasound spectroscopy (RUS) is an emerging alternative nondestructive evaluation (NDE) technique that relies on the resonance spectra of a part. RUS technology, which is also popularly known as resonant inspection (RI), is based on the assumption that every part has its unique vibration signature (resonance frequency). According to the vibration theory, the spectrum frequency is determined by the following formula:

$$F = \sqrt{\frac{K}{M}} \quad (3.15)$$

where F is the resonant frequency, K is the stiffness, and M is the mass. Or in a more general form (Auld 1973)

$$\omega^2 = \frac{\int \nabla_s \mathbf{v} : \mathbf{c} : \nabla_s \mathbf{v} dV}{\int \rho \mathbf{v} \cdot \mathbf{v} dV} \quad (3.16)$$

where c is the elastic stiffness tensor, ρ is the density, ω is the angular frequency, and v is the velocity vector. The above formula implies that any changes in c , ρ , or geometric dimensions can introduce variations to parts of or the whole resonance spectra, which forms the theoretical foundation of the RI technology.

As an emerging indirect NDE technique, vibration-based RI has been adopted by several automotive aluminum castings suppliers in quality control to separate the good and anomalous part populations (Nath et al. 2004). Their basic premise is that changes in local/distributed stiffness, mass, or energy dissipation

properties will lead to changes in the natural frequency spectrum of a vibrating system (Adams et al. 1978; Doebbling et al. 1998).

RUS is performed using broadband transducers and employing a frequency sweep or other excitation source over a range to observe peaks in the frequency spectrum where resonant vibrations occur. The characteristics of the frequency spectrum are related to the material properties (i.e., elastic properties) and geometry of the specimen. The elastic properties are determined by solving the governing equations to obtain the frequency spectrum theoretically and iteratively updating values for elastic constants until sufficient agreement is observed between calculated and measured spectra. For this reason, RUS measurements are performed on specimens with simple geometries such as parallelepipeds, cylinders, or spheres.

3.3 Status Update

This subsection presents results and progress associated with attempts to measure the elastic properties of cladding using ultrasonic enhanced backscatter measurements, RUS, and Rayleigh wave velocity measurements.

3.3.1 Backscatter Measurements

Figure 3.8 depicts how backscatter measurements were performed on tube specimens using an immersion transducer in pulse-echo mode. Scanning over the cross section of the tube ensures sampling a range of incident angles, including the Rayleigh critical angle, as the surface of the tube curves away from the transducer. The scanning was performed by positioning specimens underneath transducers in a SONIX Fusion scanning acoustic microscope (SAM) as shown in Figure 3.9. Initially, several scans were performed in an effort to determine the best frequency(ies) for performing backscatter measurements. This was evaluated through visual examination of scan outputs, such as those shown in Figure 3.10 for a stainless steel tube immersed in water and scans performed at 30 MHz and 50 MHz. In these scans, a bright vertical strip through the center of the scans represents normal incidence back-reflection from the top of the tube. In these images, symmetrical vertical lines on both sides of the central strip are evident, which correspond with the enhanced backscattering effect.

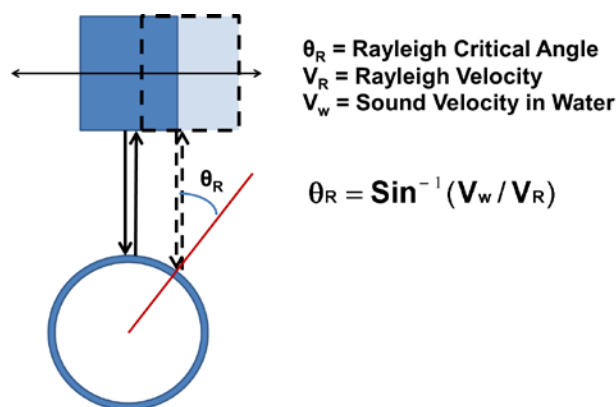


Figure 3.8. Depiction of Backscatter Measurements to Determine the Rayleigh Critical Angle for Tube Specimens

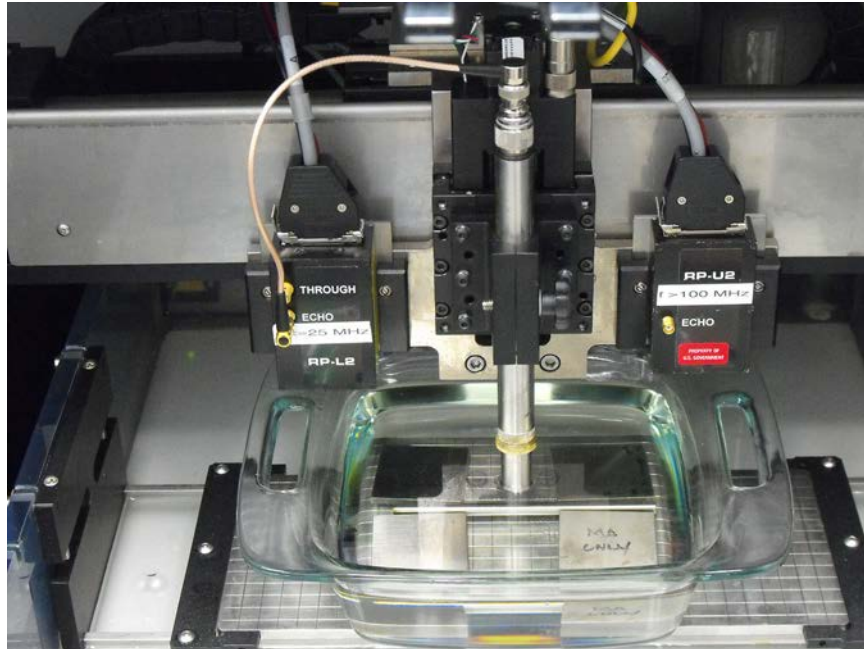


Figure 3.9. Photograph of Experimental Set-up Showing Placement of Specimen and Transducer in x-y Scanner of the SAM

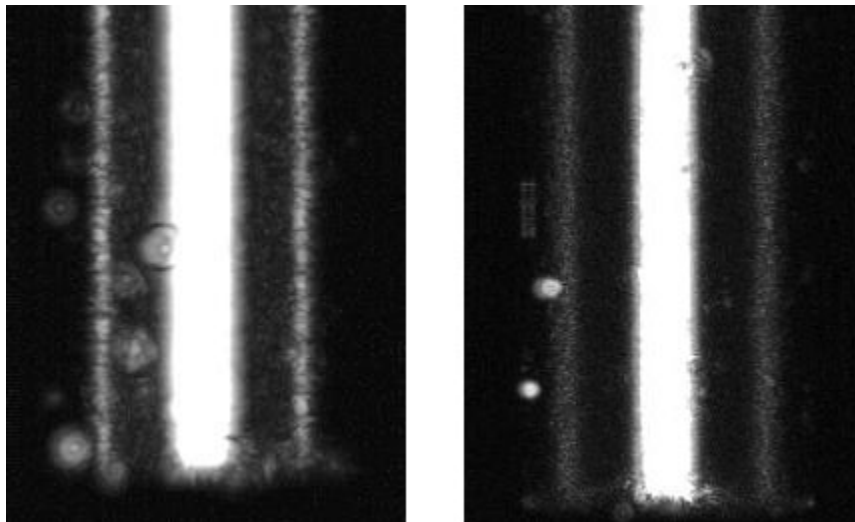


Figure 3.10. SAM Images Obtained for Stainless Steel Specimen at 30 MHz (left) and 50 MHz (right)

Similar measurements were attempted on un-treated tube specimens of Zr-4 material (specimens 1a and 2a – see Appendix D). In this case, enhanced backscatter lines were not visible in the scan images. In water, the Rayleigh angle for stainless steel is approximately 31° , while for Zr-4, it is near 42° . In an effort to obtain better results on the Zr-4 specimens, the specimens were immersed in ethanol to decrease

46

the Rayleigh angle. The result of the scan performed in ethanol at 30 MHz is provided in Figure 3.11. In this case, signals for scans in ethanol were gated to reduce the prominence of the back-reflection signal at normal incidence in the images. The Rayleigh angle can be determined from the separation of the backscatter peaks observed in the scan images. In this case, the peak separation is 3.8 mm. For comparison, the scan performed in water is shown again in Figure 3.12 along with cursors to show the measurement of peak separation. In the case of water, the backscatter peaks are separated by 5.0 mm. A summary of the Rayleigh angles and Rayleigh velocities determined from these measurements is provided in Table 3.1. Consistency is exhibited for estimation of the Rayleigh velocity in stainless steel from measurements performed in both water and ethanol, and thus, support the hypothesis that the symmetrical vertical lines in the scan images for stainless steel are enhanced backscatter peaks at the Rayleigh critical angle. However, an attempt to detect enhanced backscattering from Zr-4 specimens immersed in ethanol was unsuccessful. Results from scanning Zr-4 specimens 1a and 2a are provided in Figure 3.13 and Figure 3.14, respectively. No enhanced backscatter peak is observed in these images and relatively strong axially oriented indications are observed. These strong indications appear to be caused by scratches on the surface of the Zr-4 specimens.

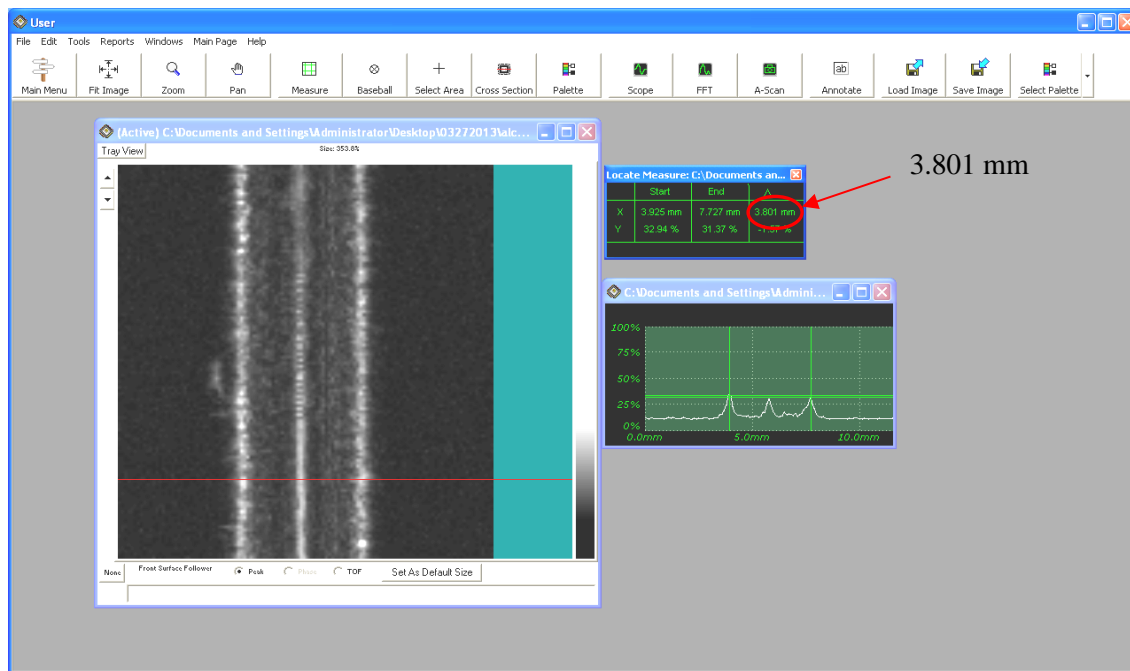


Figure 3.11. SAM Image for Stainless Steel Specimen in Ethanol. The distance between backscatter peaks is measured across a section of the sample indicating a peak separation of 3.8 mm. Gating was adjusted for scans in ethanol to reduce the prominence of the reflection signal at normal incidence in the images.

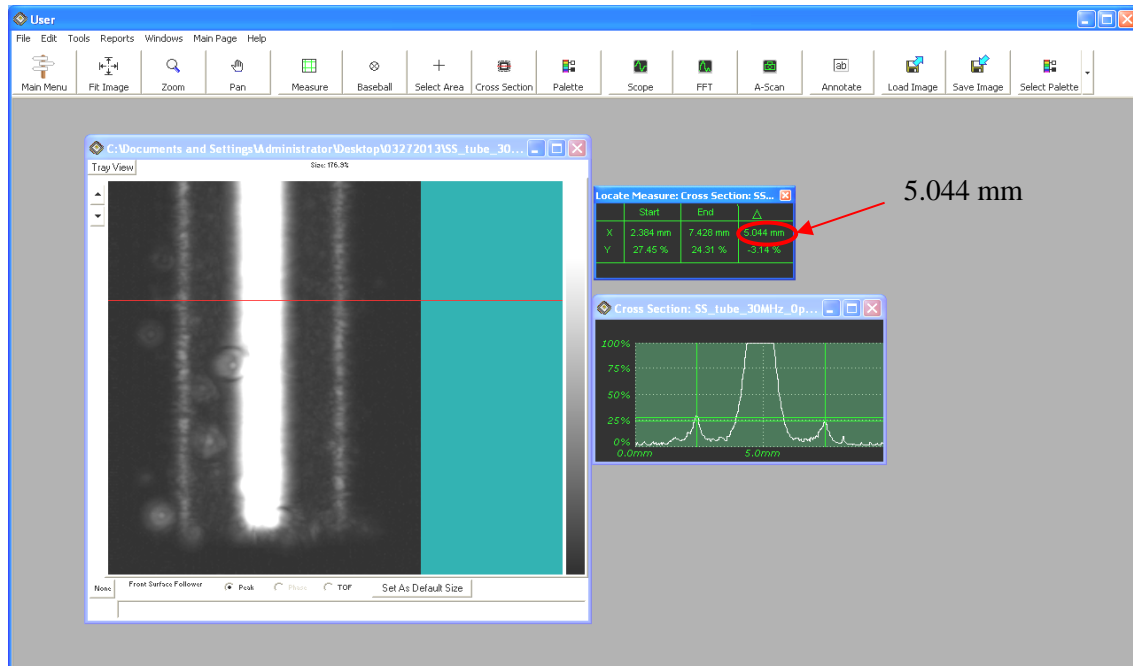


Figure 3.12. SAM Image for Stainless Steel Specimen in Water. The distance between backscatter peaks is measured across a section of the sample indicating a peak separation of 5.0 mm.

Table 3.1. Summary of Backscatter Peak Analysis for Stainless Steel Specimen in Water and Ethanol

	Water (velocity – 1480–1500 m/s) [assumed]	Ethanol (velocity – 1130–1140 m/s) [measured]
Peak Separation	5 mm	3.80 mm
Θ_{CR}	31.68°	23.52°
V_R	2818–2856 m/s	2832–2857 m/s

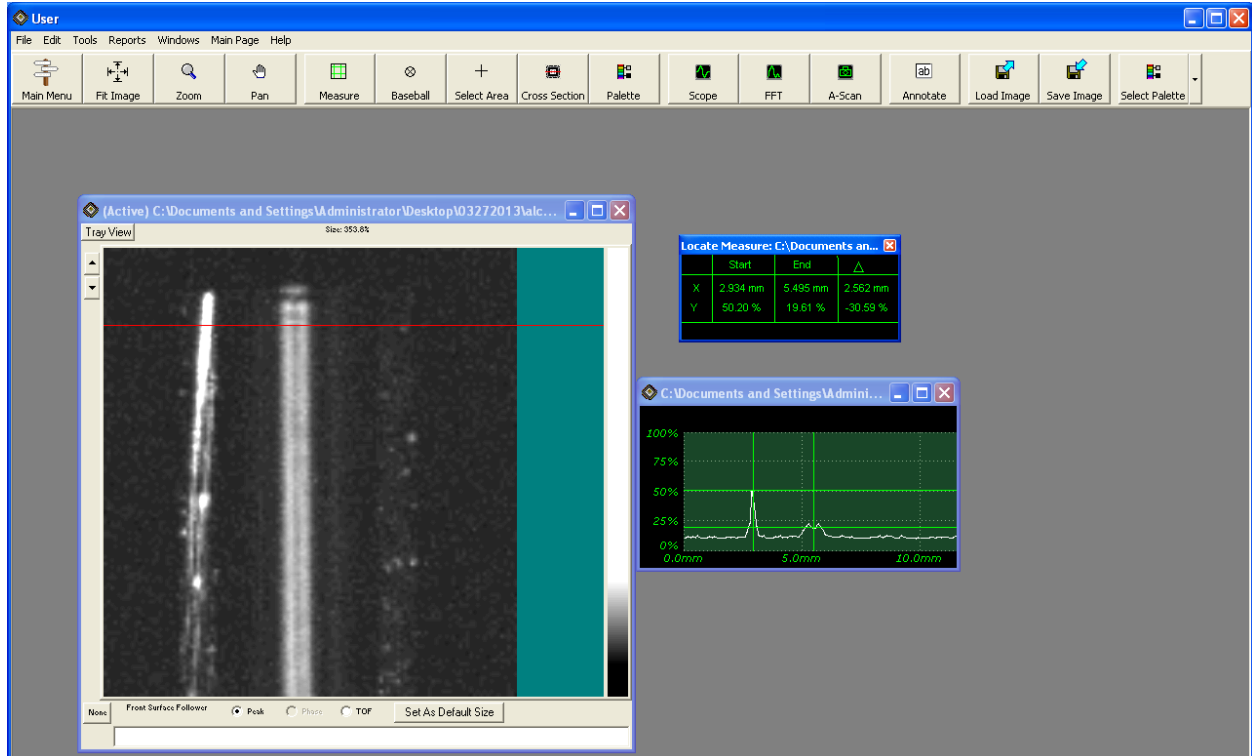


Figure 3.13. SAM Image Obtained for Zirc-4 Specimen 1a Immersed in Ethanol

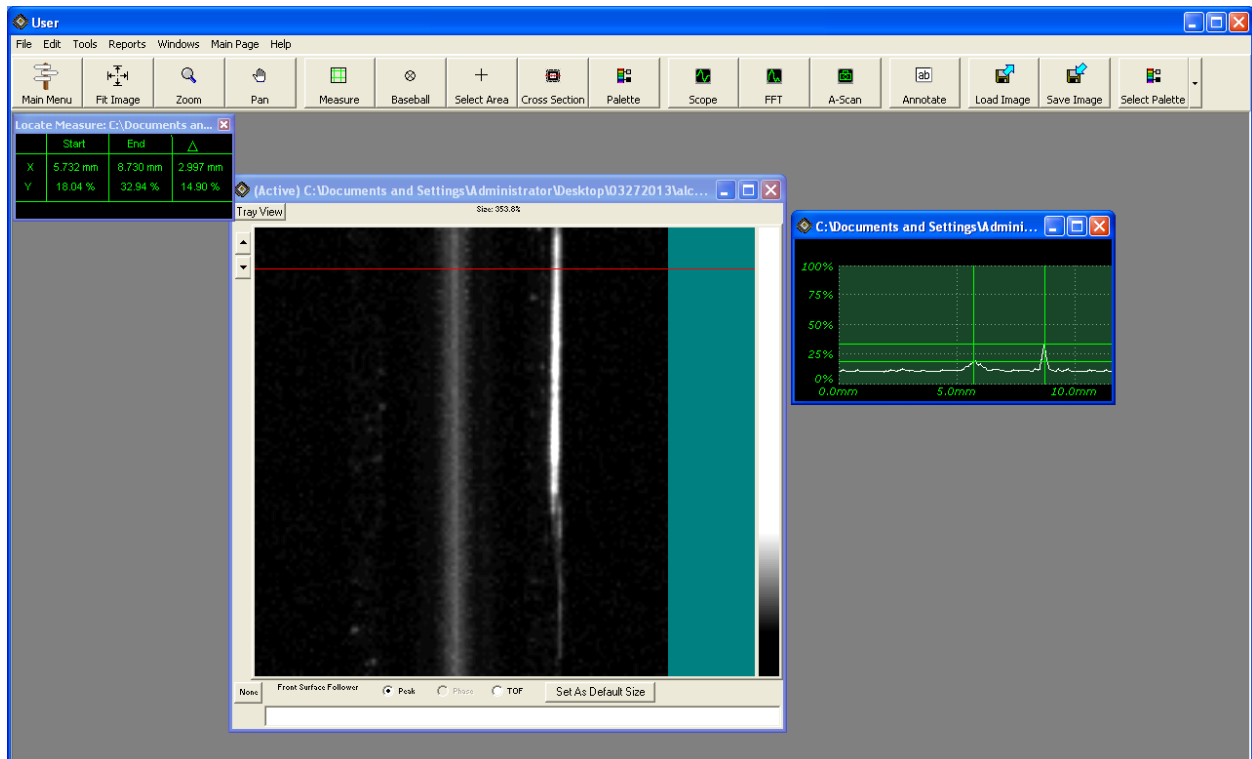


Figure 3.14. SAM Image Obtained for Zirc-4 Specimen 2a Immersed in Ethanol

In addition to water and ethanol, two other liquids were considered for backscatter measurements of Zr-4, and a summary of acoustic properties for all liquids obtained from Cheeke (2002) is provided in Table 3.2. In this case, Bromobenzene was identified as another candidate liquid for performing the scans because the Rayleigh angle for Zr-4 is close to the Rayleigh angle for stainless steel in water. In addition, the impedance of Bromobenzene is relatively close to that for water and Bromobenzene has a very low attenuation. However, only relatively weak backscatter peaks were observed in an initial scan of a stainless steel specimen in Bromobenzene (see Figure 3.16) and scanning of Zr-4 in Bromobenzene was not attempted.

Table 3.2. Summary of Relevant Properties for Potential Immersion Fluids (source: Cheeke 2002)

	Velocity (m/s)	Impedance (MRayl)	Impedance Ratio	Attenuation (dB/cm)	θ_{CR} (stainless steel)^(d)	θ_{CR} (zirc-4)^(e)
Water	1480 ^(a)	1.483 ^(a)	1.000	22 ^(b)	31.9°	42.3°
Ethanol	1207 ^(b)	0.95 ^(b)	1.561	48.5 ^(b)	25.5°	33.3°
Methanol	1103 ^(b)	0.872 ^(b)	1.701	30.2 ^(b)	23.2°	30.1°
Bromobenzene	1167 ^(c)	1.776 ^(c)	0.835	1.63 ^(c)	24.6°	32.0°

(a) at 20°C
 (b) at 25°C
 (c) at 22°C
 (d) assume $V_R = 2800$ m/s
 (e) assume $V_R = 2200$ m/s

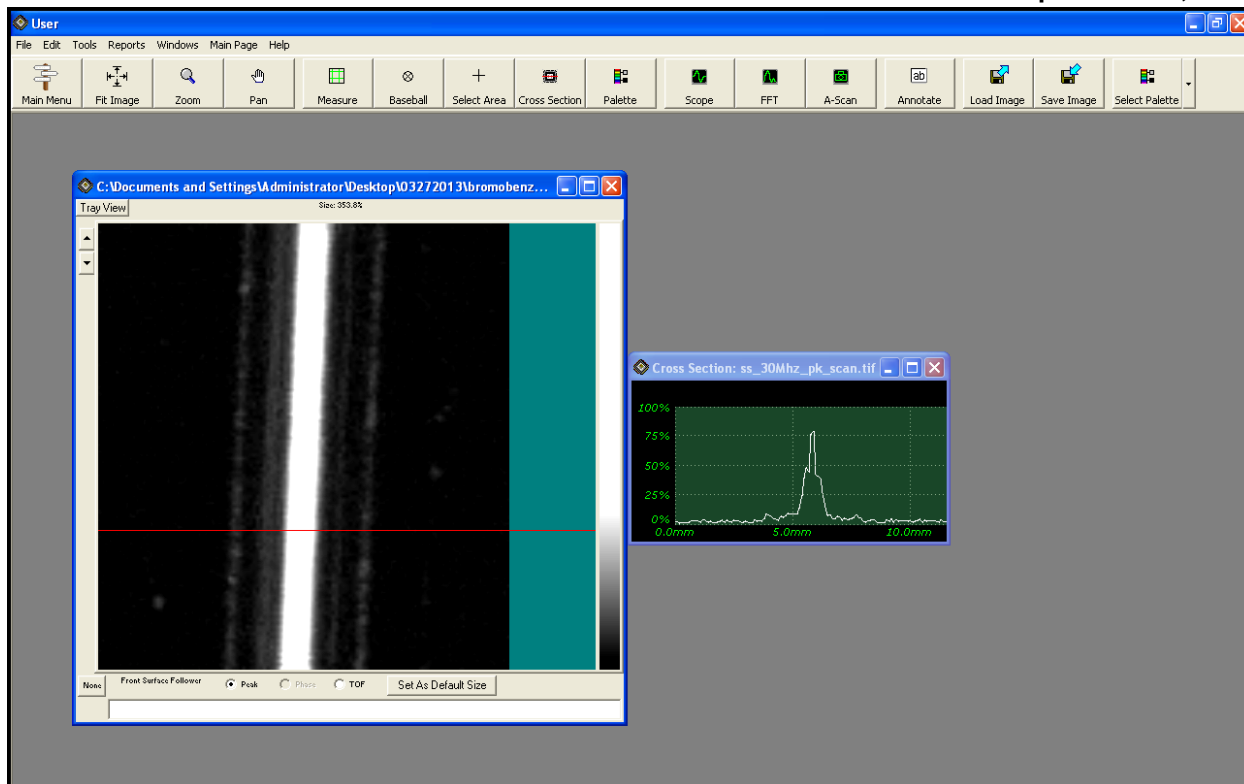


Figure 3.15. SAM Image for Stainless Steel Specimen in Bromobenzene

3.3.2 Resonant Ultrasound Spectroscopy Measurements

Parallelepiped specimens of Zr-4 were prepared for performing RUS measurements from a nominally 2-mm thick specimen of Zr-4 plate material from Allegheny Technologies Inc. (ATI). Initially, untreated (no hydrogen charging) specimens were fabricated by cutting out nine 3 mm × 5 mm × 2 mm specimens and then polishing them (see Figure 3.16). In addition, larger coupons were prepared for hydrogen charging that would then be cut into 3 mm × 5 mm × 2 mm specimens post-treatment. These coupons are shown in Figure 3.17.

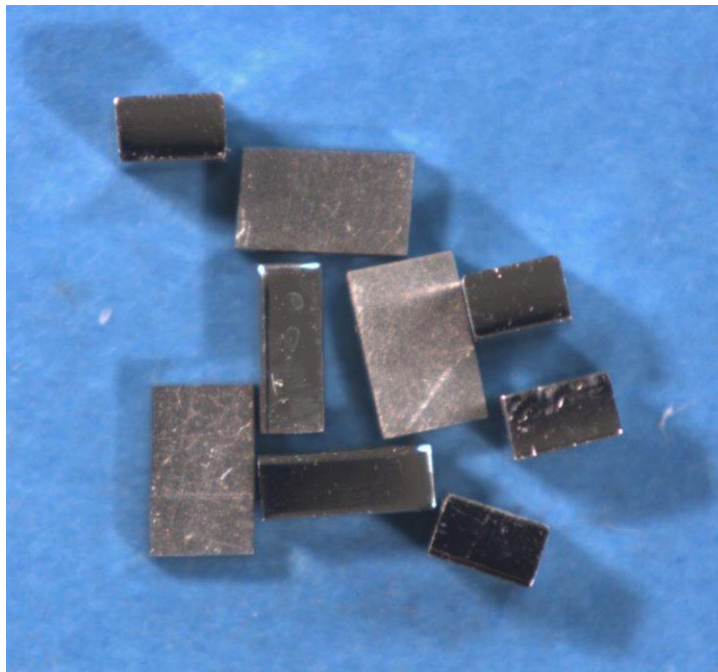


Figure 3.16. Photograph of Parallelepiped Specimens Fabricated from Zr-4 Plate (1.82 mm × 3 mm × 5 mm)

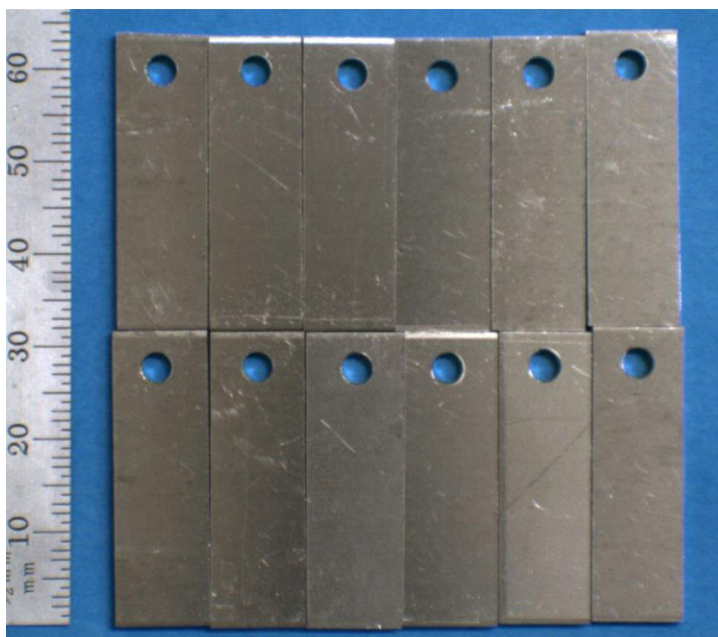


Figure 3.17. Photograph of Zr-4 Coupons Prepared for Hydrogen Charging

Prior to performing RUS measurements on the untreated specimens, the specimens were labeled, cleaned, weighed, and measured because this information is input into the RUS measurement system. A tabulation of this data for the nine uncharged specimens is included in Table 3.3. The mass density, ρ , for

each specimen is calculated based on the measured dimensions and weight of the specimens, and tabulated in the final column. It is clear that there is significant variance in the calculated densities and that they are consistently under the value of 6.55 g/cc reported by the vendor. The most likely explanation for this is that there are errors in the specimen geometry resulting from the cutting and/or polishing process. As a consequence, specimen UH06RM was initially selected for RUS measurements because its estimated mass density came closest to the reported mass density.

A photograph of the RUS setup with parallelepiped specimen UH06RM placed between two piezoelectric electrodes is shown in Figure 3.18. An example of a resonant spectra output is provided in Figure 3.19. To sort out frequency peaks associated with modes of the specimen of interest from modes from artifacts in the measurement setup, additional finite element method (FEM) modeling of the specimens was performed to confirm peaks observed in the spectrum. A comparison of the FEM modeling predictions with measurement observations for UH06RM is provided in Figure 3.20. Pretty good agreement between theory and experiment is observed for approximately the first 35 modes.

Table 3.3. Tabulation of Zr-4 Samples *Not* Charged with Hydrogen

Sample ID	Mass (g), uncertainty ± 0.0001 g	Length Dimension (mm), uncertainty ± 0.01 mm	Width Dimension (mm), uncertainty ± 0.01 mm	Thickness/Height Dimension (mm), uncertainty ± 0.01 mm	Mass Density (g/cc)
UH01RM	0.1816, 0.1816, 0.1816 Avg: 0.1816	4.88, 4.87, 4.88 Avg: 4.88	3.20, 3.20, 3.19 Avg: 3.20	1.85, 1.85, 1.85 Avg: 1.85	6.286 g/cc
UH02RM	0.1710, 0.1710, 0.1710 Avg: 0.1710	4.87, 4.87, 4.88 Avg: 4.87	2.95, 2.95, 2.95 Avg: 2.95	1.85, 1.85, 1.85 Avg: 1.85	6.434 g/cc
UH03RM	0.1740, 0.1740, 0.1741 Avg: 0.1740	4.86, 4.87, 4.86 Avg: 4.86	3.00, 3.00, 3.00 Avg: 3.00	1.85, 1.85, 1.85 Avg: 1.85	6.451 g/cc
UH04RM	0.1798, 0.1799, 0.1799, 0.1799 Avg: 0.1799	4.83, 4.83, 4.84 Avg: 4.83	3.18, 3.18, 3.18 Avg: 3.18	1.85, 1.85, 1.85 Avg: 1.85	6.331 g/cc
UH05RM	0.1785, 0.1785, 0.1785 Avg: 0.1785	4.87, 4.87, 4.87 Avg: 4.87	3.10, 3.10, 3.10 Avg: 3.10	1.85, 1.85, 1.85 Avg: 1.85	6.391 g/cc
UH06RM	0.1643, 0.1644, 0.1643 Avg: 0.1643	4.86, 4.86, 4.86 Avg: 4.86	2.83, 2.83, 2.83 Avg: 2.83	1.85, 1.85, 1.85 Avg: 1.85	6.457 g/cc
UH07RM	0.1834, 0.1834, 0.1834 Avg: 0.1834	4.85, 4.85, 4.85 Avg: 4.85	3.17, 3.17, 3.17 Avg: 3.17	1.85, 1.85, 1.85 Avg: 1.85	6.448 g/cc
UH08RM	0.1849, 0.1848, 0.1849 Avg: 0.1849	4.84, 4.84, 4.84 Avg: 4.84	3.23, 3.23, 3.23 Avg: 3.23	1.85, 1.85, 1.85 Avg: 1.85	6.393 g/cc
UH09RM	0.1804, 0.1804, 0.1804 Avg: 0.1804	4.85, 4.85, 4.85 Avg: 4.85	3.13, 3.13, 3.13 Avg: 3.13	1.85, 1.85, 1.85 Avg: 1.85	6.424 g/cc

The results of the RUS measurements performed on specimen UH06RM are summarized in Table 3.4. This table tabulates stiffness coefficients c_{11} and c_{44} and elastic moduli for specimen UH06RM and compares the results to vendor-specified properties. In this case, results for UH06RM are presented for two measurement modes: (1) the user-supplied specimen dimensions are kept fixed and (2) the user-supplied specimen dimensions are allowed to “float” with small adjustments made to reduce the overall error. In either case, the results are pretty similar. The c_{11} , c_{44} , and bulk modulus values are output by the RUS system while Young’s modulus and Poisson’s ratio are calculated from the values of the coefficients. The parameters with the most significant deviation from the vendor specifications include the c_{11} stiffness coefficient and the bulk modulus.

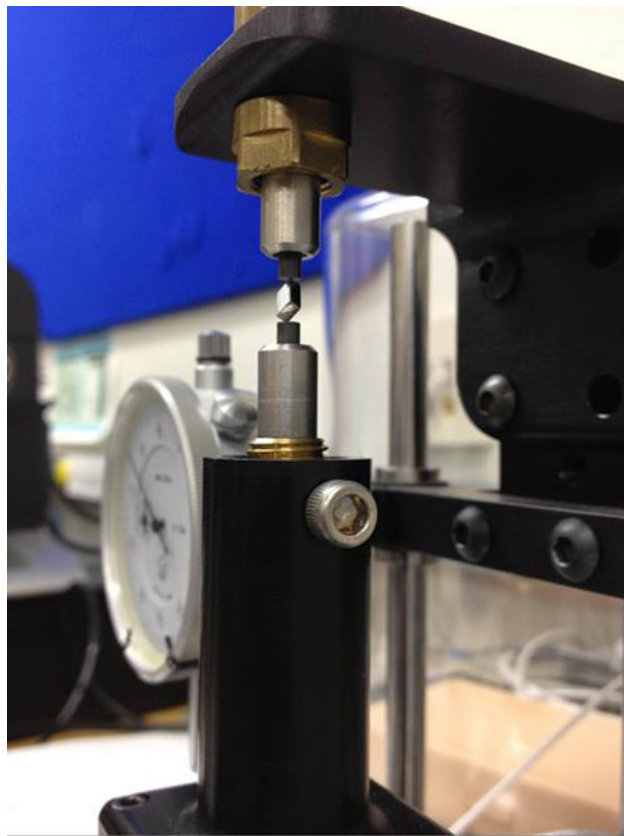


Figure 3.18. Placement of Parallelepiped Specimen UH06RM between Piezoelectric Transducers for Performance of RUS Measurement

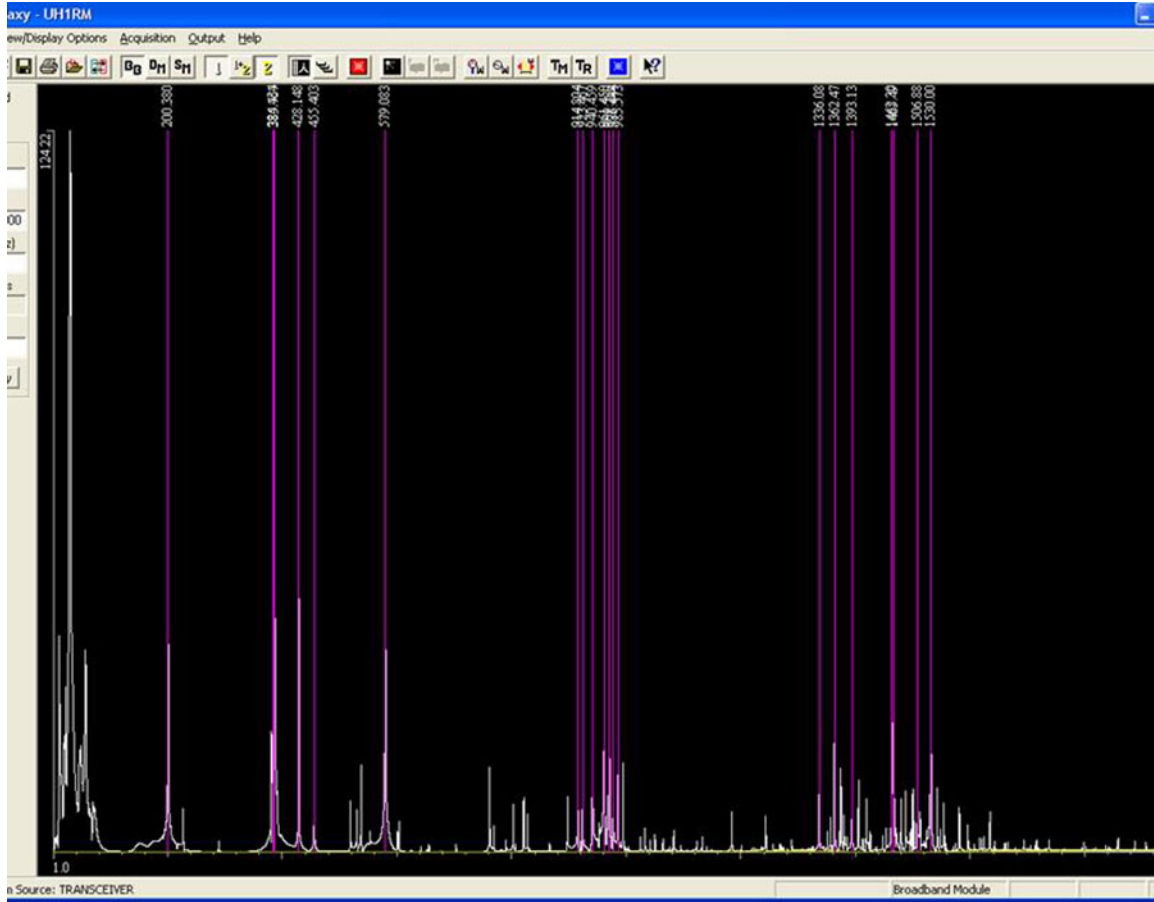


Figure 3.19. Example of Typical RUS Spectra Output; Obtained for Specimen UH1RM in this Case

Resonance Ultrasound Spectroscopy Measurements for
 Zr-4 Sample ID UHRM6

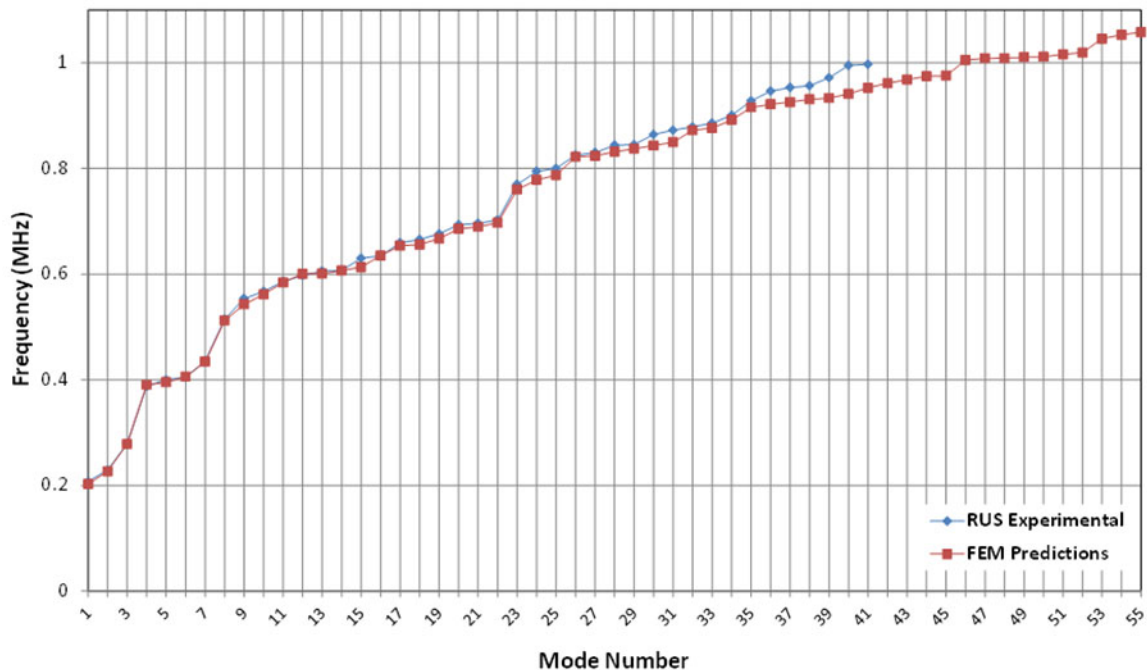


Figure 3.20. Comparison of FEM Modeling Predictions for Location of Spectral Peaks with Experimental Observations

Table 3.4. Tabulation of c11 and c44 Measurements and Values of c11 and c44 from Vendor Specifications

	c11	c44	Young's Modulus	Poisson's Ratio	Bulk Modulus
Vendor Specification	175.6 GPa	36.24 GPa	99.3 GPa	0.37	127.3
UH06RM w/ fixed dimensions	165.7 GPa	37.13 GPa	100.63 GPa	0.356	116.22
UH06RM w/ floating dimensions	166.2 GPa	37.13 GPa	100.71 GPa	0.356	116.69

3.3.3 Rayleigh Wave Velocity Measurements

Rayleigh wave velocity measurements were attempted on specimens using the apparatus shown in Figure 3.21. In this case, a pitch-catch mode is employed with the transmitter and receiver oriented near the Rayleigh angle for the specimen of interest; 5 MHz transducers with 0.5-in. diameters and 1-in. focal lengths are used for both transmit and receive. The apparatus allows adjustment of the distance between the transmit and receive transducers to facilitate $V(x)$ measurements of the Rayleigh velocity. Initially, a persistence scan was performed on a flat aluminum specimen in an attempt to recreate a scattering profile like that in Figure 3.6. An oscilloscope image for the persistence scan of the aluminum specimen is shown in Figure 3.22. The velocity is determined in a couple of different ways. First, the receiving transducer is translated in 1-mm increments with time-of-flight data recorded for the Rayleigh wave

signal at each increment. This data is plotted on a graph and a least-squares technique is used to fit a straight line to the data. Figure 3.23 shows the results of two $V(x)$ scans performed on the aluminum specimen with the slope of the lines equal to the velocity of the Rayleigh wave in inches/ μ sec. Alternatively, the data collected for Figure 3.23 is also provided in Table 3.5. In this case, each point in the scan may be treated as an individual measurement of velocity referenced back to the initial point of the scan. The individual measurements of velocity may be averaged and a standard deviation can be computed from the measurements. This information is provided in Table 3.5 as both inches/sec. and mm/sec. In this case, bold data entries represent outliers that were excluded from the calculations of average velocity and standard deviation. Velocities computed by fitting straight lines to the data as in Figure 3.23 are slightly lower than the velocity computed by averaging all of the measurements in Table 3.5.

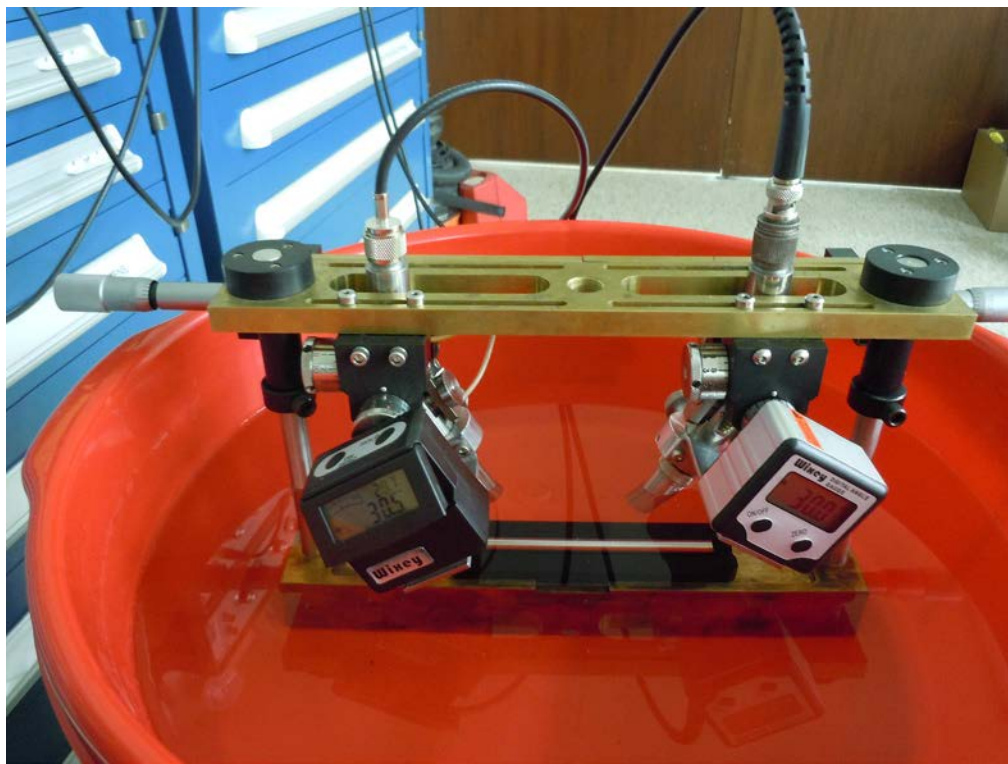


Figure 3.21. Apparatus for Performing Rayleigh Wave Velocity Measurements on Specimens

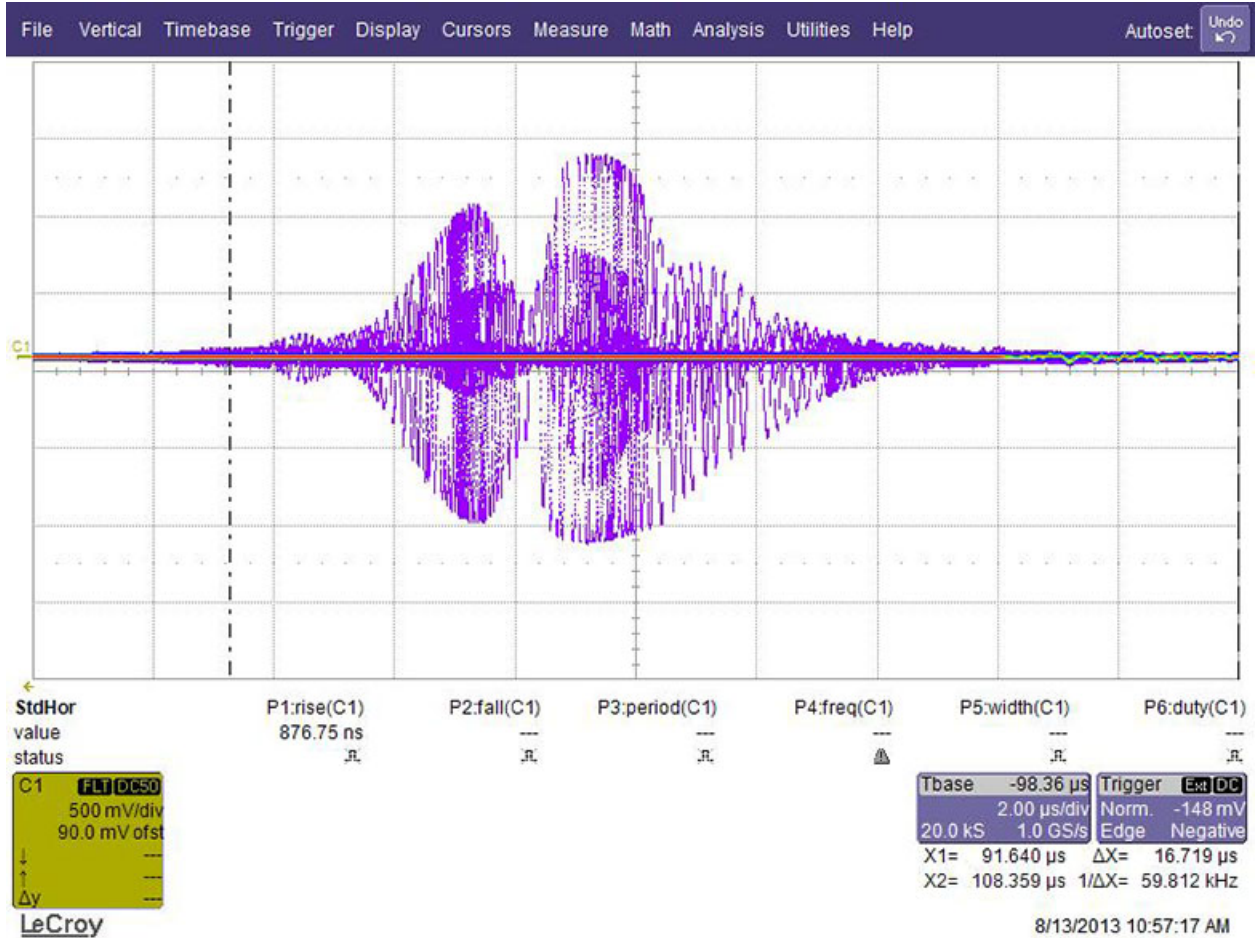


Figure 3.22. Persistence Scan of Scattered Profile for Flat Aluminum Specimen

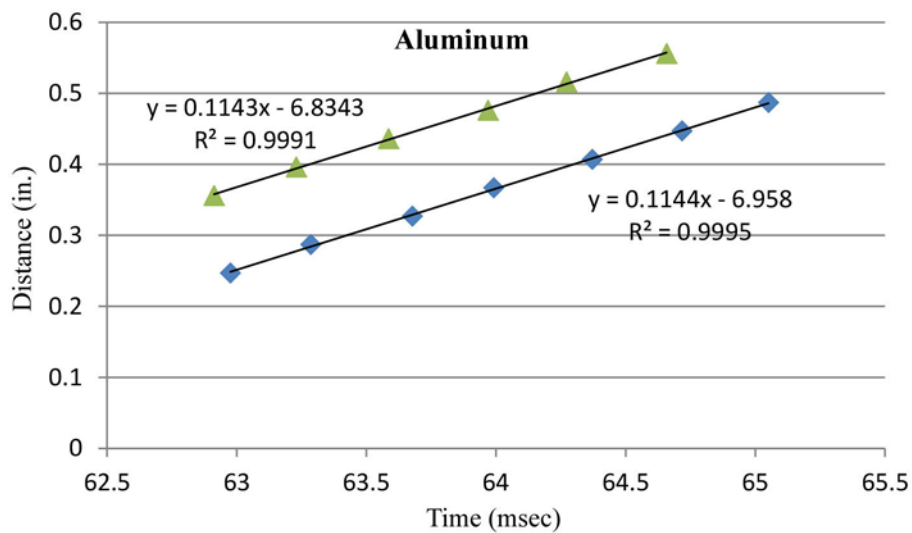


Figure 3.23. Results of Two V(x) Scans Performed on Flat Aluminum Specimen. The slope of the curves represents the Rayleigh velocity (in./μsec.).

Table 3.5. Summary of V(x) Scan Data for a Flat Aluminum Specimen

Scan 1			Scan 2		
Time (μs)	Distance (in.)	Velocity (in./μs)	Time (μs)	Distance (in.)	Velocity (in./μs)
62.9758	0.247		62.9128	0.356	
63.2862	0.287	0.1289	63.2298	0.396	0.1262
63.6778	0.327	0.1140	63.5858	0.436	0.1189
63.9914	0.367	0.1182	63.9692	0.476	0.1136
64.3716	0.407	0.1146	64.2718	0.516	0.1177
64.7176	0.447	0.1148	64.6580	0.556	0.1146
65.0510	0.487	0.1157	64.7910	0.596	0.1278
Average (in./μs)		0.1154	Average (in./μs)		0.1162
Std. Dev. (in./μs)		0.0016	Std. Dev. (in./μs)		0.0025
Average (mm/μs)		2.932	Average (mm/μs)		2.951
Std. Dev. (mm/μs)		0.041	Std. Dev. (mm/μs)		0.064

3.4 Summary, Conclusions, and Future Efforts

The status of FY13 efforts related to measurements of elastic properties of fuel cladding in an effort to characterize hydrogen effects is reflected in the bullets below. These bullets document several conclusions related to enhanced backscattering, resonant ultrasound spectroscopy, and Rayleigh velocity measurements performed or attempted in FY13:

- Enhanced backscattering was observed for a stainless steel tube specimen when immersed in multiple liquids.
- Backscatter peaks at the Rayleigh angle were not observed for Zr-4 tube specimens immersed in ethanol and water.
- The literature indicates that the amplitude of these backscatter peaks is dependent on the scattering inhomogeneity, perhaps caused by the surface roughness of the specimen or inherent material inhomogeneity in the specimen.
- Resonant ultrasound spectroscopy measurements performed on a parallelepiped specimen (UH06RM) of Zr-4 were consistent with vendor-provided specifications to within approximately 2.5% for the value of the stiffness coefficient c44 and within approximately 1.3% for Young’s modulus. However, larger discrepancies are observed for the c11 coefficient (approximately 5.6%) and the bulk modulus (approximately 8.7%).
- A tabulation of the measured dimensions and weights of nine initially prepared specimens exhibited considerable variability in the mass density calculated from those measurements. This indicates that the specimens exhibited significant deviations from ideal parallelepiped shapes and are a likely source of error observed.
- An apparatus and technique for performing Rayleigh velocity measurements on specimens has been demonstrated on a flat specimen of aluminum. The standard deviation of the measurements is reported to be on the order of 0.05 mm/μs.
- The literature indicates that ultrasonic velocity measurements have limited sensitivity to observe changes in hydrogen concentration with sensitivities on the order of 0.005 mm/μs change in velocity per 100 ppm of hydrogen concentration reported in the literature.

Based on these observations, several recommendations can be made with respect to future efforts.

Recommendations for future efforts include:

- Characterizing the surface roughness and microstructure of stainless steel and Zr-4 tube specimens used for enhanced backscatter measurements to determine if such measurements are feasible for Zr-4 materials (i.e., for instance, through appropriate surface polish or finish).
- Preparing better quality specimens for RUS measurements and exploring the possibility of performing RUS on more geometrically complex specimens (i.e., ring-shaped specimens representing cladding cross sections).
- Reducing the uncertainty in Rayleigh velocity measurements and attempting measurements on flat and tube-shaped Zr-4 specimens.
- Exploring the feasibility of performing $V(z)$ measurements of the Rayleigh velocity on specimens of interest, potentially using the same apparatus used for $V(x)$ measurements.
- Exploring non-linear Rayleigh wave measurements in an attempt to characterize hydrogen effects. Non-linear parameter measurements are typically more sensitive to distributed, pre-fracture forms of degradation than measurements of ultrasonic velocity.

4.0 REFERENCES

- Adams, R D, P Cawley, CJ Pye and BJ Stones. 1978. "A Vibration Technique For Non-destructively Assessing the Integrity of Structures." *Journal of Mechanical Engineering Science* 20:93-100.
- Auld BA. 1973. *Acoustic Fields and Waves in Solids, Volume 2*. Wiley and Sons. ISBN 047103701X 9780471037019. Chapter 10.
- Auld BA and JC Moulder. 1999. "Review of Advances in Quantitative Eddy Current Nondestructive Evaluation." *Journal of Nondestructive Evaluation* 18(1):3-36.
- Beissner RE. 1994. "Slots vs. Cracks in Eddy Current NDE." *Journal of Nondestructive Evaluation* 13(4):175-183.
- Bertoni HL and T Tamir. 1973. "Unified Theory of Rayleigh-Angle Phenomena for Acoustic Beams at Liquid-Solid Interfaces." *Applied Physics* 2:157-172.
- Billone M, Y Yan, T Burtseva and R Daum. 2008. *Cladding Embrittlement during Postulated Loss-of-Coolant Accidents*. NUREG/CR-6967, U.S. Nuclear Regulatory Commission, Washington, D.C. ADAMS Accession No. ML082130389.
- Billone MC, TA Burtseva and RE Einziger. 2013. "Ductile-to-Brittle Transition Temperatures for High-Burnup Cladding Alloys Exposed to Simulated Drying-Storage Conditions." *Journal of Nuclear Materials* 433:431-448.
- Bowler JR. 1994. "Eddy-current Interaction with an Ideal Crack. I. The Forward Problem." *Journal of Applied Physics* 75(12):8128-8137.
- Bowler JR. 2002. "Thin-skin Eddy-current Inversion for the Determination of Crack Shapes." *Inverse Problems* 18(6):1891-1905.
- Bowler JR, SJ Norton and DJ Harrison. 1994. "Eddy-current Interaction with an Ideal Crack. II. The Inverse Problem." *Journal of Applied Physics* 75(12):8138-8144.
- Burke SK. 1988. "A Benchmark Problem for Computation of ΔZ in Eddy-Current Nondestructive Evaluation (NDE)." *Journal of Nondestructive Evaluation* 7(1/2):35-41.
- Caseres L and TS Mintz. 2010. *Atmospheric Stress Corrosion Cracking Susceptibility of Welded and Unwelded 304, 304L, and 316L Austenitic Stainless Steels Commonly Used for Dry Cask Storage Containers Exposed to Marine Environments*. NUREG/CR-7030, U.S. Nuclear Regulatory Commission, Washington, D.C.
- Cheeke JDN. 2002. *Fundamentals and Applications of Ultrasonic Waves*. CRC Press, Boca Raton. ISBN 0849301300.
- Cumblidge SE, MT Anderson and SR Doctor. 2004. *An Assessment of Visual Testing*. NUREG/CR-6860, U.S. Nuclear Regulatory Commission, Washington, D.C.
- Cumblidge SE, MT Anderson, SR Doctor, FA Simonen and AJ Elliot. 2007. *A Study of Remote Visual Methods to Detect Cracking in Reactor Components*. NUREG/CR-6943, PNNL-16472, U.S. Nuclear Regulatory Commission, Washington, D.C.

- de Billy M and L Adler. 1982. "Parameters Affecting Backscattered Ultrasonic Leaky-Rayleigh Waves from Liquid-Solid Interfaces." *Journal of the Acoustical Society of America* 72(3):1018-1020.
- de Billy M and G Quentin. 1982. "Backscattering of Acoustic Waves by Randomly Rough Surfaces of Elastic Solids Immersed in Water." *Journal of the Acoustical Society of America* 72(2):591-601.
- De PK, JT John, S Banerjee, T Jayakumar, M Thavasimuthu and B Raj. 1998. "Assessment of Hydrogen Levels in Zircaloy-2 by Non-destructive Testing." *Journal of Nuclear Materials* 252(1-2):43-54.
- Doebling SW, CR Farrar and MB Prime. 1998. "A Summary Review of Vibration-based Identification Methods." *The Shock and Vibration Digest* 205:531-545.
- Gómez MP, G Domizzi, MIL Pumarega and JE Ruzzante. 2006. "Characterization of Hydrogen Concentration in Zircaloy-4 Using Ultrasonic Techniques." *Journal of Nuclear Materials* 353(3):167-176.
- Hanson BD, H Alsaed, C Stockman, D Enos, RM Meyer and K Sorenson. 2012. *Used Fuel Disposition Campaign - Gap Analysis to Support Extended Storage of Used Nuclear Fuel, Rev. 0*. FCRD-USED-2011-000136 Rev. 0, PNNL-20509, U.S. Department of Energy, Washington, D.C.
- Hanson BD, R Shimskey, C Lavender, PJ MacFarlan and P Eslinger. 2013. *Used Fuel Disposition Campaign -- Hydride Rim Formation in Unirradiated Zircaloy*. FCRD-USED-2013-000151, PNNL-22438, Pacific Northwest National Laboratory, Richland, Washington.
- Heasler PG and SR Doctor. 1996. *Piping Inspection Round Robin*. NUREG/CR-5068, PNL-10475, U.S. Nuclear Regulatory Commission, Washington, D.C.
- Heasler PG and SR Doctor. 2003. *A Comparison of Three Round Robin Studies on ISI Reliability of Wrought Stainless Steel Piping*. NUREG/CR-6795, PNNL-13873, U.S. Nuclear Regulatory Commission, Washington, D.C.
- Heasler PG, TT Taylor, JC Spanner, SR Doctor and JD Deffenbaugh. 1990. *Ultrasonic Inspection Reliability for Intergranular Stress Corrosion Cracks: A Round Robin Study of the Effects of Personnel, Procedures, Equipment and Crack Characteristics*. NUREG/CR-4908, PNL-6179, U.S. Nuclear Regulatory Commission, Washington, D.C.
- Huang H and T Takagi. 2002. "Inverse Analyses for Natural and Multicracks Using Signals from a Differential Transmit-Receive ECT Probe." *IEEE Transactions on Magnetics* 38(2):1009-1012.
- Liu I-H and C-H Yang. 2006. "Nondestructive Characterization of Zircaloy Tubes with Hydride Rims." In *12th Asia-Pacific Conference on Non-Destructive Testing 2006 (APCNDT 2006)*. November 5-10, 2006, Auckland, New Zealand.
- Liu I-H and C-H Yang. 2008. "Laser Ultrasound Technique for Nondestructive Characterization of Material Properties in Hydrogen-Charged Zircaloy Tubes." In *1st International Symposium on Laser Ultrasonics: Science, Technology and Applications*. July 16-18, 2008, Montreal, Canada.
- Meyer R, A Pardini, B Hanson and K Sorenson. 2013. *Review of NDE Methods for Detection and Monitoring of Atmospheric SCC in Welded Canisters for the Storage of Used Nuclear Fuel*. PNNL-22158, Pacific Northwest National Laboratory, Richland, Washington.

Nagy PB and L Adler. 1989. "On the Original of Increased Backward Radiation from a Liquid-Solid Interface at the Rayleigh Angle." *Journal of the Acoustical Society of America* 85(3):1355-1357.

Nagy PB and L Adler. 1994. "Increased Incoherent Backscattering from a Liquid-Solid Interface at the Rayleigh Angle." *Journal of the Acoustical Society of America* 98(4):2537-2545.

Nath R, J Schwarz, MK Johnson, J Long and J Saxton. 2004. "Correlation of Quasar Resonant Inspection Measurements with Yield Force in Powder Metal Parts." In *Proceedings of the 2004 International Conference on Powder Metallurgy and Particulate Materials*, pp. 11-1-7. June 13-17, 2004, Chicago, Illinois. Metal Powder Industries Federation, Princeton, New Jersey.

Neuenschwander J, T Schmidt, T Luthi and M Romer. 2006. "Leaky Rayleigh Wave Investigation on Mortar Samples." *Ultrasonics* 45(1-4):50-55.

Norris AN. 1983. "Back Reflection of Ultrasonic Waves from a Liquid-Solid Interface." *Journal of the Acoustical Society of America* 73(2):427-434.

NRC. 2011. *Contaminants and Stagnant Conditions Affecting Stress Corrosion Cracking in Stainless Steel Piping in Pressurized Water Reactors*. NRC Information Notice 2011-04, U.S. Nuclear Regulatory Commission (NRC), Washington, D.C. ADAMS Accession No. ML103410363.

Wåle J. 2006. *Crack Characterisation for In-service Inspection Planning - An Update*. SKI Report 2006:24, Swedish Nuclear Power Inspectorate, Stockholm, Sweden.

Yang C-H and M-F Huang. 2004. "Non-destructive Characterization of Hydrogen Concentration in Zircaloy." *Key Engineering Materials* 270-273:89-95.

Yang C-H and Y-A Lai. 2006. "Nondestructive Characterization Hydrogen-Charged Zircalloys with a Laser Ultrasound Technique." *Key Engineering Materials* 321-323:410-413.

Yeh C-H and C-H Yang. 2010. "Characterization of Hydride Orientation in Zircaloy Cladding Tubes with a Laser Ultrasound Technique." In *Proceedings of the 30th Symposium on UltraSonic Electronics (USE2009)*, pp. 227-228. November 18-20, 2009, Kyoto City, Japan.

Yu Z and S Boseck. 1995. "Scanning Acoustic Microscopy and Its Applications to Material Characterization." *Reviews of Modern Physics* 67(4):863-891.

Yusa N, Z Chen, K Miya, T Uchimoto and T Takagi. 2003. "Large-Scale Parallel Computation for the Reconstruction of Natural Stress Corrosion Cracks from Eddy Current Testing Signals." *NDT & E International* 36(7):449-459.

Yusa N, W Cheng, Z Chen and K Miya. 2002. "Generalized Neural Network Approach to Eddy Current Inversion for Real Cracks." *NDT & E International* 35(8):609-614.

Yusa N, H Huang and K Miya. 2007a. "Numerical Evaluation of the Ill-Posedness of Eddy Current Problems to Size Real Cracks." *NDT & E International* 40(3):185-191.

Yusa N and K Miya. 2009. "Discussion on the Equivalent Conductivity and Resistance of Stress Corrosion Cracks in Eddy Current Simulations." *NDT & E International* 42(1):9-15.

Yusa N, S Perrin, K Mizuno, Z Chen and K Miya. 2007b. "Eddy Current Inspection of Closed Fatigue and Stress Corrosion Cracks." *Measurement Science and Technology* 18(11):3403-3408.

Appendix A: Specimens for Eddy Current Evaluation

A-1. EDM Verification Plate

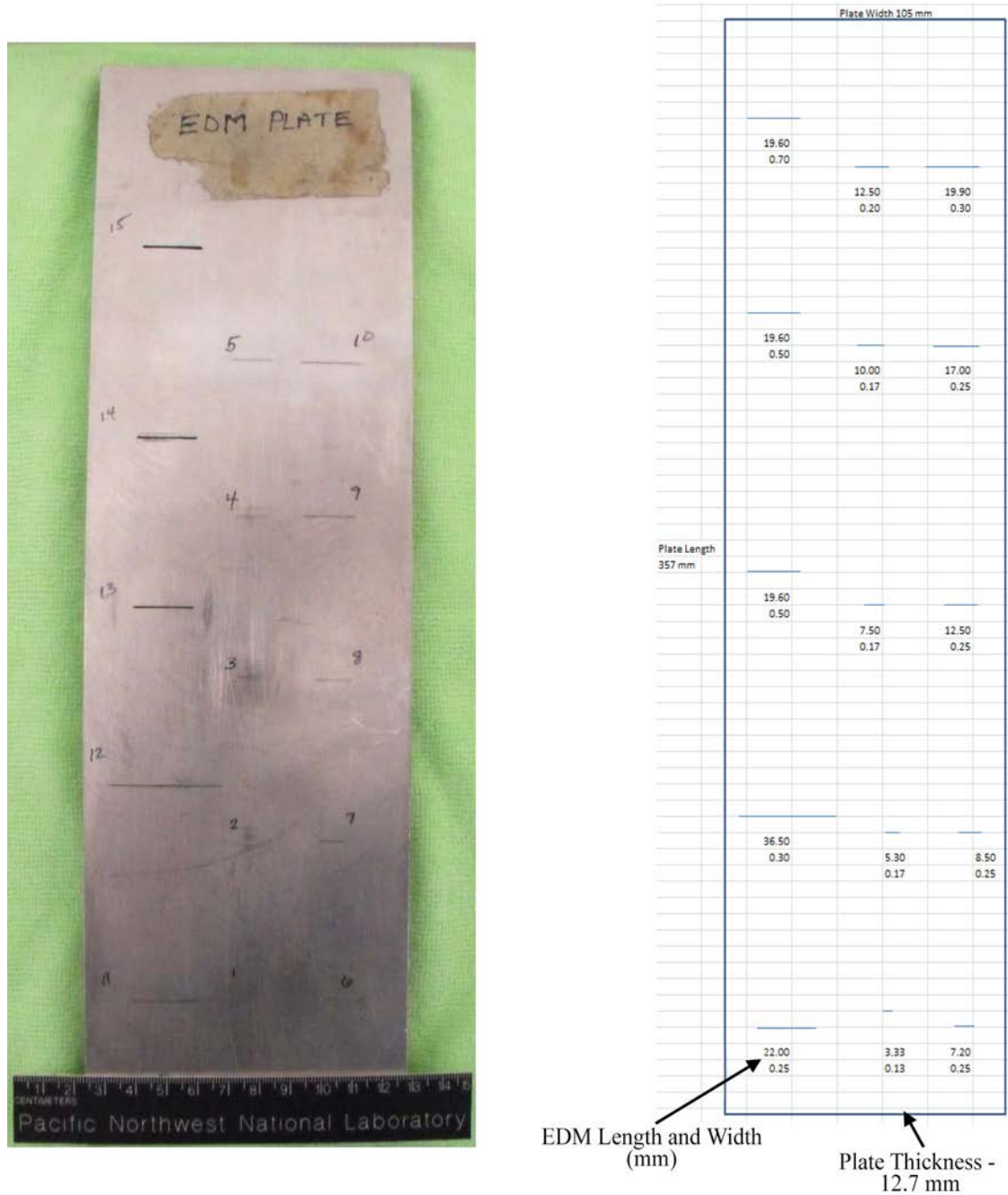


Figure A.1. EDM Plate. Gross measurements taken with Vernier calipers.

A.2

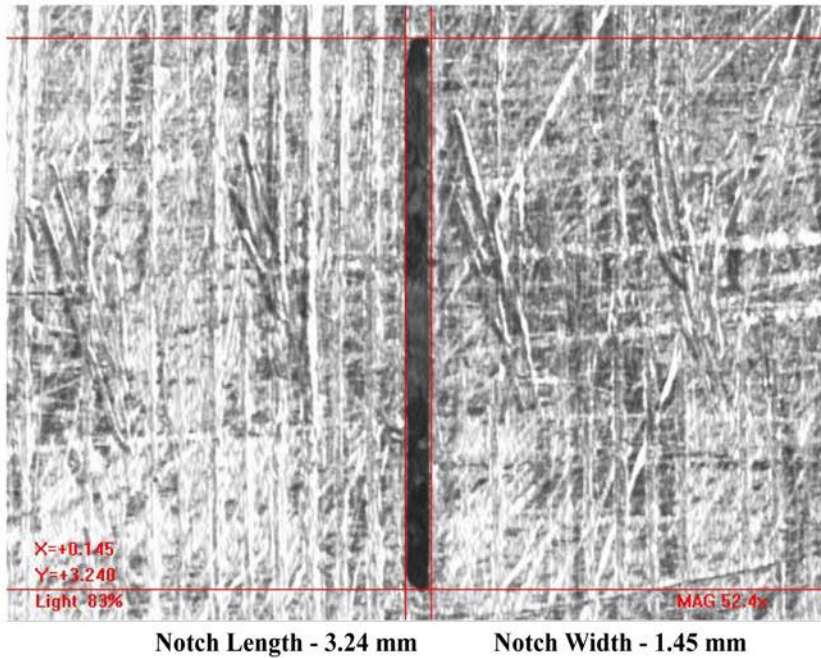
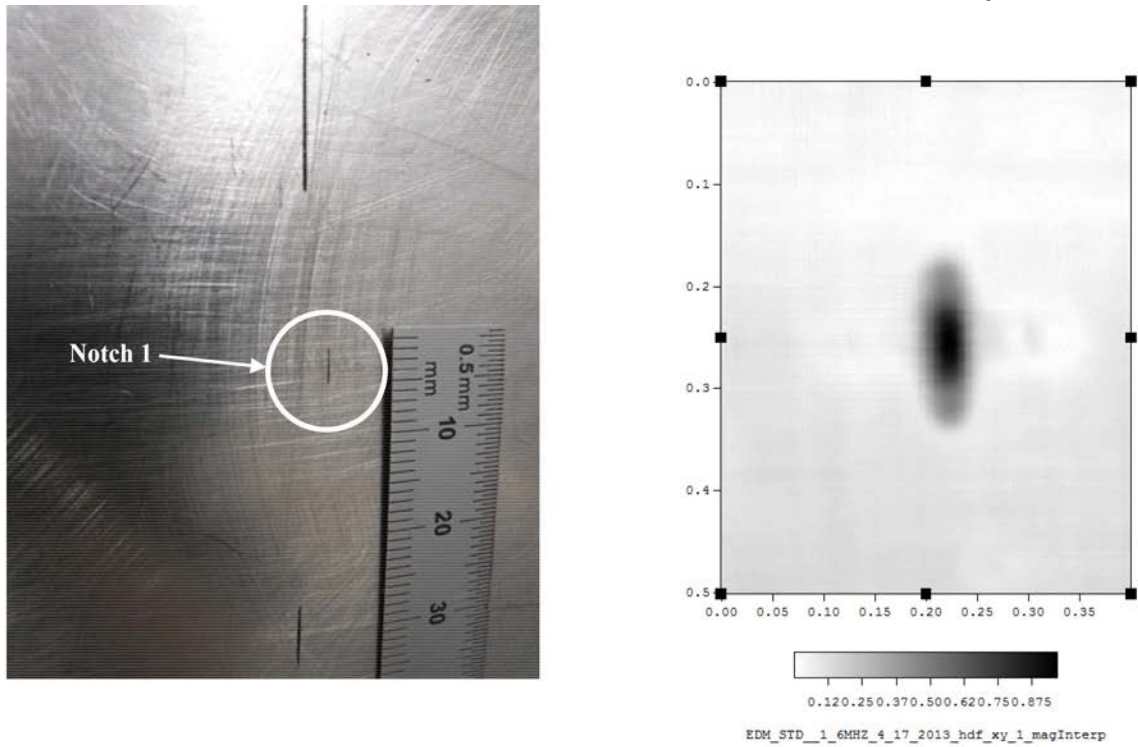


Figure A.2. EDM Notch 1, ET Scan (inches) and Optical Microscopy Measurement (mm)

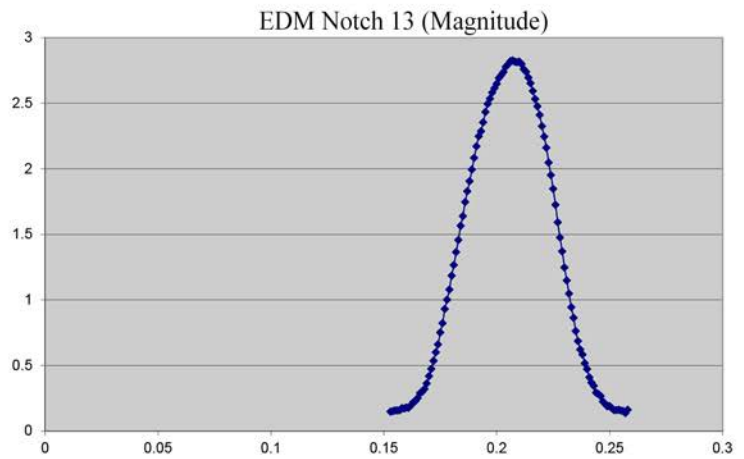
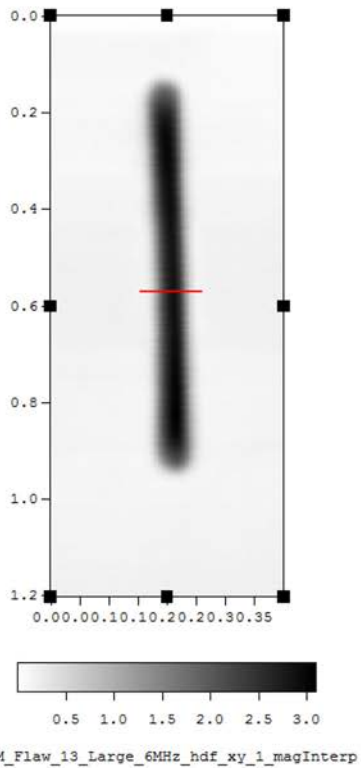
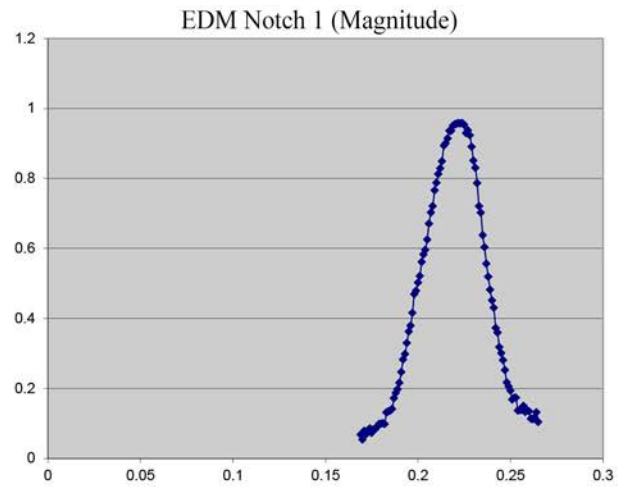
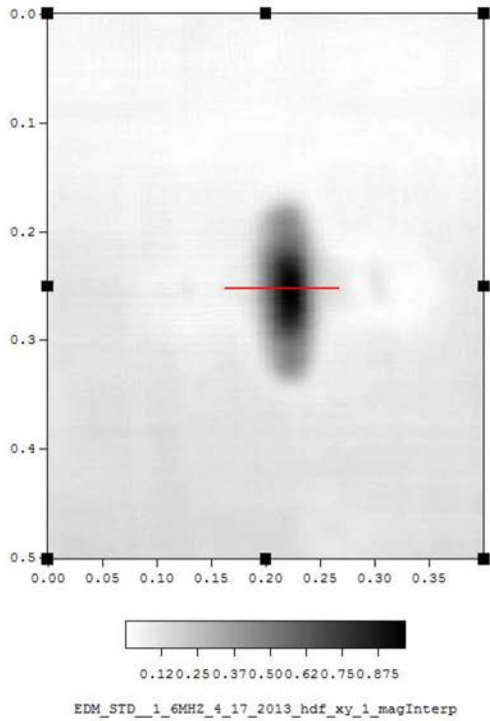


Figure A.3. Single Line Plots of Magnitude of Both Notch 1 and Notch 13 (aspect ratio correct)

A.4

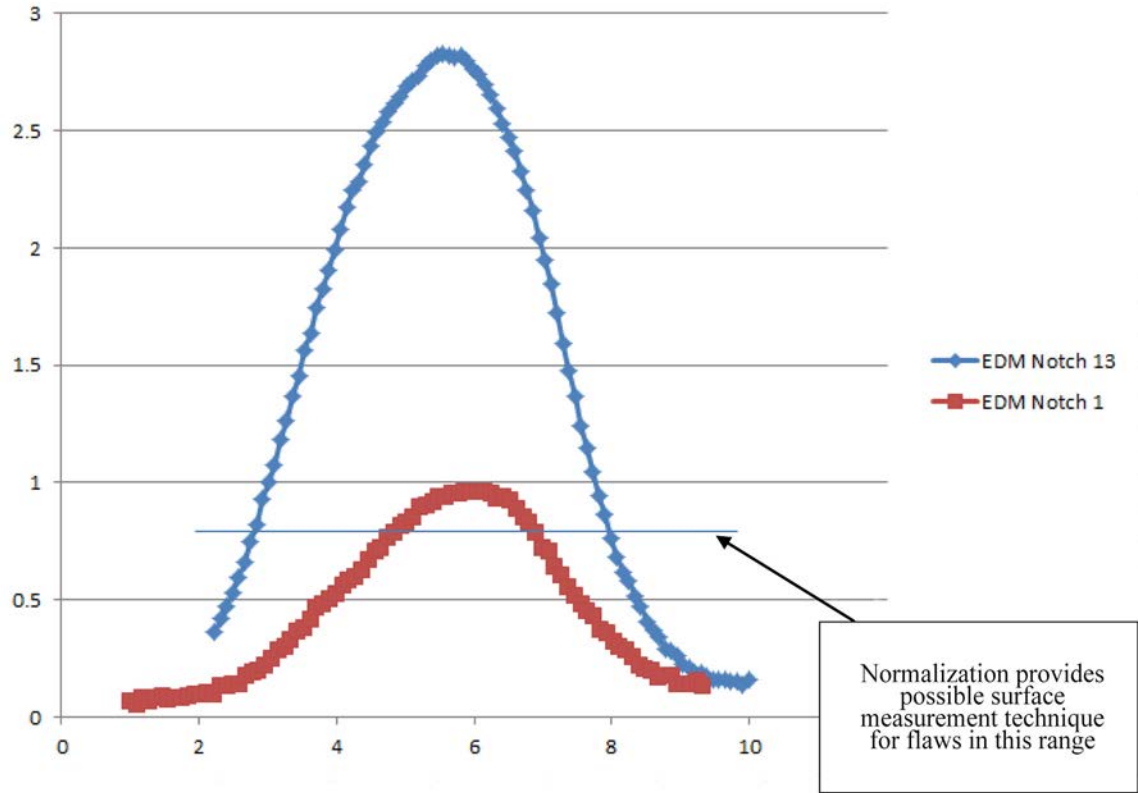


Figure A.4. Normalization of EDM Notches 1 and 13

A.6

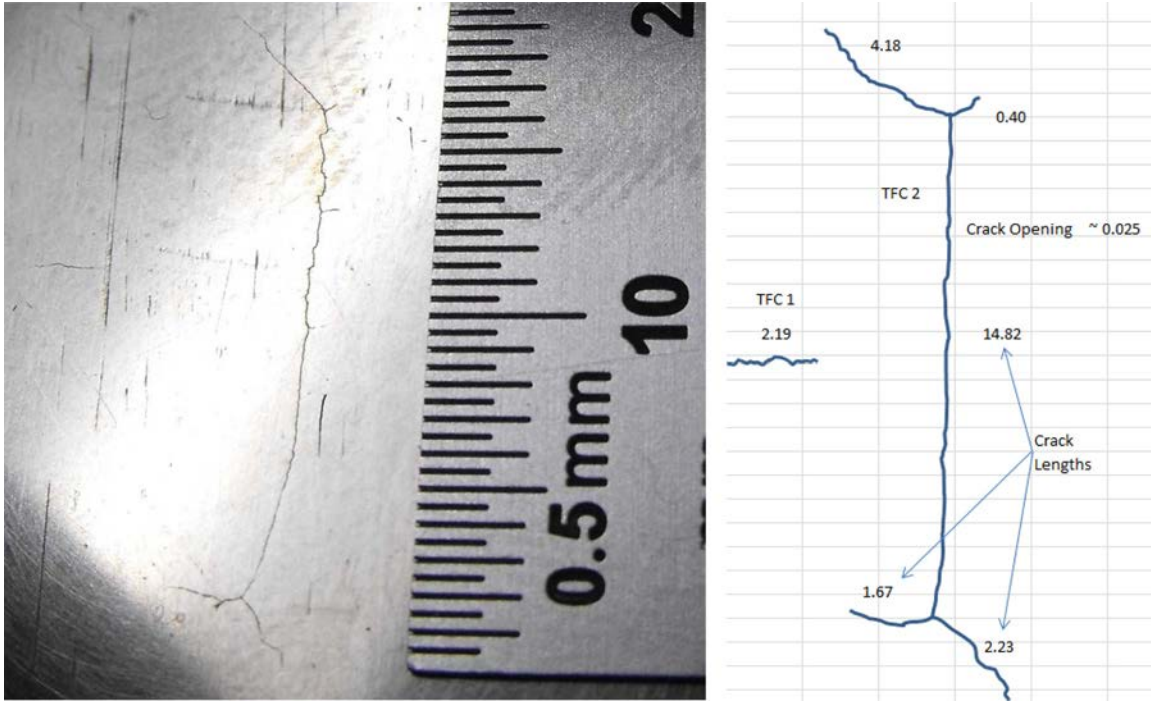


Figure A.6. TFC Specimen B-117. Gross measurements taken with Vernier calipers.

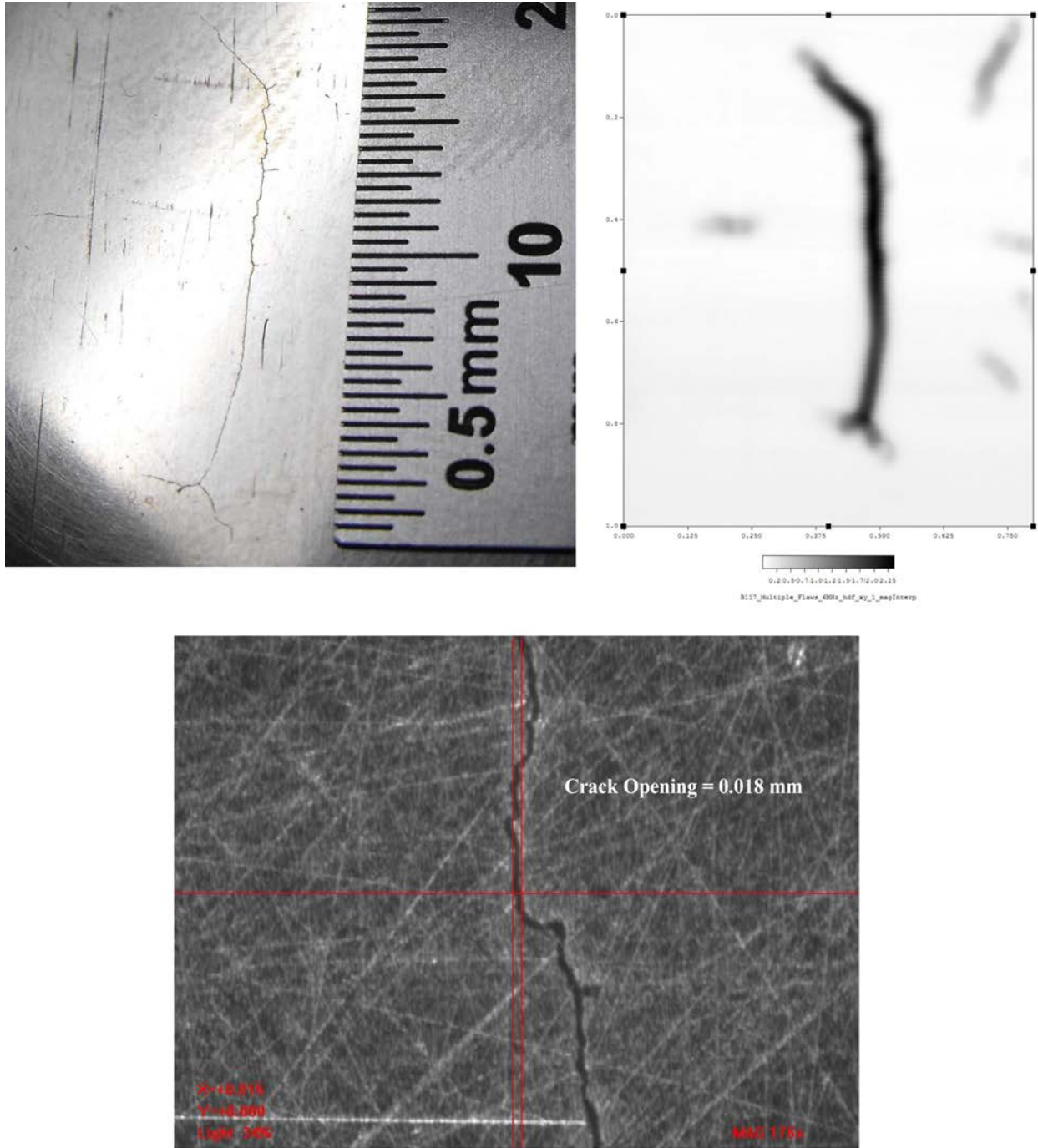


Figure A.7. TFC in B-117, ET Scan (inches), and Optical Microscopy Measurement (mm)

A.8

A-3. Specimen B-118

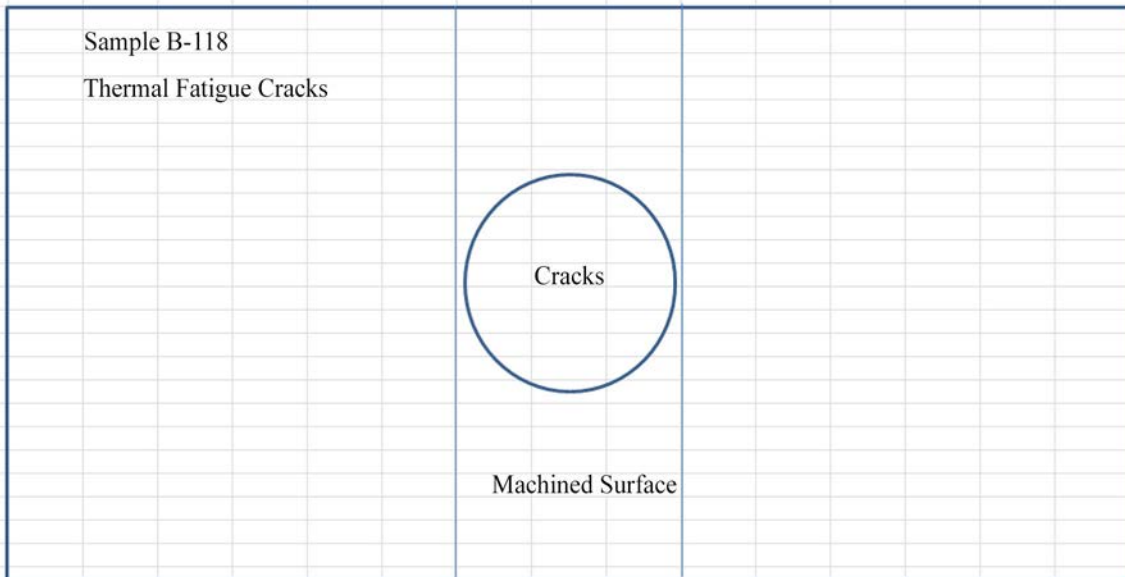


Figure A.8. Thermal Fatigue Crack Specimen B-118

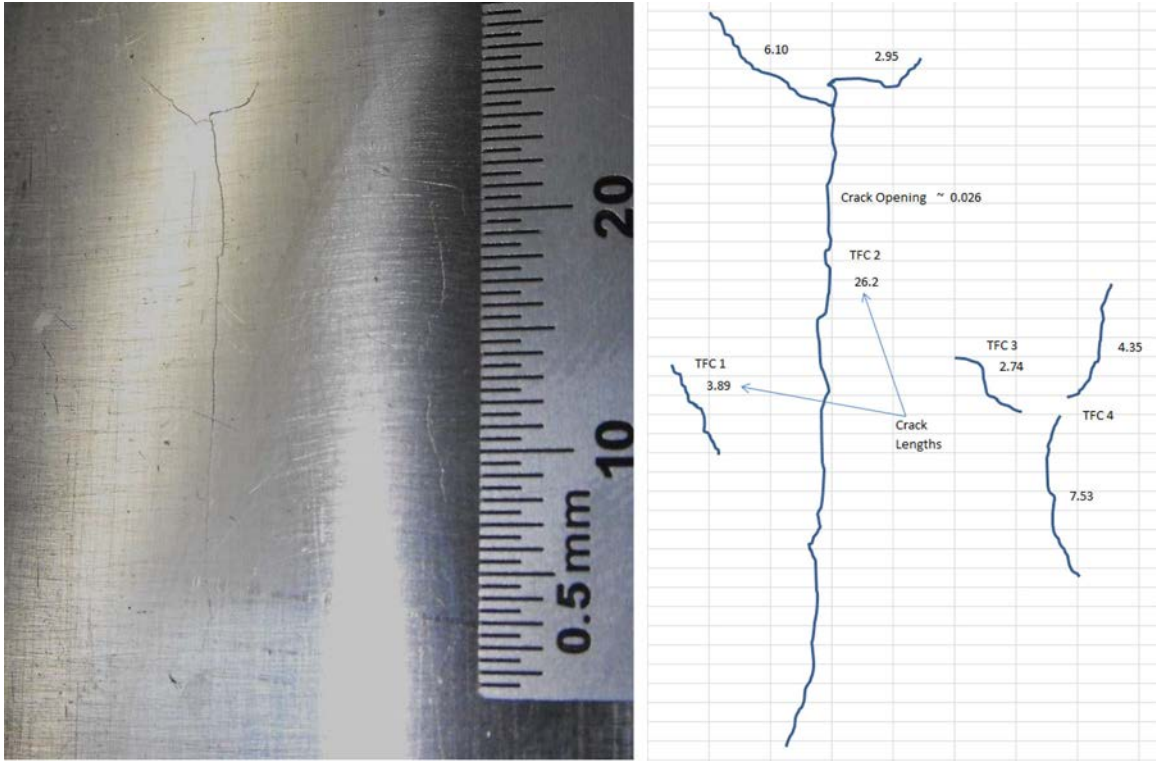
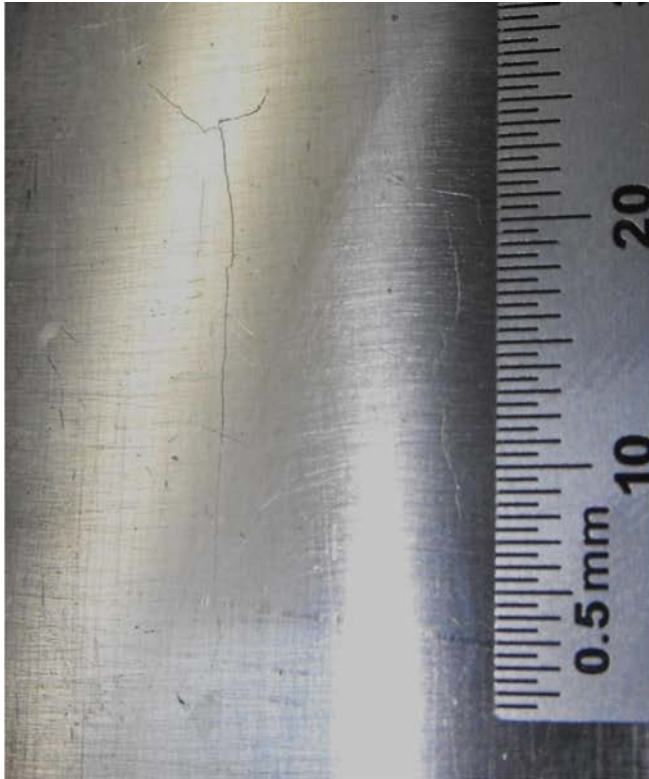


Figure A.9. TFC Specimen B-118. Gross measurements taken with Vernier calipers.

A.10



No eddy current scan was performed on B-118

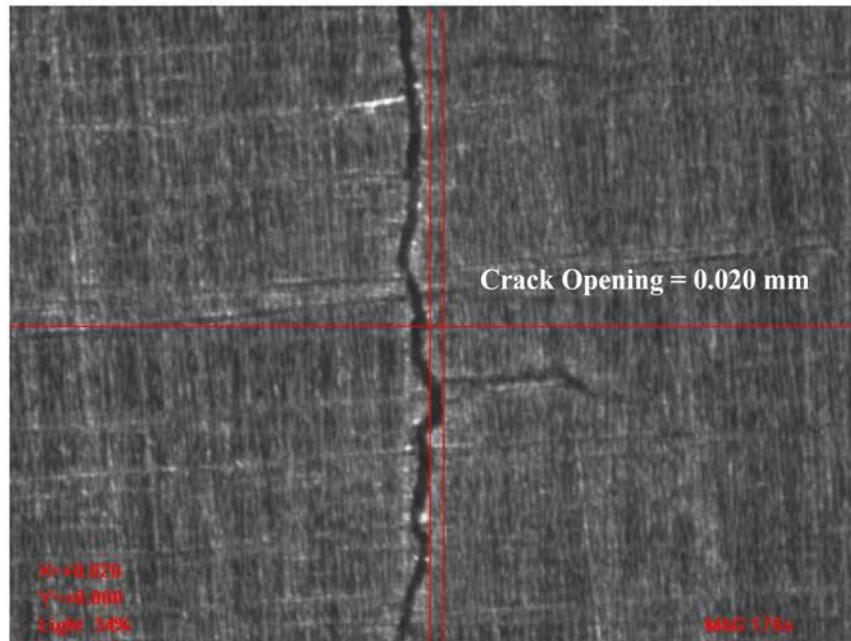


Figure A.10. TFC in B-118 and Optical Microscopy Measurement (mm)

A-4. Specimen 07-343




			Machined surface
			
Flaw 1 Crack		Flaw 2 Not visible	Flaw 3 Not visible

Figure A.11. Crack Specimen 07-343

A.12



Length - 12.4 mm
Crack Opening - 0.060 mm

Figure A.12. Crack Specimen 07-343. Gross measurements taken with Vernier calipers.

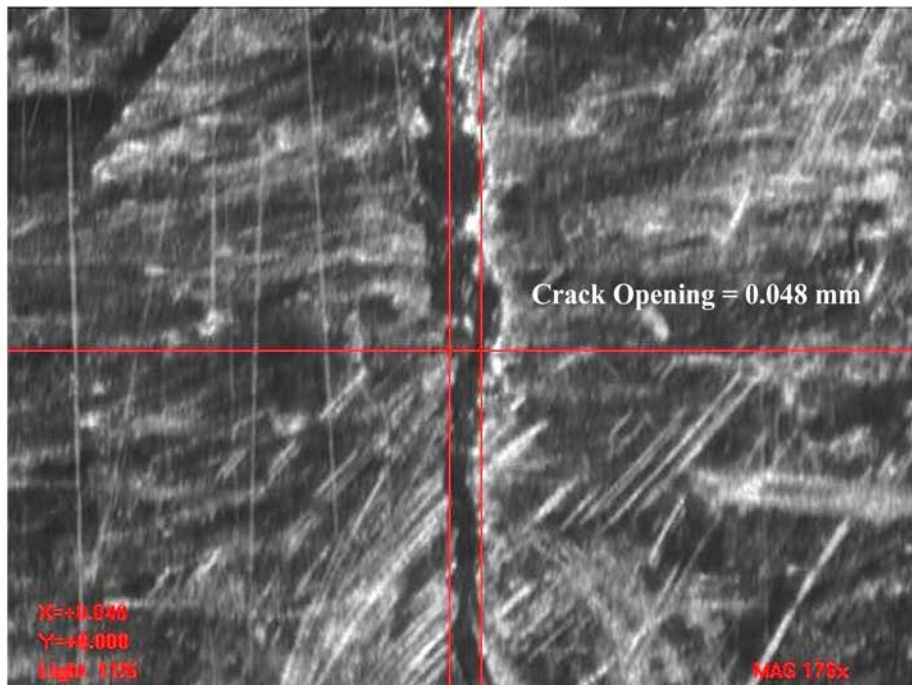
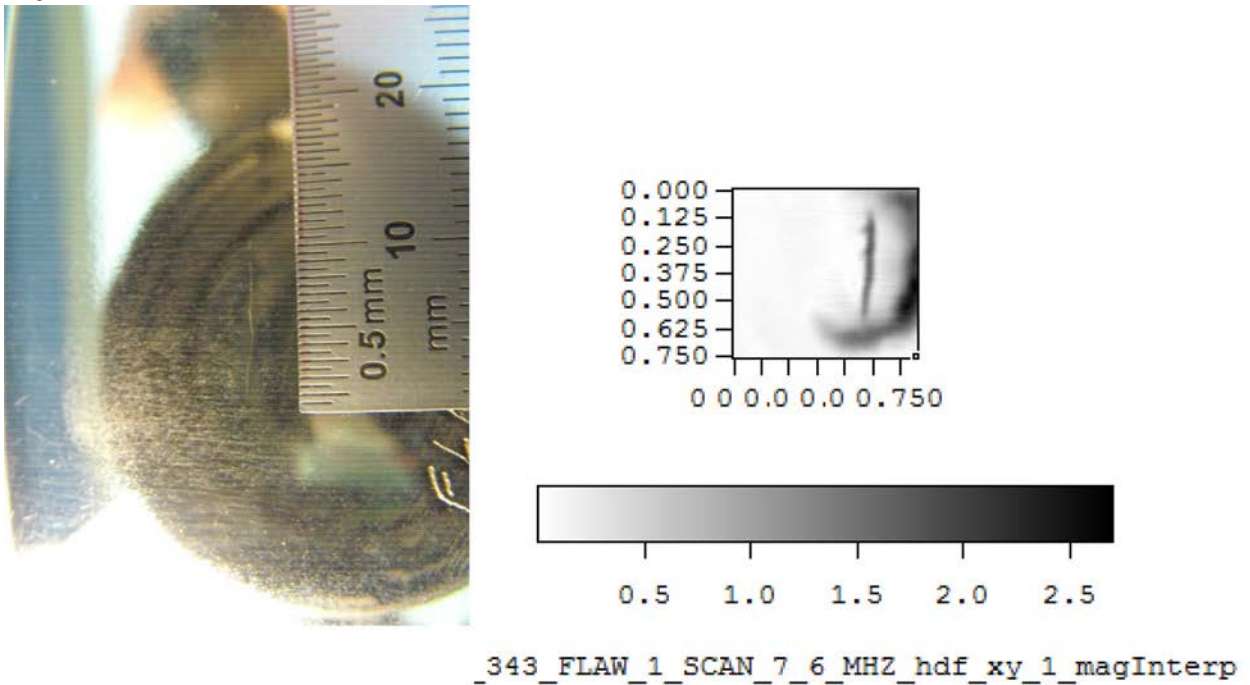


Figure A.13. Crack in 07-343, ET Scan (inches), and Optical Microscopy Measurement (mm)

A.14

A-5. Specimen D2



Sample D2-3 cut from pipe and sectioned

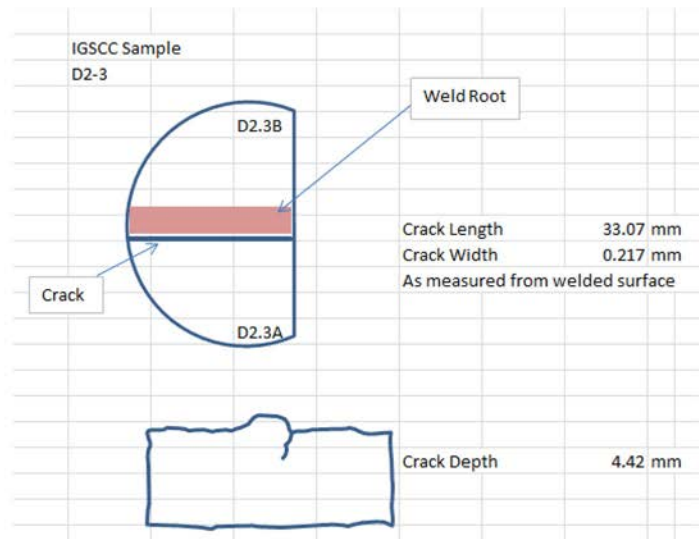
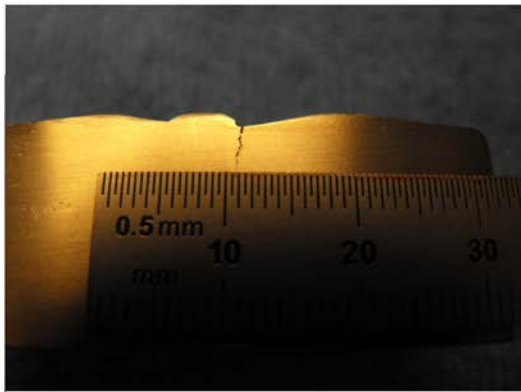
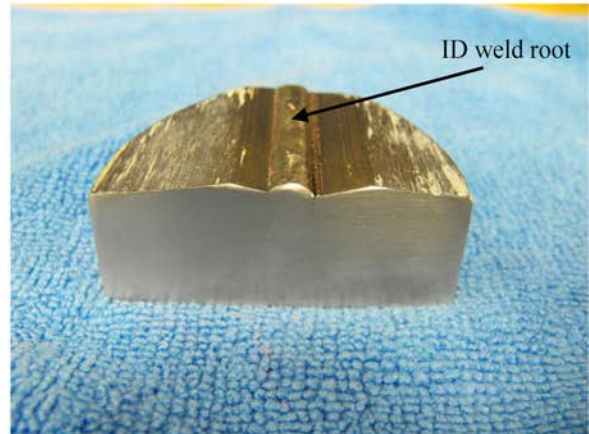
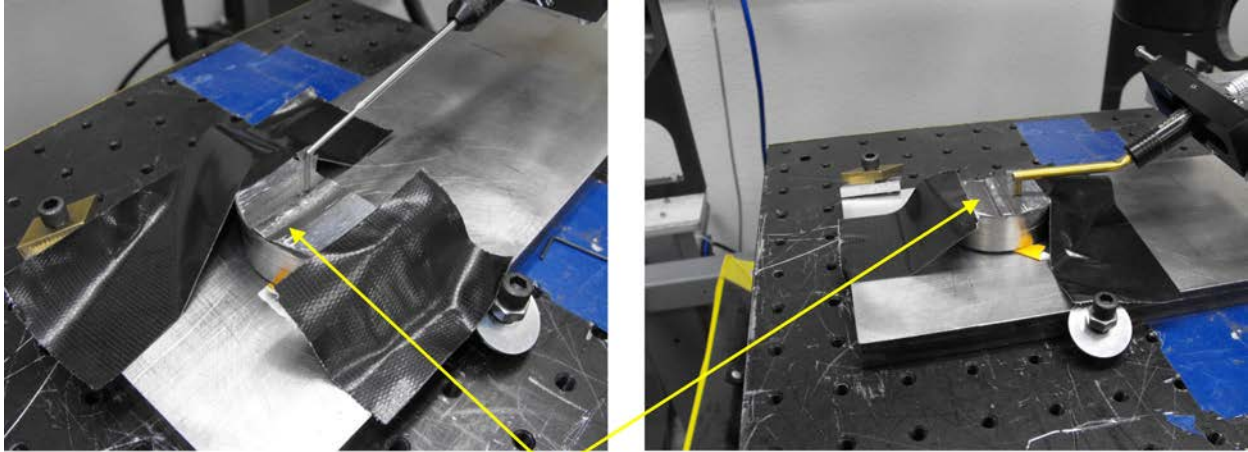


Figure A.14. IGSCC Crack Specimen D2-3



ET parallel and perpendicular scans of the weld root in the as-found condition yielded poor results. Decision was made to surface the weld root.

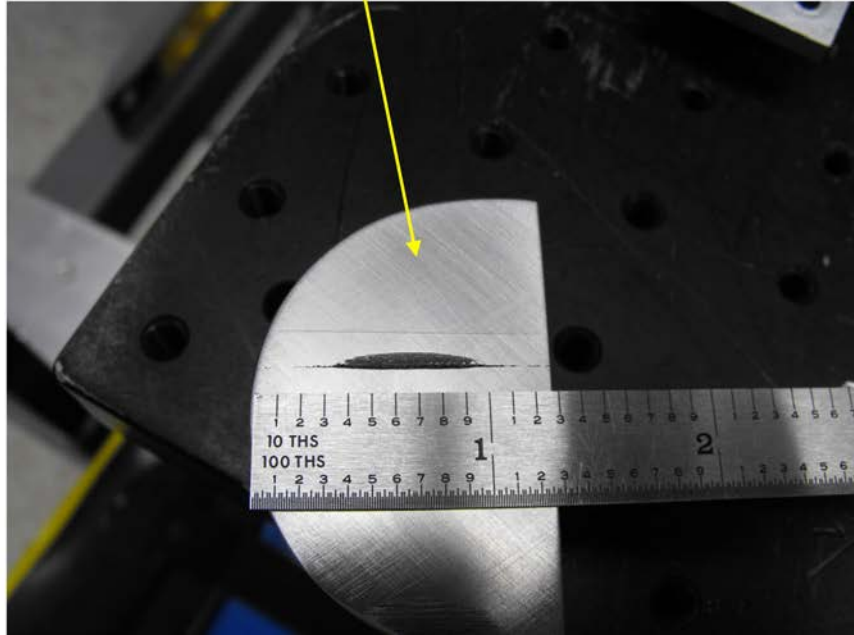


Figure A.15. ET Scan of Sample D2-3 and Sample Machining

A.16

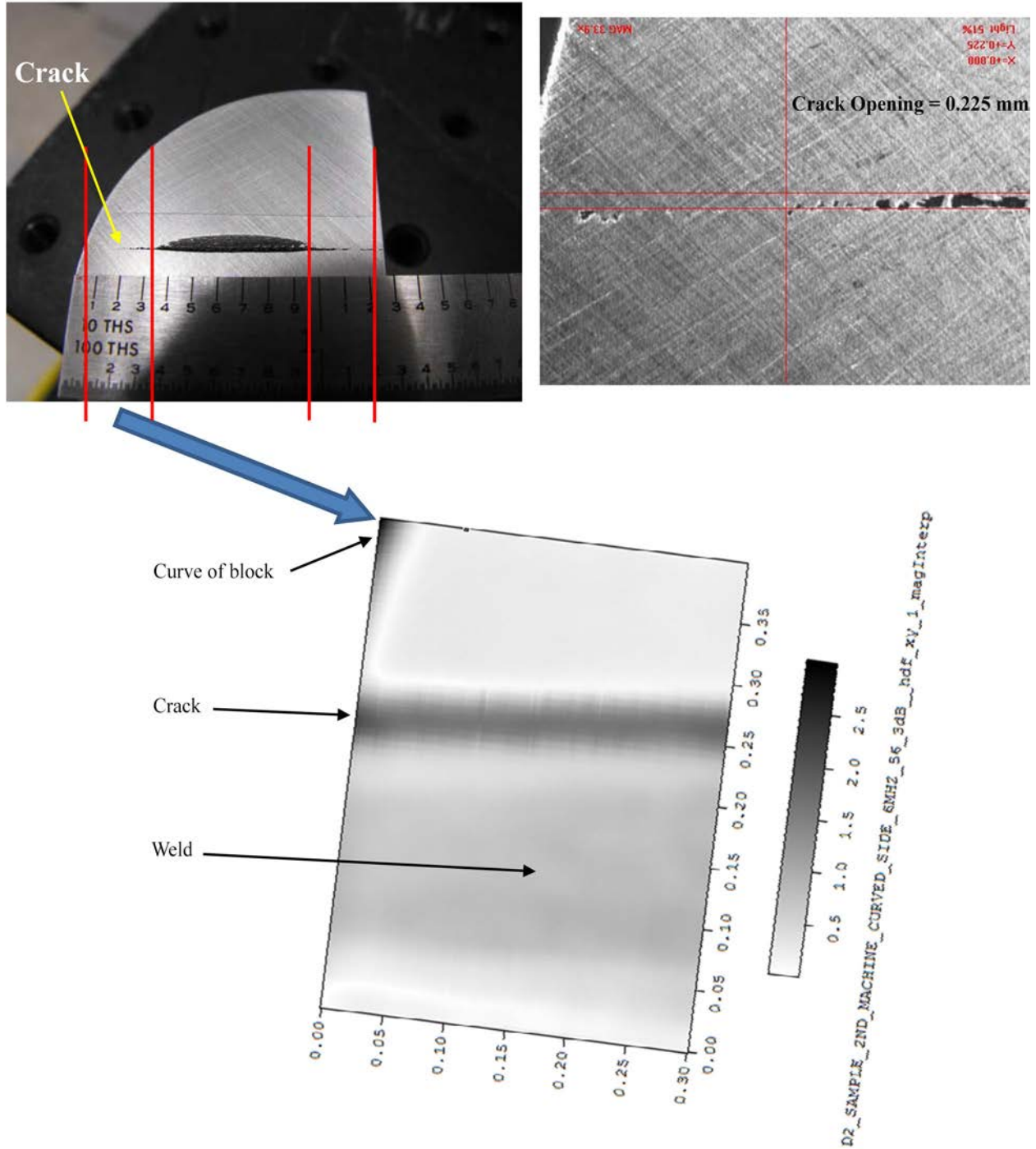


Figure A.16. Top Left Image is a Photograph of IGSCC Sample D2; the entire crack as machined to eliminate most of the weld geometry. Top Right Image is a Photograph of the Left Portion that was Eddy Current Scanned, which has a crack opening of 0.225 mm. Bottom is the Eddy Current Scan of the Left Portion of the Crack.

Appendix B: Results of Parametric Study of Probe Dimensions

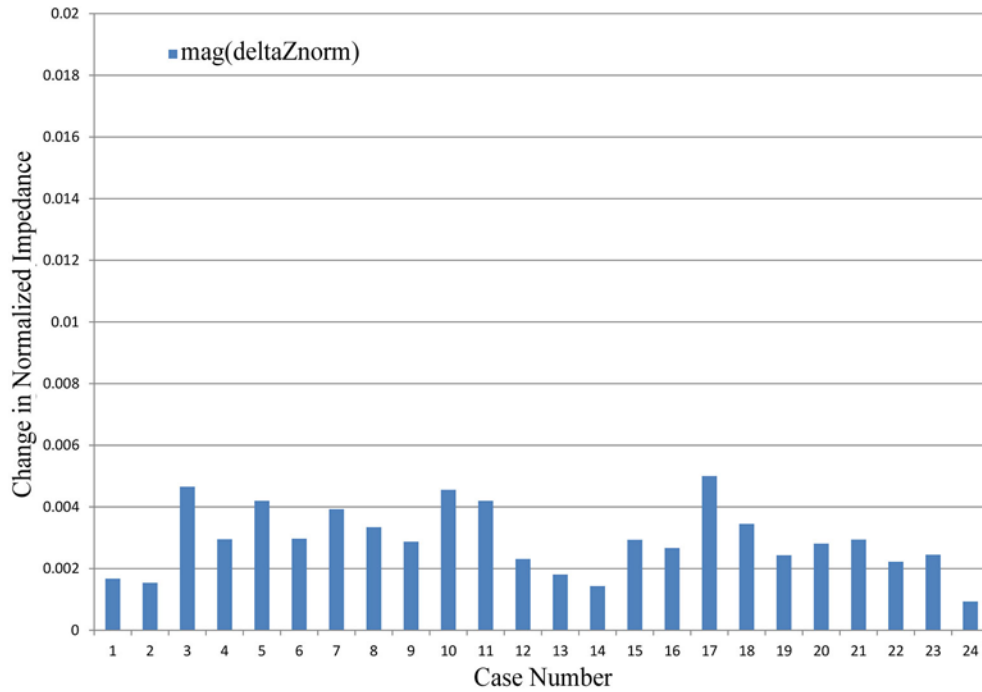


Figure B.1. Results of Parametric Analysis for 24 Variations of Probe Geometry Parameters for an Air-Core Probe over a Conductive Notch at 5 kHz. The vertical axis represents the change in normalized impedance magnitude between 8.4-mm deep and 4.2-mm deep rectangular notch models with constant aspect ratio of 3.

B.2

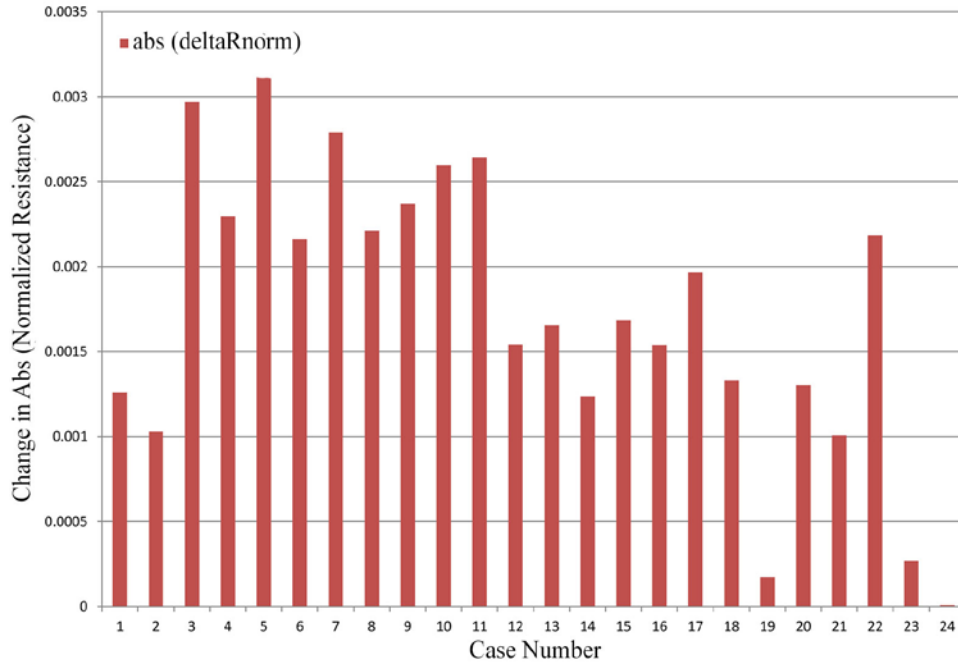


Figure B.2. Results of Parametric Analysis for 24 Variations of Probe Geometry Parameters for an Air-Core Probe over a Conductive Notch at 5 kHz. The vertical axis represents the change in normalized resistance between 8.4-mm deep and 4.2-mm deep rectangular notch models with constant aspect ratio of 3.

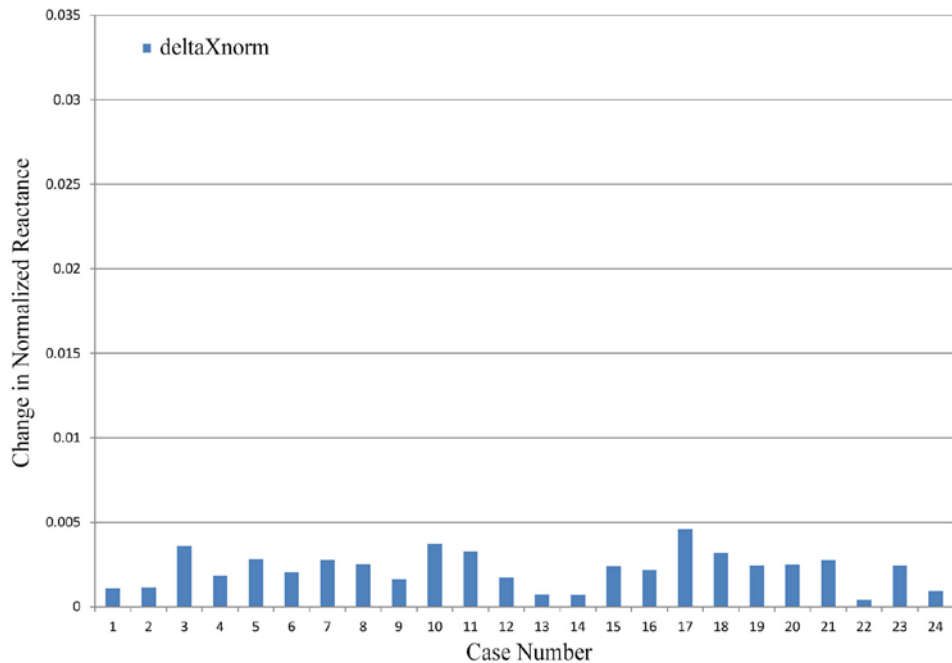


Figure B.3. Results of Parametric Analysis for 24 Variations of Probe Geometry Parameters for an Air-Core Probe over a Conductive Notch at 5 kHz. The vertical axis represents the change in normalized reactance between 8.4-mm deep and 4.2-mm deep rectangular notch models with constant aspect ratio of 3.

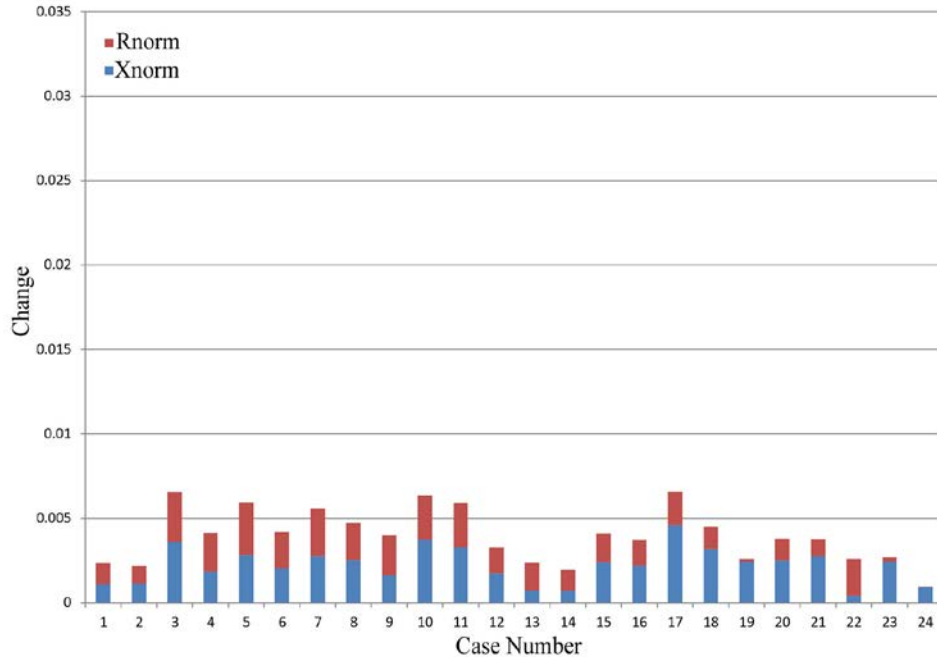


Figure B.4. Results of Parametric Analysis for 24 Variations of Probe Geometry Parameters for an Air-Core Probe over a Conductive Notch at 5 kHz. The change in normalized resistance and change in normalized reactance between 8.4-mm deep and 4.2-mm deep rectangular notch models with constant aspect ratio of 3 are represented on the vertical axis.

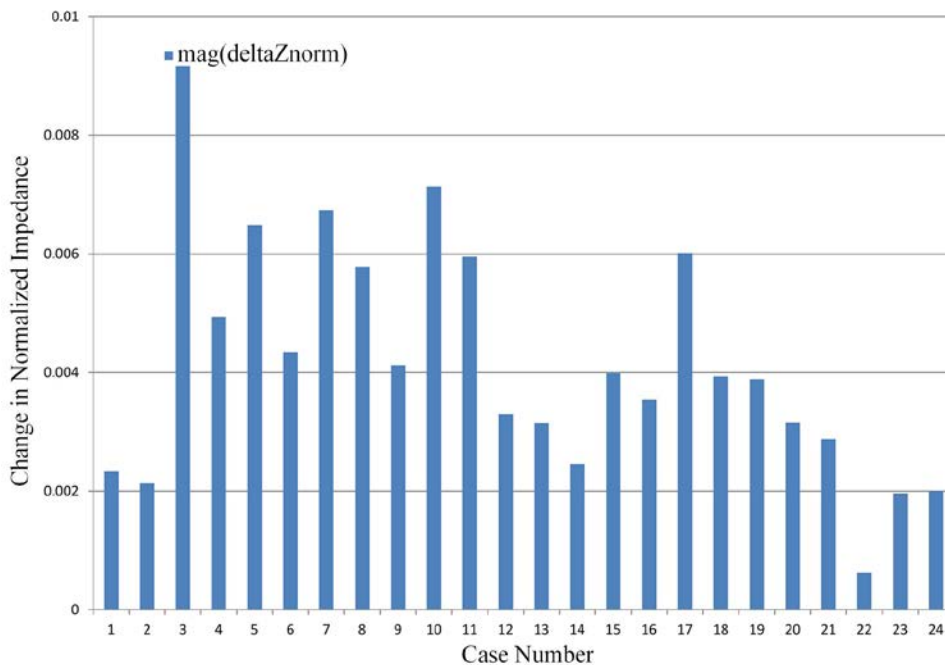


Figure B.5. Results of Parametric Analysis for 24 Variations of Probe Geometry Parameters for an Air-Core Probe over a Conductive Notch at 25 kHz. The vertical axis represents the change in normalized impedance magnitude between 8.4-mm deep and 4.2-mm deep rectangular notch models with constant aspect ratio of 3.

B.4

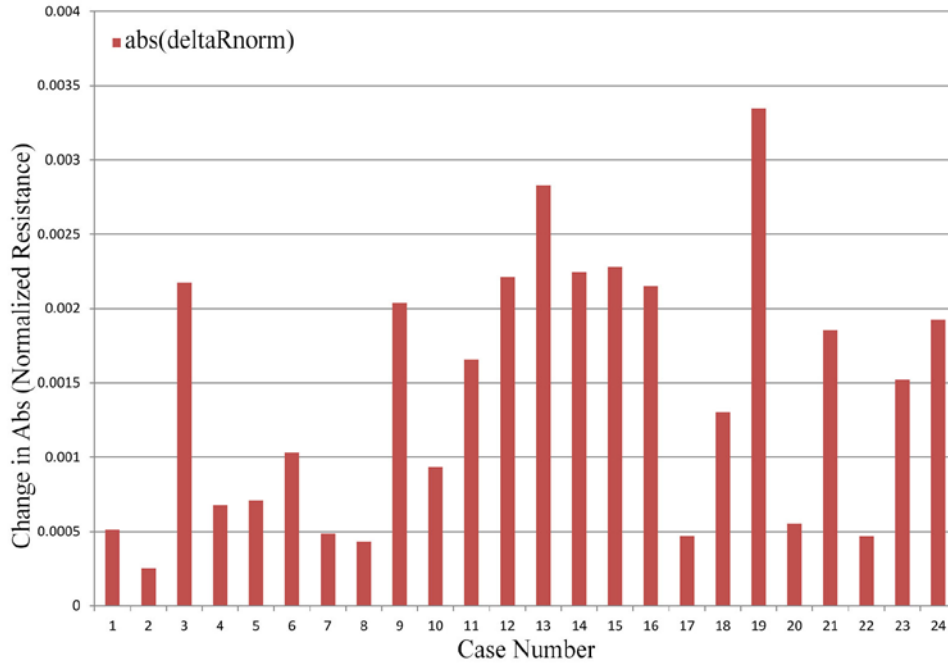


Figure B.6. Results of Parametric Analysis for 24 Variations of Probe Geometry Parameters for an Air-Core Probe over a Conductive Notch at 25 kHz. The vertical axis represents the change in normalized resistance between 8.4-mm deep and 4.2-mm deep rectangular notch models with constant aspect ratio of 3.

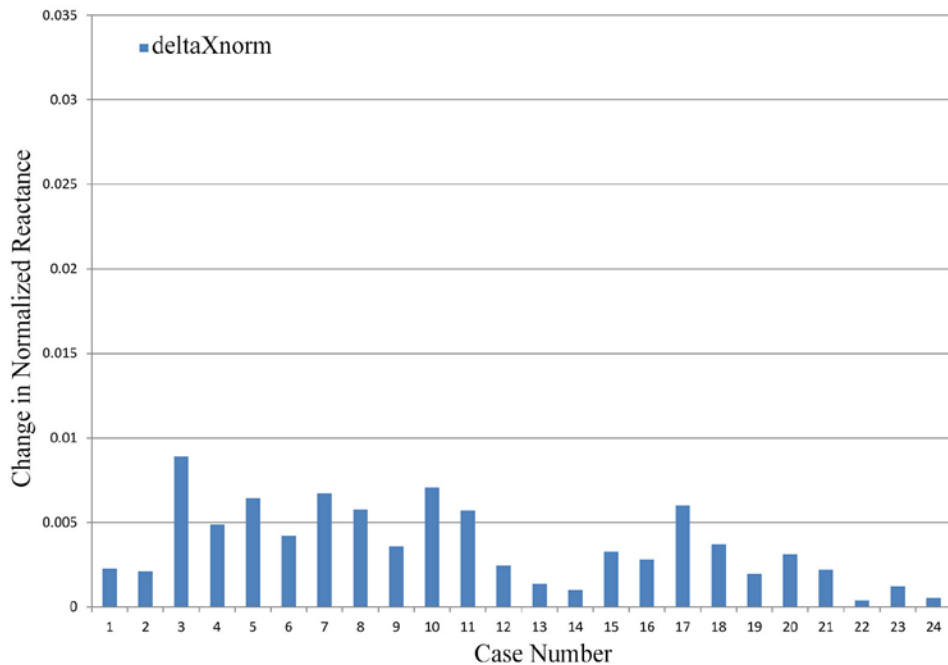


Figure B.7. Results of Parametric Analysis for 24 Variations of Probe Geometry Parameters for an Air-Core Probe over a Conductive Notch at 25 kHz. The vertical axis represents the change in normalized reactance between 8.4-mm deep and 4.2-mm deep rectangular notch models with constant aspect ratio of 3.

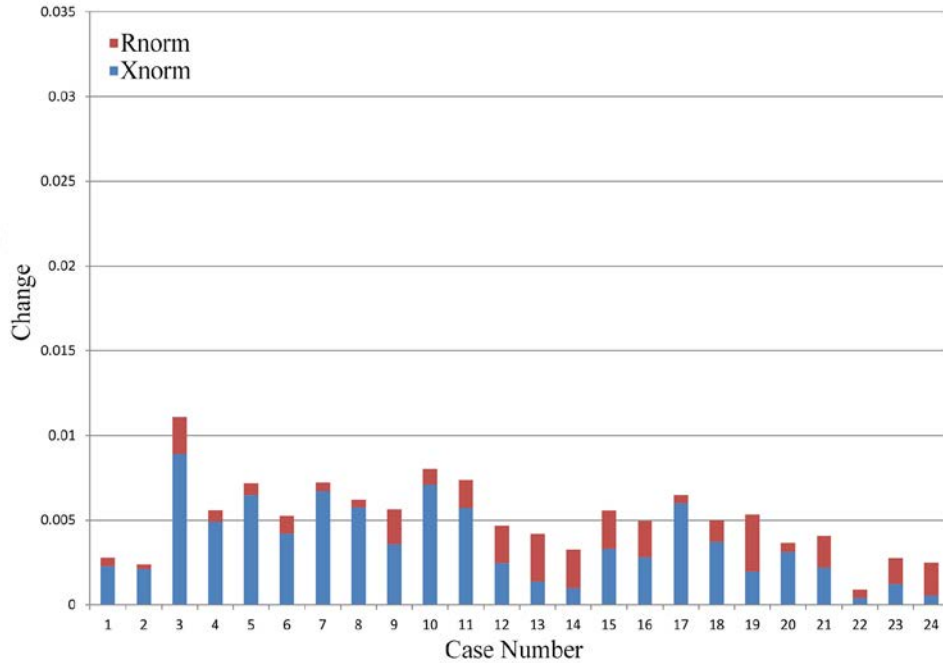


Figure B.8. Results of Parametric Analysis for 24 Variations of Probe Geometry Parameters for an Air-Core Probe over a Conductive Notch at 25 kHz. The change in normalized resistance and change in normalized reactance between 8.4-mm deep and 4.2-mm deep rectangular notch models with constant aspect ratio of 3 are represented on the vertical axis.

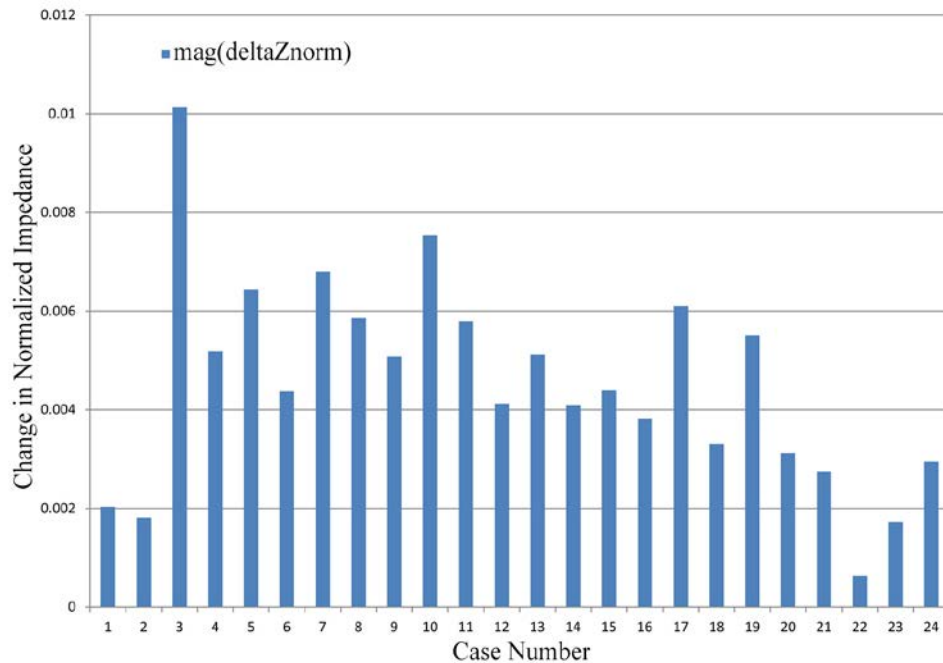


Figure B.9. Results of Parametric Analysis for 24 Variations of Probe Geometry Parameters for an Air-Core Probe over a Conductive Notch at 50 kHz. The vertical axis represents the change in normalized impedance magnitude between 8.4-mm deep and 4.2-mm deep rectangular notch models with constant aspect ratio of 3.

B.6

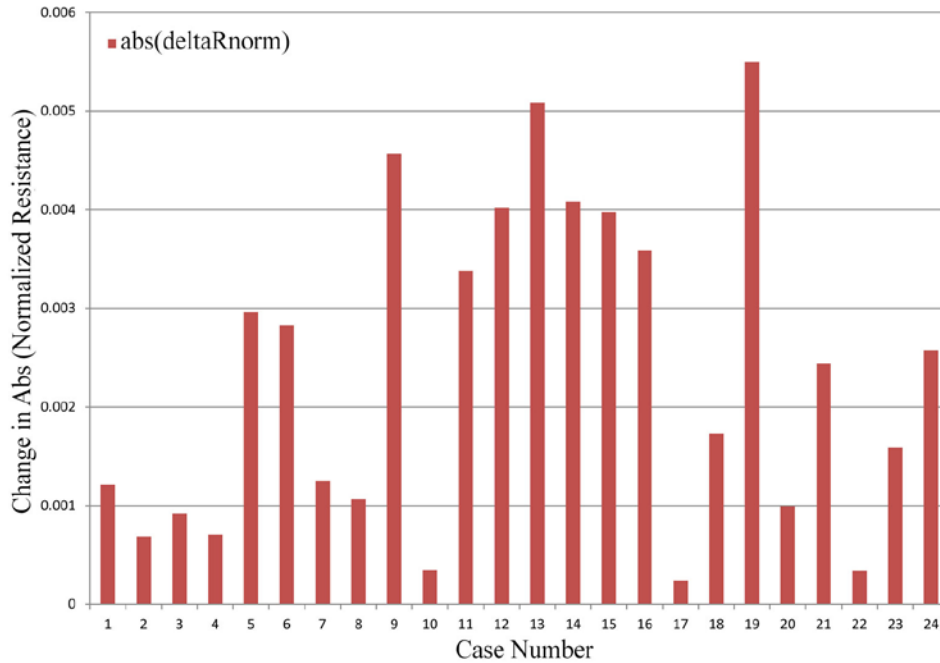


Figure B.10. Results of Parametric Analysis for 24 Variations of Probe Geometry Parameters for an Air-Core Probe over a Conductive Notch at 50 kHz. The vertical axis represents the change in normalized resistance between 8.4-mm deep and 4.2-mm deep rectangular notch models with constant aspect ratio of 3.

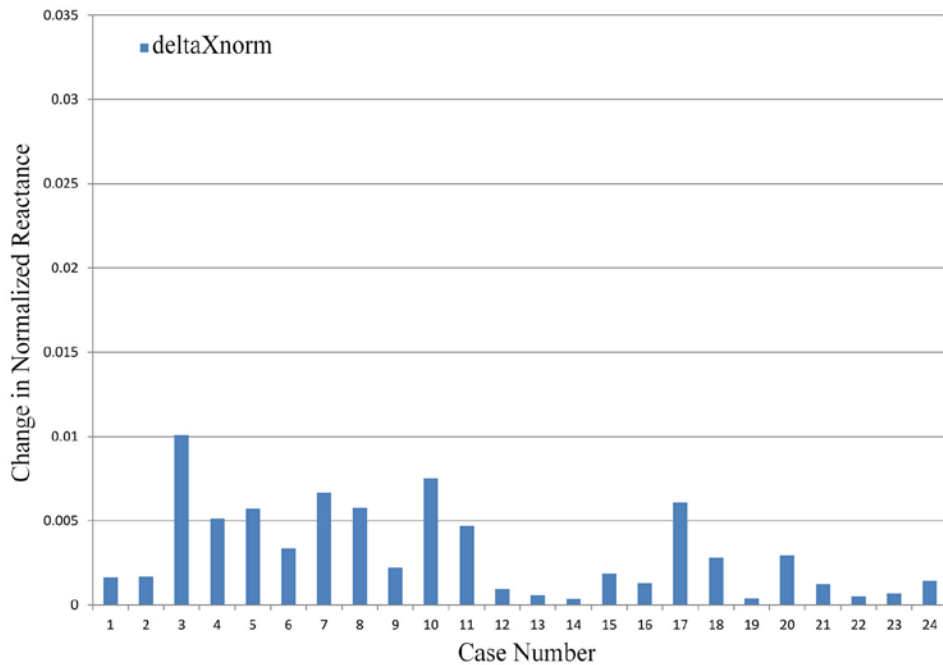


Figure B.11. Results of Parametric Analysis for 24 Variations of Probe Geometry Parameters for an Air-Core Probe over a Conductive Notch at 50 kHz. The vertical axis represents the change in normalized reactance between 8.4-mm deep and 4.2-mm deep rectangular notch models with constant aspect ratio of 3.

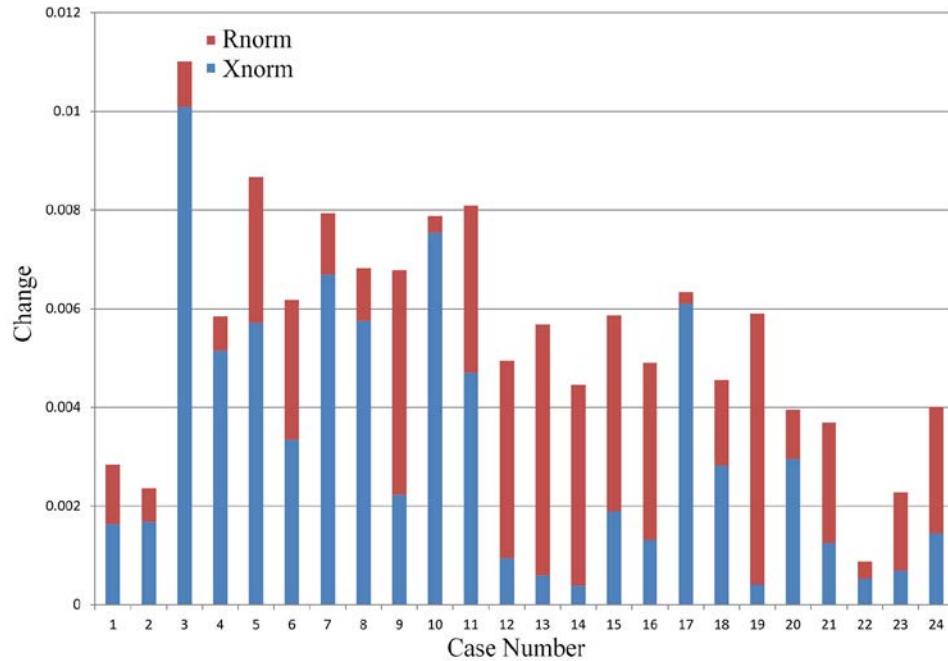


Figure B.12. Results of Parametric Analysis for 24 Variations of Probe Geometry Parameters for an Air-Core Probe over a Conductive Notch at 50 kHz. The change in normalized resistance and change in normalized reactance between 8.4-mm deep and 4.2-mm deep rectangular notch models with constant aspect ratio of 3 are represented on the vertical axis.

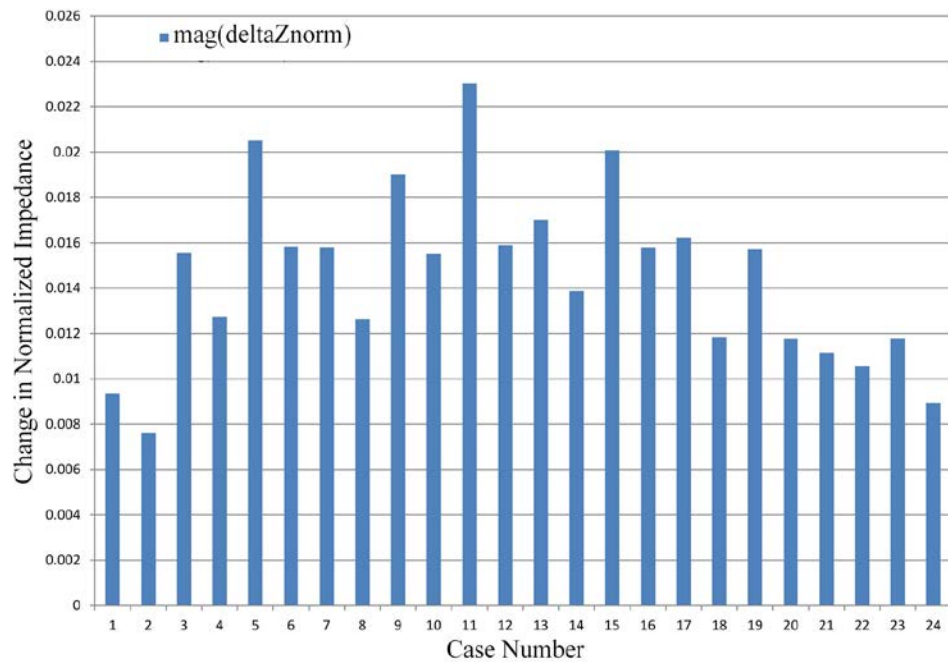


Figure B.13. Results of Parametric Analysis for 24 Variations of Probe Geometry Parameters for an Air-Core Probe over an Air-Filled Notch at 5 kHz. The vertical axis represents the change in normalized impedance magnitude between 8.4-mm deep and 4.2-mm deep rectangular notch models with constant aspect ratio of 3.

B.8

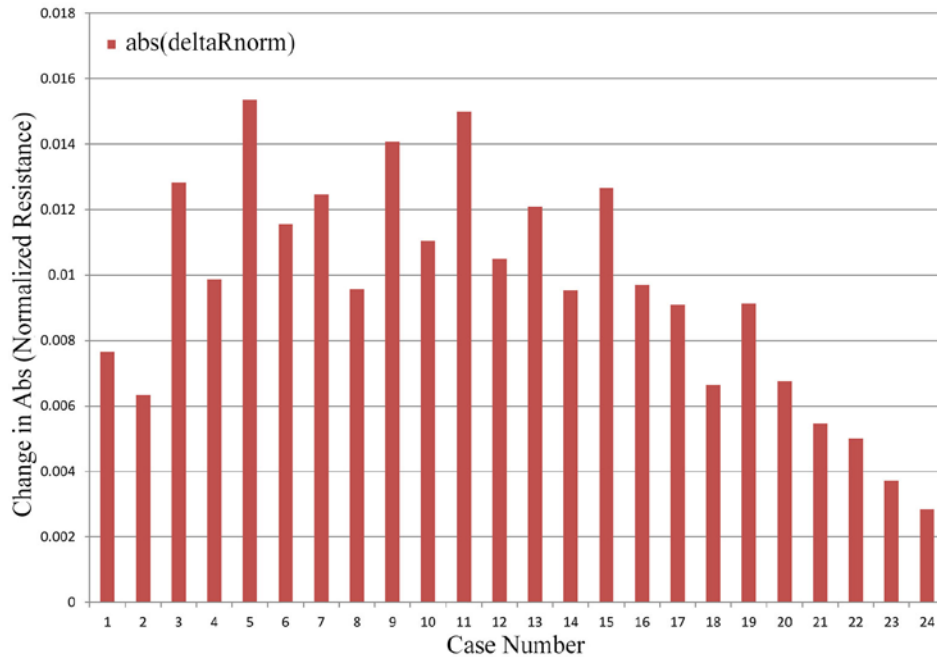


Figure B.14. Results of Parametric Analysis for 24 Variations of Probe Geometry Parameters for an Air-Core Probe over an Air-Filled Notch at 5 kHz. The vertical axis represents the change in normalized resistance between 8.4-mm deep and 4.2-mm deep rectangular notch models with constant aspect ratio of 3.

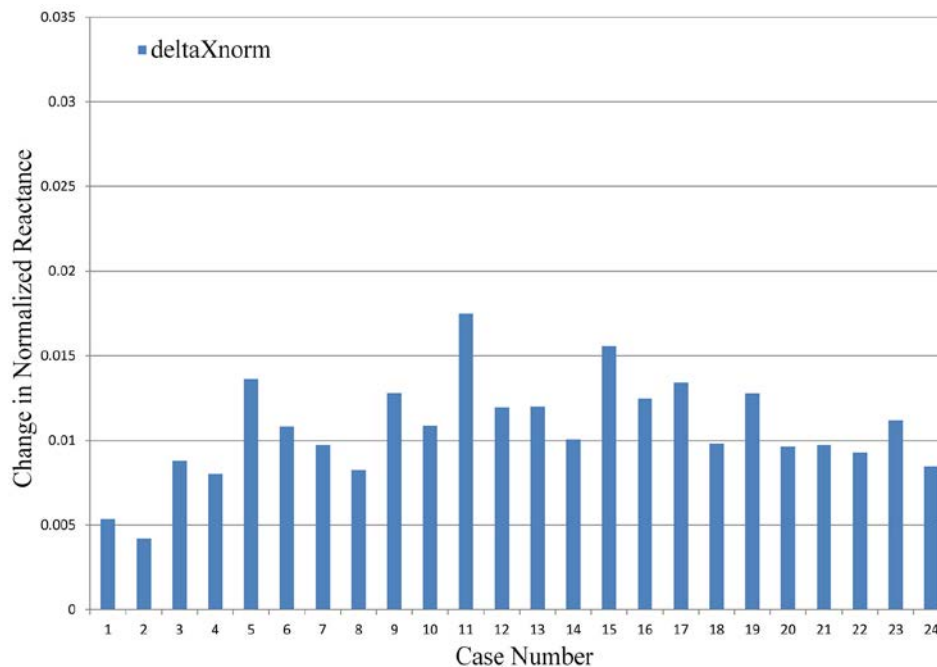


Figure B.15. Results of Parametric Analysis for 24 Variations of Probe Geometry Parameters for an Air-Core Probe over an Air-Filled Notch at 5 kHz. The vertical axis represents the change in normalized reactance between 8.4-mm deep and 4.2-mm deep rectangular notch models with constant aspect ratio of 3.

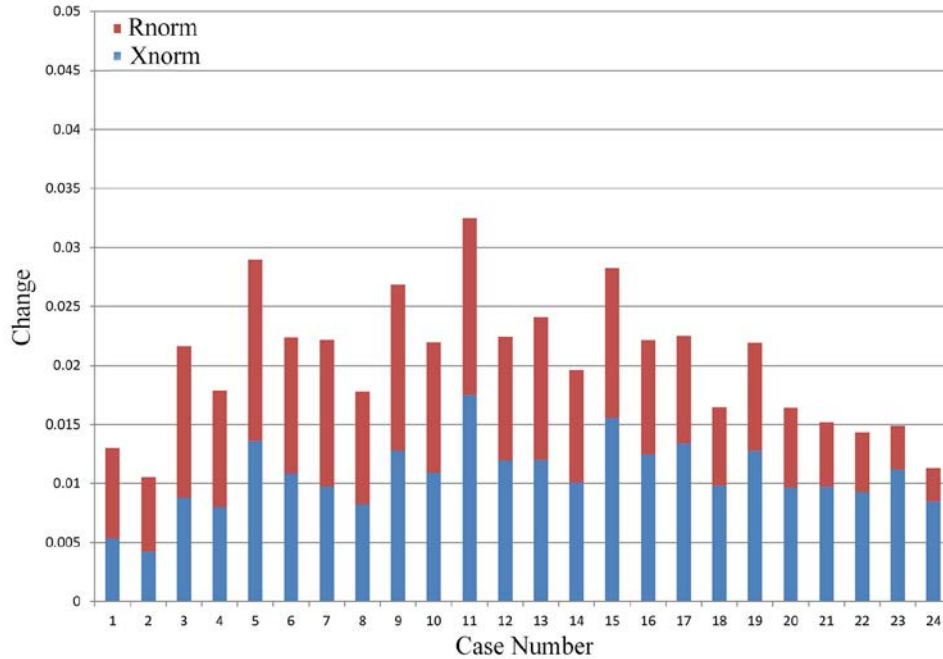


Figure B.16. Results of Parametric Analysis for 24 Variations of Probe Geometry Parameters for an Air-Core Probe over an Air-Filled Notch at 5 kHz. The change in normalized resistance and change in normalized reactance between 8.4-mm deep and 4.2-mm deep rectangular notch models with constant aspect ratio of 3 are represented on the vertical axis.

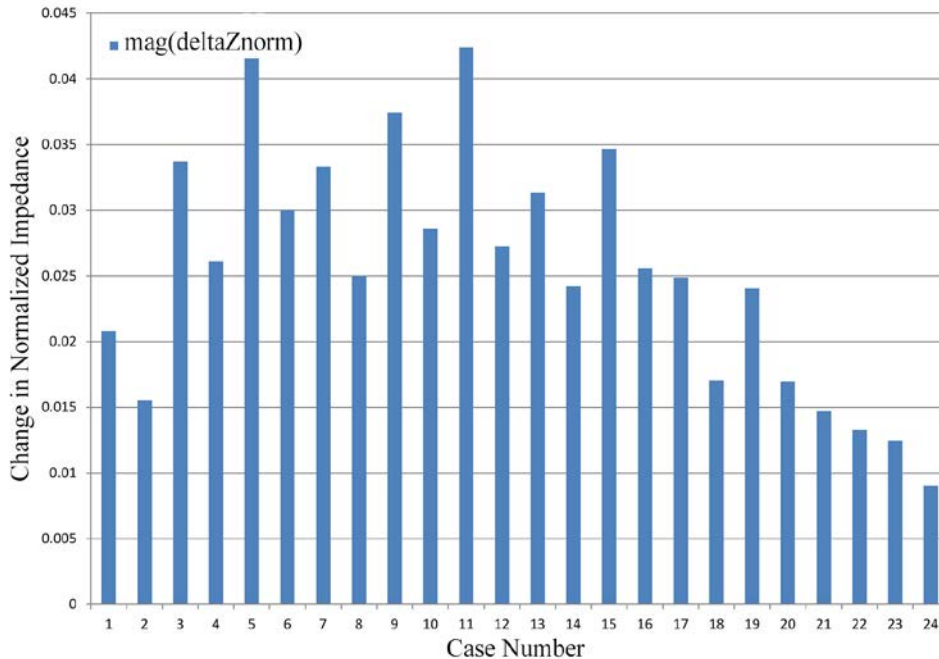


Figure B.17. Results of Parametric Analysis for 24 Variations of Probe Geometry Parameters for an Air-Core Probe over an Air-Filled Notch at 25 kHz. The vertical axis represents the change in normalized impedance magnitude between 8.4-mm deep and 4.2-mm deep rectangular notch models with constant aspect ratio of 3.

B.10

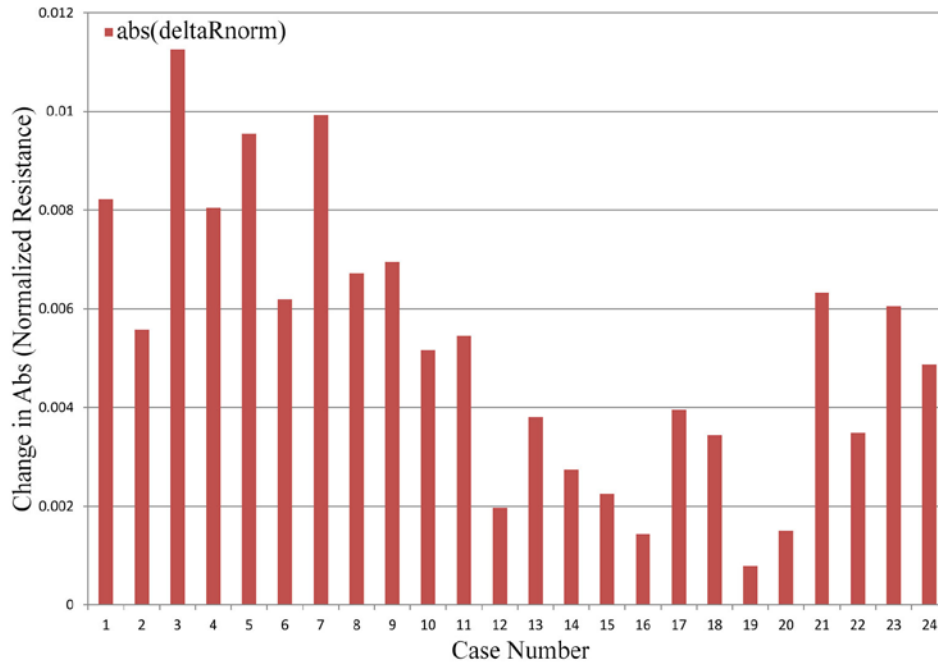


Figure B.18. Results of Parametric Analysis for 24 Variations of Probe Geometry Parameters for an Air-Core Probe over an Air-Filled Notch at 25 kHz. The vertical axis represents the change in normalized resistance between 8.4-mm deep and 4.2-mm deep rectangular notch models with constant aspect ratio of 3.

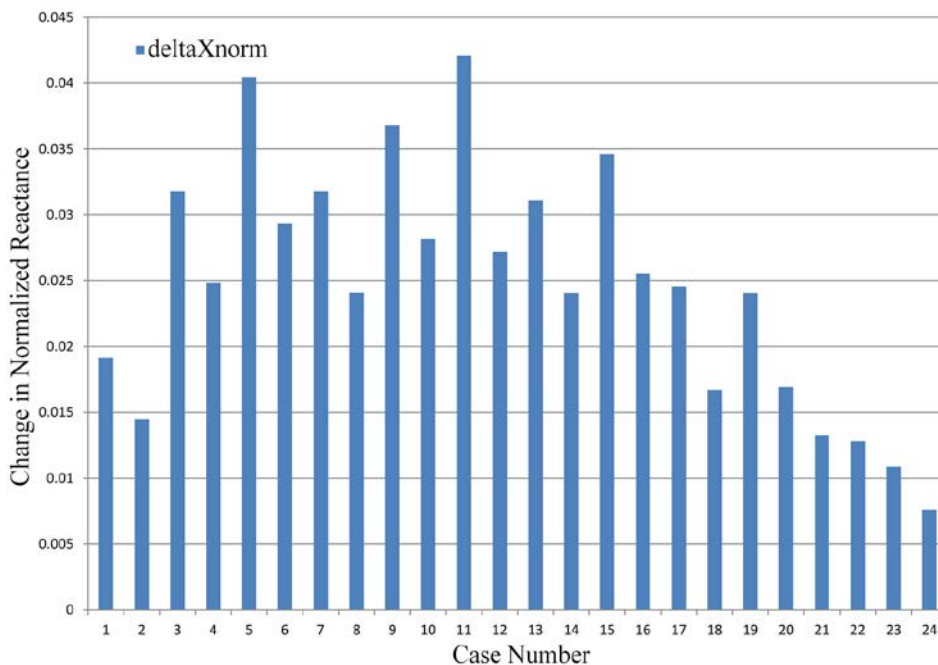


Figure B.19. Results of Parametric Analysis for 24 Variations of Probe Geometry Parameters for an Air-Core Probe over an Air-Filled Notch at 25 kHz. The vertical axis represents the change in normalized reactance between 8.4-mm deep and 4.2-mm deep rectangular notch models with constant aspect ratio of 3.

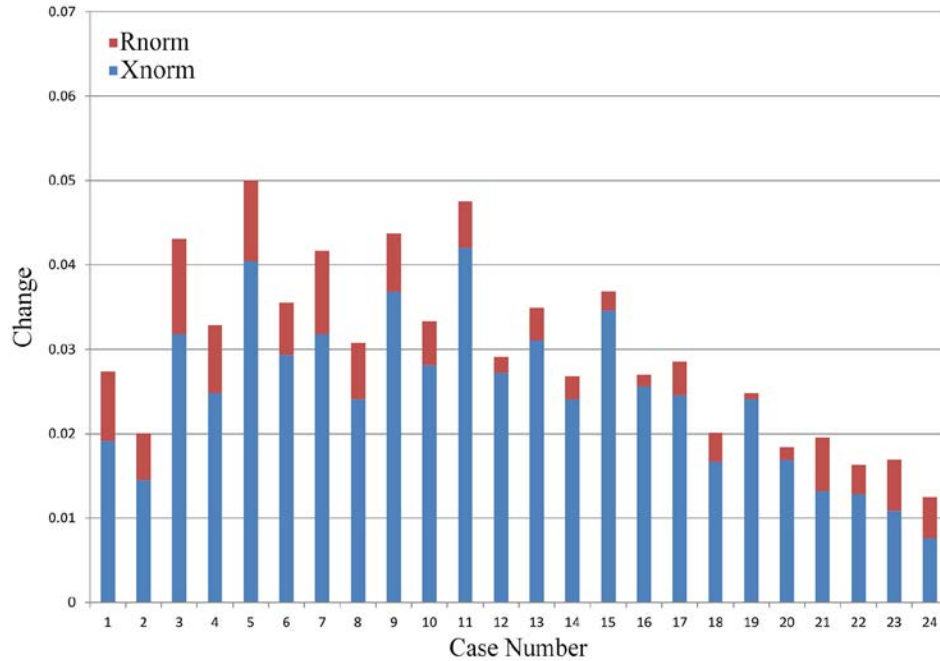


Figure B.20. Results of Parametric Analysis for 24 Variations of Probe Geometry Parameters for an Air-Core Probe over an Air-Filled Notch at 25 kHz. The change in normalized resistance and change in normalized reactance between 8.4-mm deep and 4.2-mm deep rectangular notch models with constant aspect ratio of 3 are represented on the vertical axis.

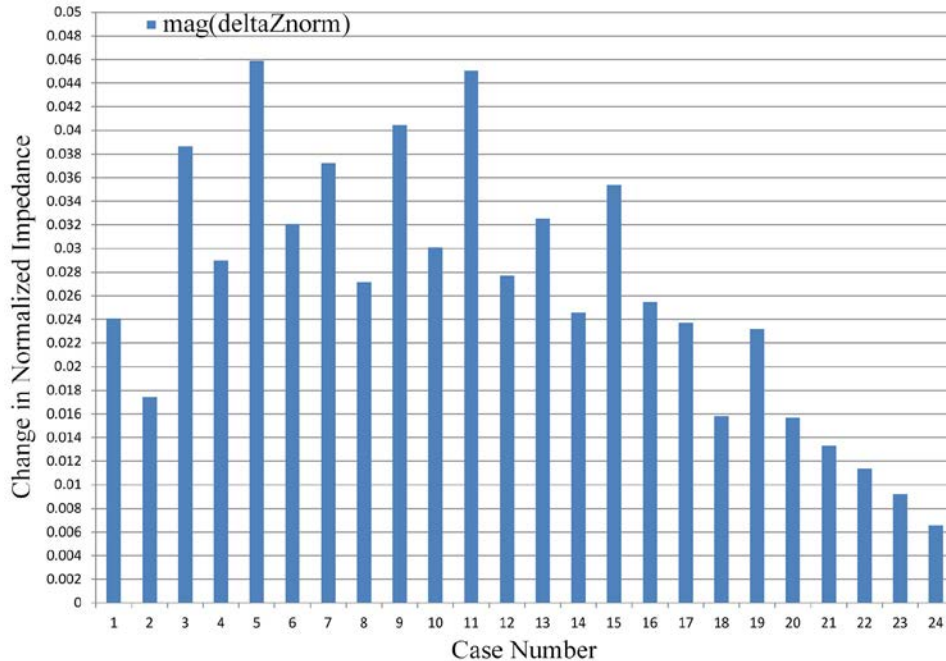


Figure B.21. Results of Parametric Analysis for 24 Variations of Probe Geometry Parameters for an Air-Core Probe over an Air-Filled Notch at 50 kHz. The vertical axis represents the change in normalized impedance magnitude between 8.4-mm deep and 4.2-mm deep rectangular notch models with constant aspect ratio of 3.

B.12

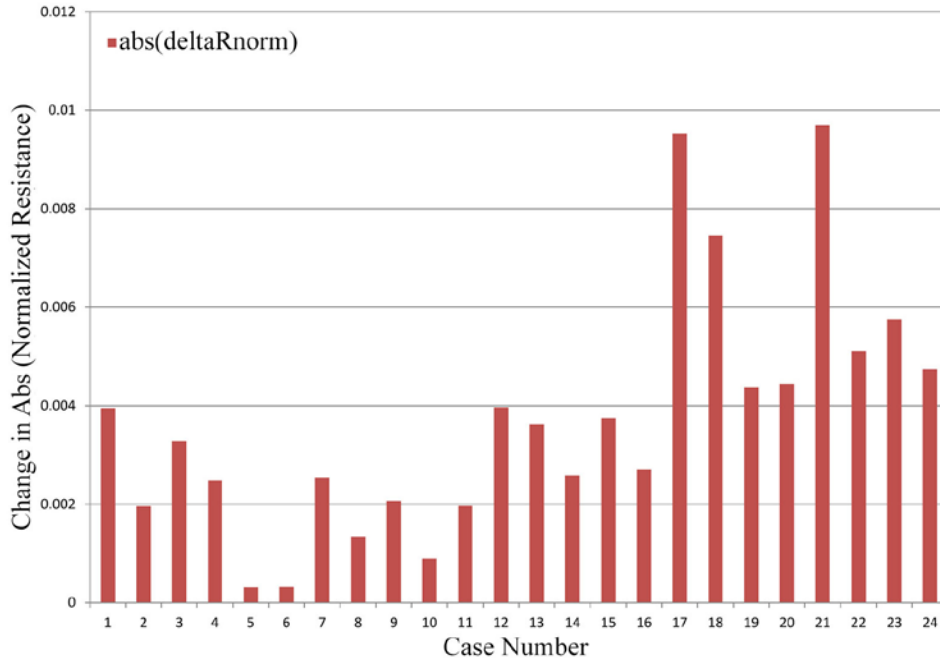


Figure B.22. Results of Parametric Analysis for 24 Variations of Probe Geometry Parameters for an Air-Core Probe over an Air-Filled Notch at 50 kHz. The vertical axis represents the change in normalized resistance between 8.4-mm deep and 4.2-mm deep rectangular notch models with constant aspect ratio of 3.

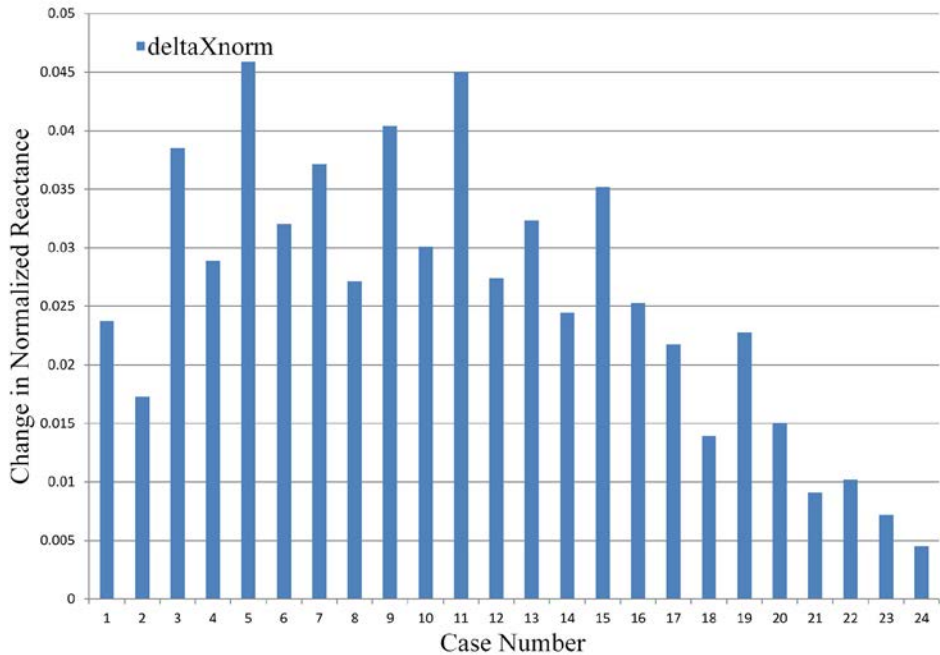


Figure B.23. Results of Parametric Analysis for 24 Variations of Probe Geometry Parameters for an Air-Core Probe over an Air-Filled Notch at 50 kHz. The vertical axis represents the change in normalized reactance between 8.4-mm deep and 4.2-mm deep rectangular notch models with constant aspect ratio of 3.

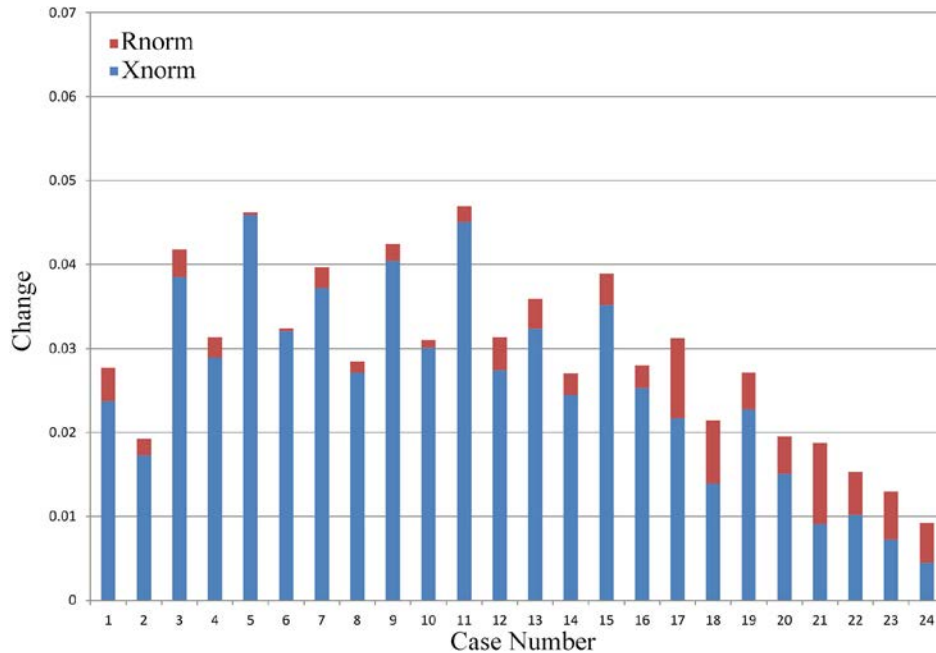


Figure B.24. Results of Parametric Analysis for 24 Variations of Probe Geometry Parameters for an Air-Core Probe over an Air-Filled Notch at 50 kHz. The change in normalized resistance and change in normalized reactance between 8.4-mm deep and 4.2-mm deep rectangular notch models with constant aspect ratio of 3 are represented on the vertical axis.

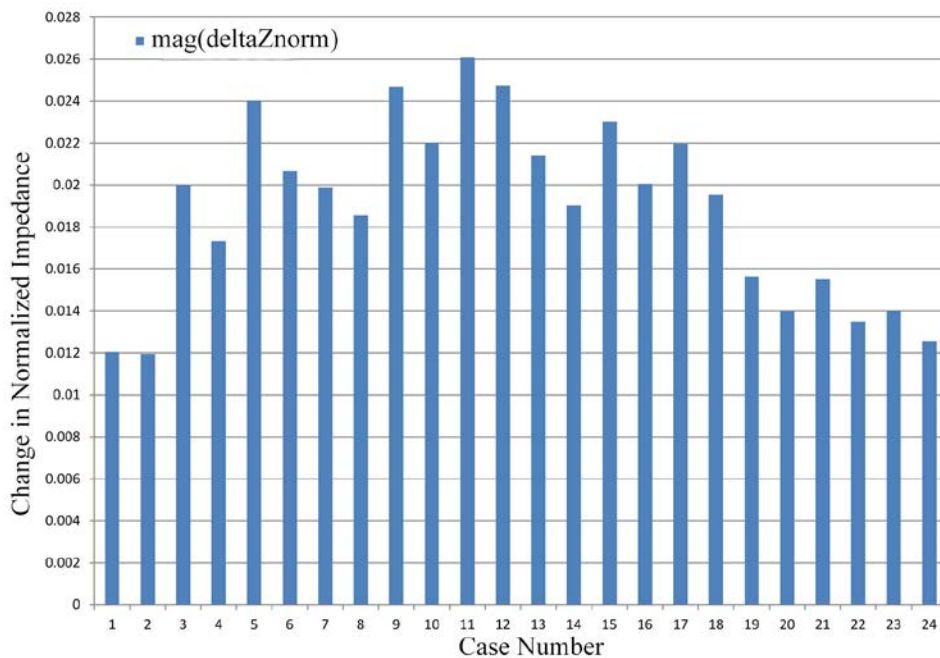


Figure B.25. Results of Parametric Analysis for 24 Variations of Probe Geometry Parameters for a Ferrite-Core Probe over an Air-Filled Notch at 5 kHz. The vertical axis represents the change in normalized impedance magnitude between 8.4-mm deep and 4.2-mm deep rectangular notch models with constant aspect ratio of 3.

B.14

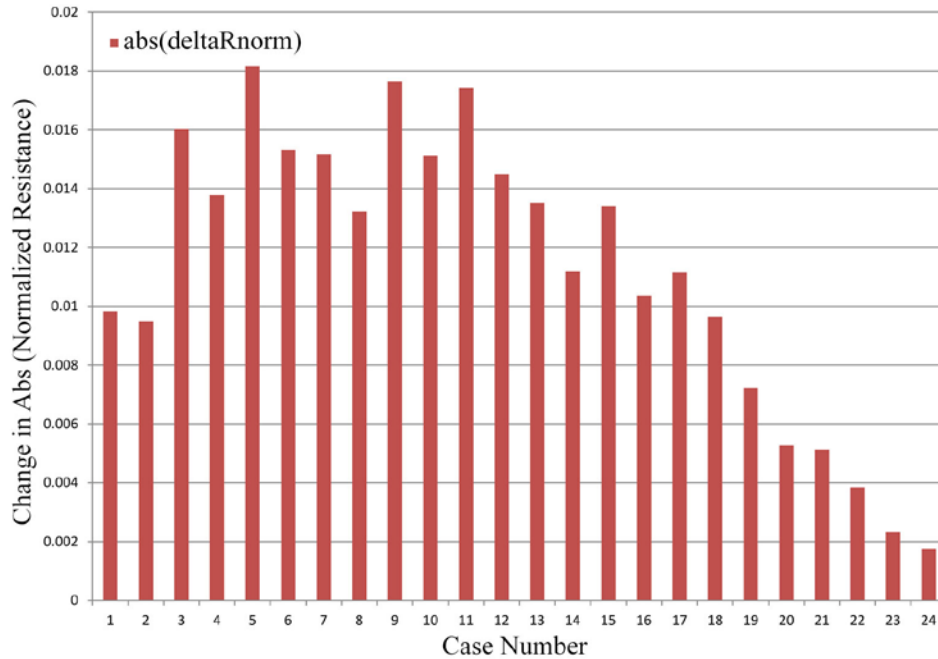


Figure B.26. Results of Parametric Analysis for 24 Variations of Probe Geometry Parameters for a Ferrite-Core Probe over an Air-Filled Notch at 5 kHz. The vertical axis represents the change in normalized resistance between 8.4-mm deep and 4.2-mm deep rectangular notch models with constant aspect ratio of 3.

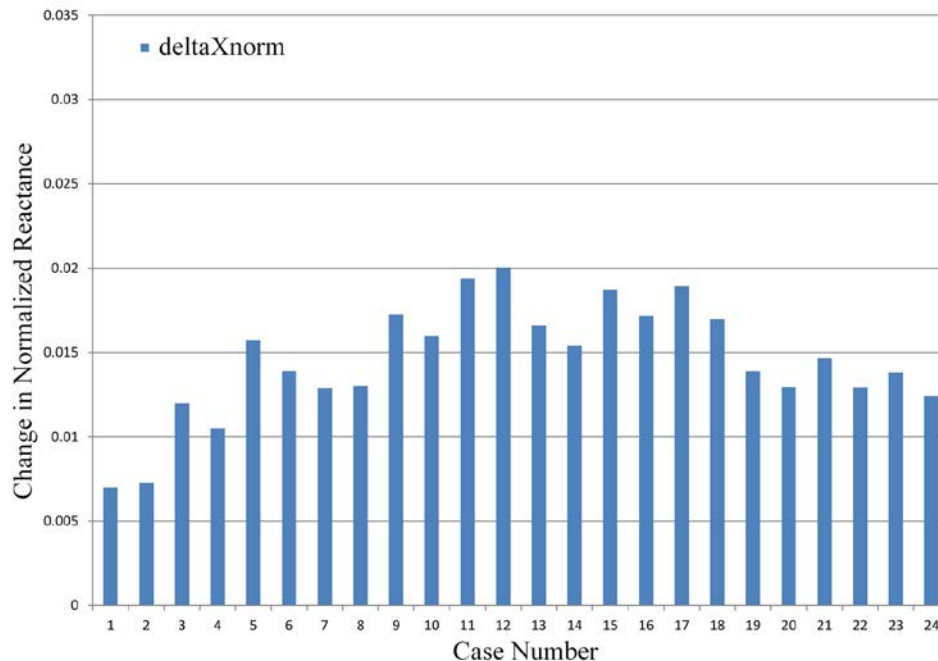


Figure B.27. Results of Parametric Analysis for 24 Variations of Probe Geometry Parameters for a Ferrite-Core Probe over an Air-Filled Notch at 5 kHz. The vertical axis represents the change in normalized reactance between 8.4-mm deep and 4.2-mm deep rectangular notch models with constant aspect ratio of 3.

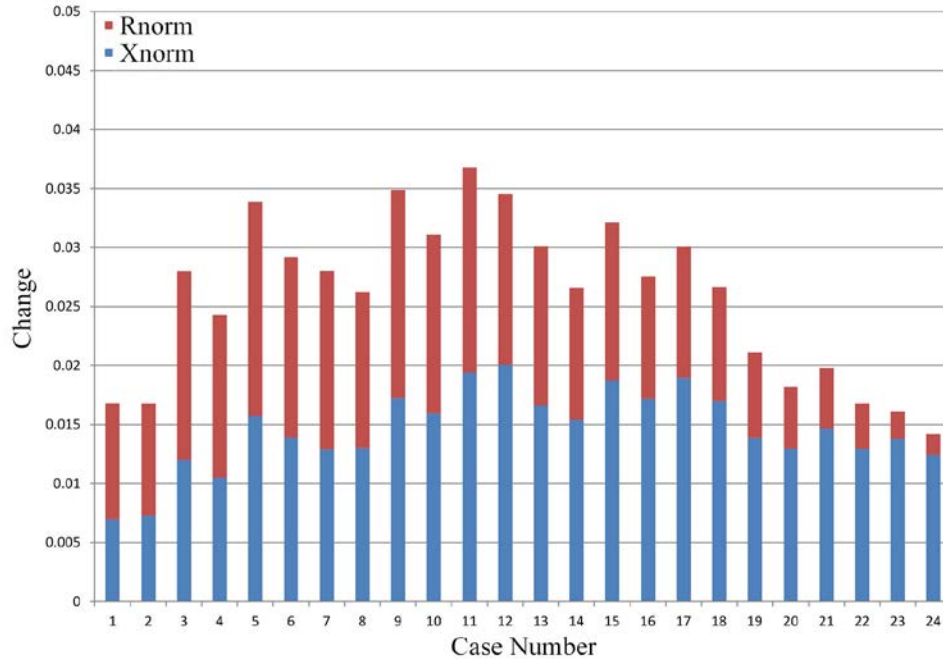


Figure B.28. Results of Parametric Analysis for 24 Variations of Probe Geometry Parameters for a Ferrite-Core Probe over an Air-Filled Notch at 5 kHz. The change in normalized resistance and change in normalized reactance between 8.4-mm deep and 4.2-mm deep rectangular notch models with constant aspect ratio of 3 are represented on the vertical axis.

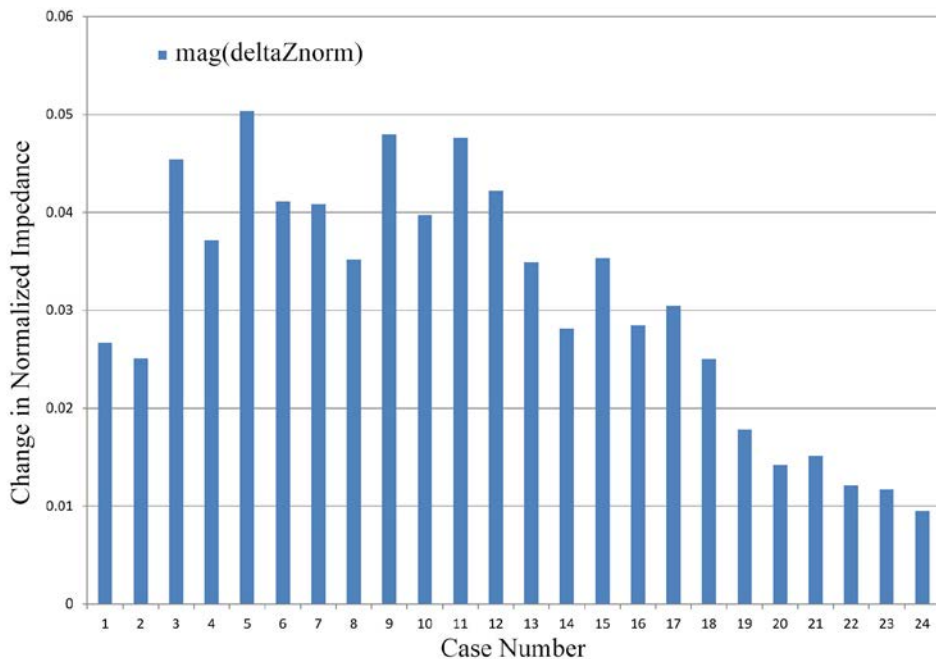


Figure B.29. Results of Parametric Analysis for 24 Variations of Probe Geometry Parameters for a Ferrite-Core Probe over an Air-Filled Notch at 25 kHz. The vertical axis represents the change in normalized impedance magnitude between 8.4-mm deep and 4.2-mm deep rectangular notch models with constant aspect ratio of 3.

B.16

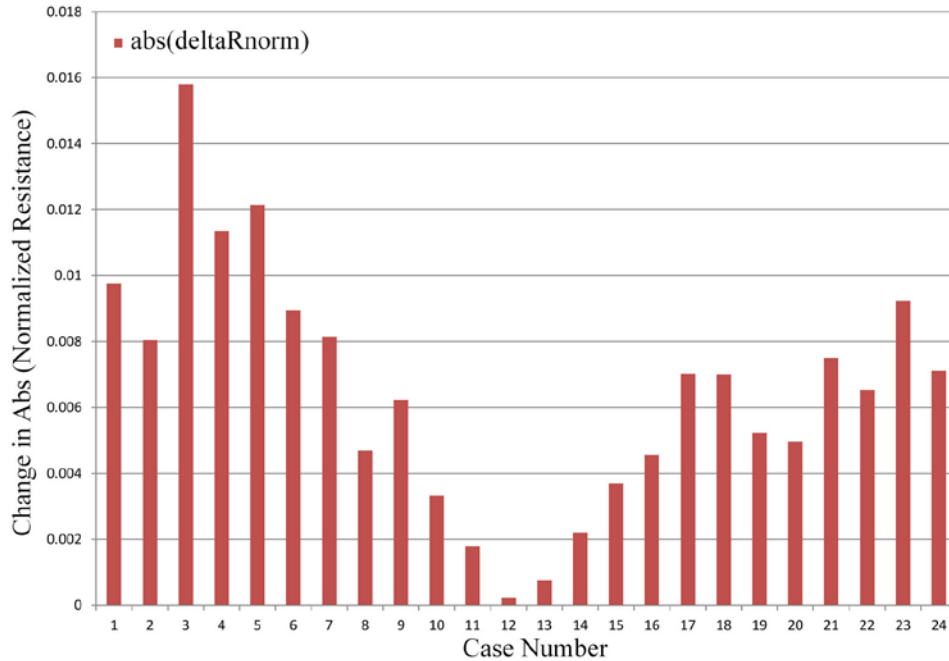


Figure B.30. Results of Parametric Analysis for 24 Variations of Probe Geometry Parameters for a Ferrite-Core Probe over an Air-Filled Notch at 25 kHz. The vertical axis represents the change in normalized resistance between 8.4-mm deep and 4.2-mm deep rectangular notch models with constant aspect ratio of 3.

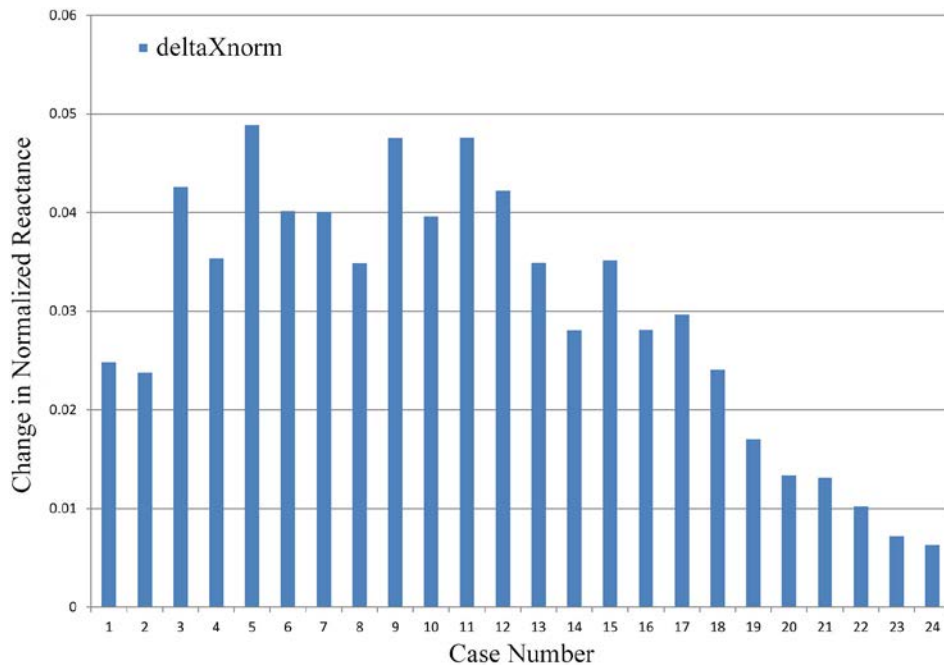


Figure B.31. Results of Parametric Analysis for 24 Variations of Probe Geometry Parameters for a Ferrite-Core Probe over an Air-Filled Notch at 25 kHz. The vertical axis represents the change in normalized reactance between 8.4-mm deep and 4.2-mm deep rectangular notch models with constant aspect ratio of 3.

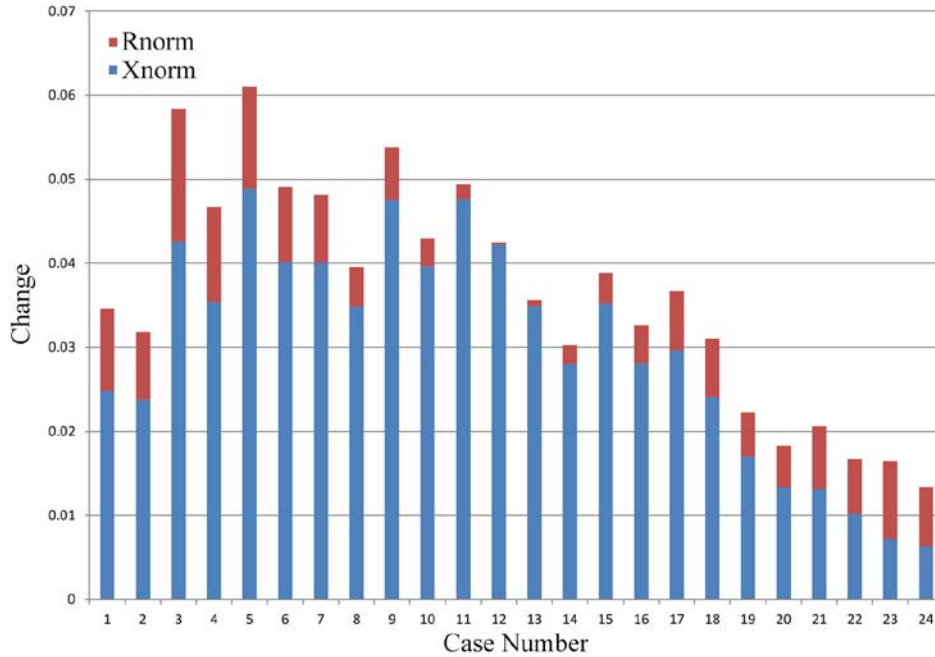


Figure B.32. Results of Parametric Analysis for 24 Variations of Probe Geometry Parameters for a Ferrite-Core Probe over an Air-Filled Notch at 25 kHz. The change in normalized resistance and change in normalized reactance between 8.4-mm deep and 4.2-mm deep rectangular notch models with constant aspect ratio of 3 are represented on the vertical axis.

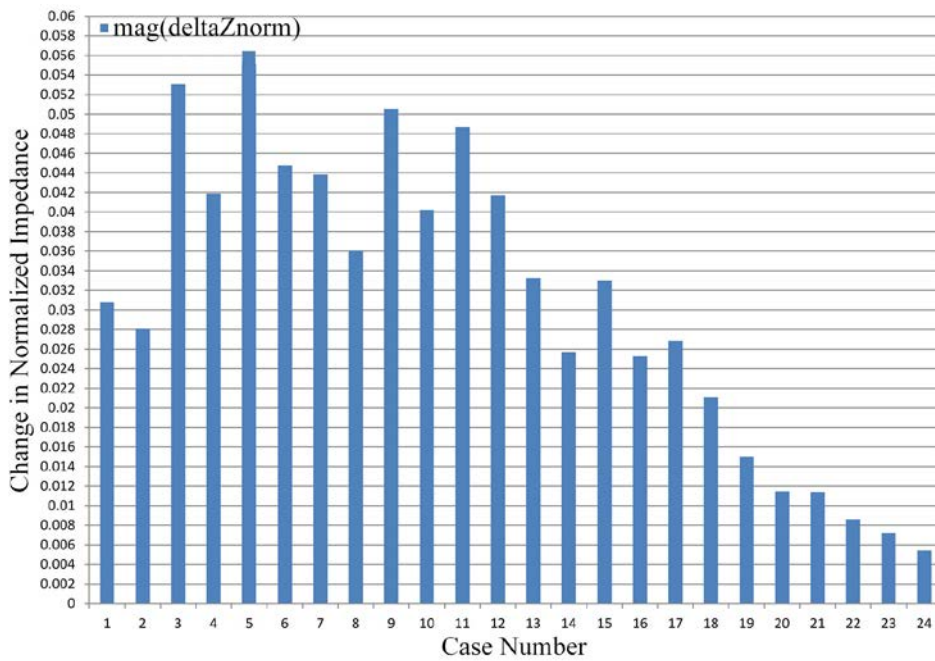


Figure B.33. Results of Parametric Analysis for 24 Variations of Probe Geometry Parameters for a Ferrite-Core Probe over an Air-Filled Notch at 50 kHz. The vertical axis represents the change in normalized impedance magnitude between 8.4-mm deep and 4.2-mm deep rectangular notch models with constant aspect ratio of 3.

B.18

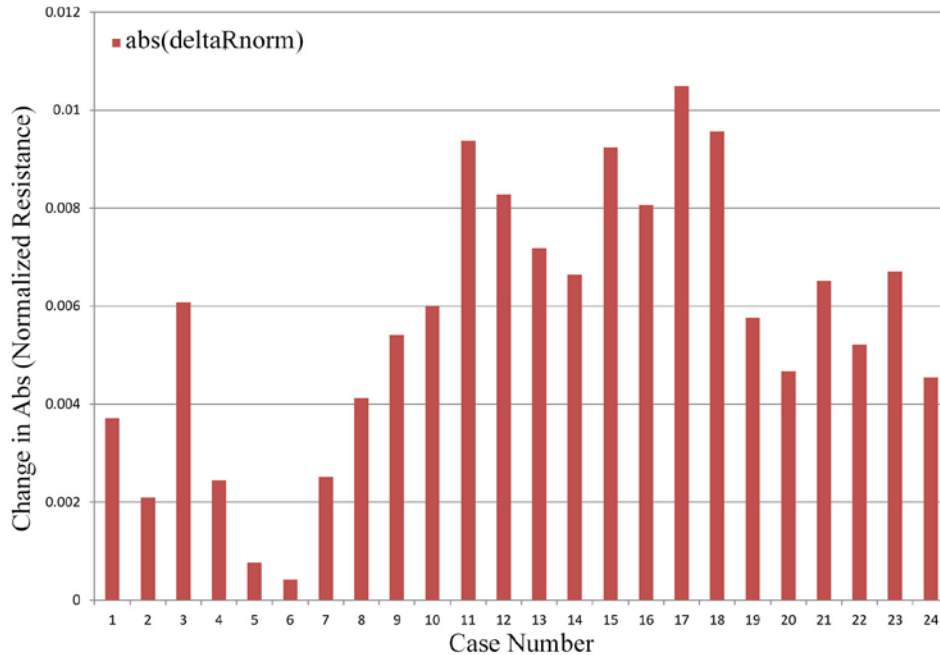


Figure B.34. Results of Parametric Analysis for 24 Variations of Probe Geometry Parameters for a Ferrite-Core Probe over an Air-Filled Notch at 50 kHz. The vertical axis represents the change in normalized resistance between 8.4-mm deep and 4.2-mm deep rectangular notch models with constant aspect ratio of 3.

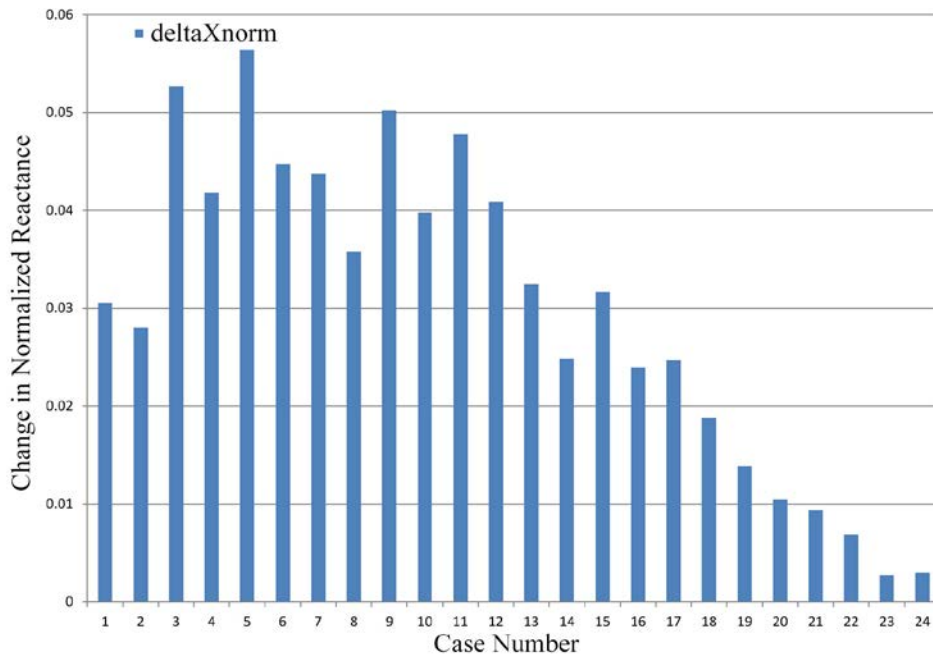


Figure B.35. Results of Parametric Analysis for 24 Variations of Probe Geometry Parameters for a Ferrite-Core Probe over an Air-Filled Notch at 50 kHz. The vertical axis represents the change in normalized reactance between 8.4-mm deep and 4.2-mm deep rectangular notch models with constant aspect ratio of 3.

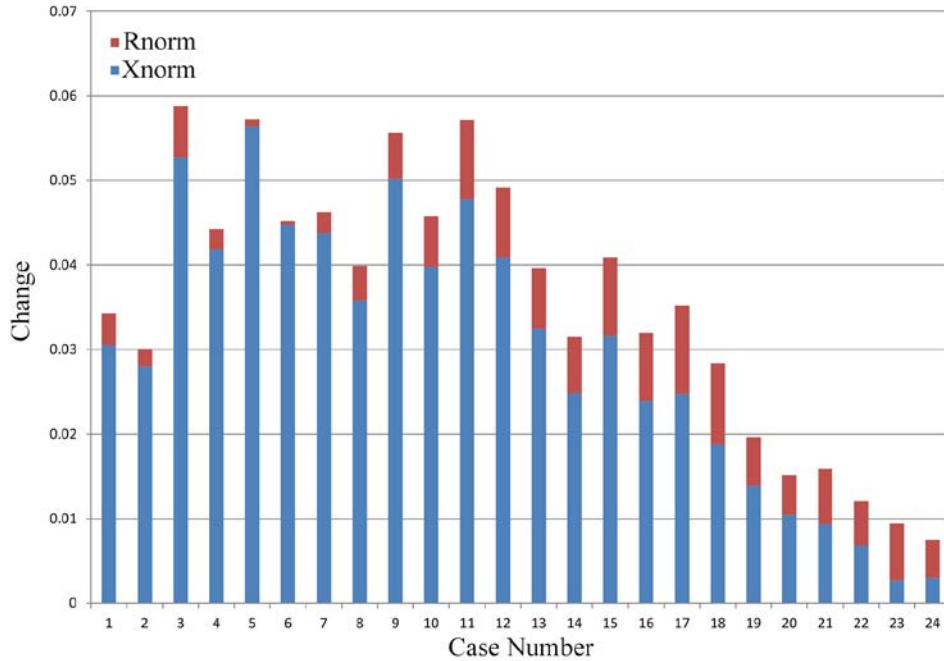


Figure B.36. Results of Parametric Analysis for 24 Variations of Probe Geometry Parameters for a Ferrite-Core Probe over an Air-Filled Notch at 50 kHz. The change in normalized resistance and change in normalized reactance between 8.4-mm deep and 4.2-mm deep rectangular notch models with constant aspect ratio of 3 are represented on the vertical axis.

Appendix C: Simulated Eddy Current Frequency Sweep Responses

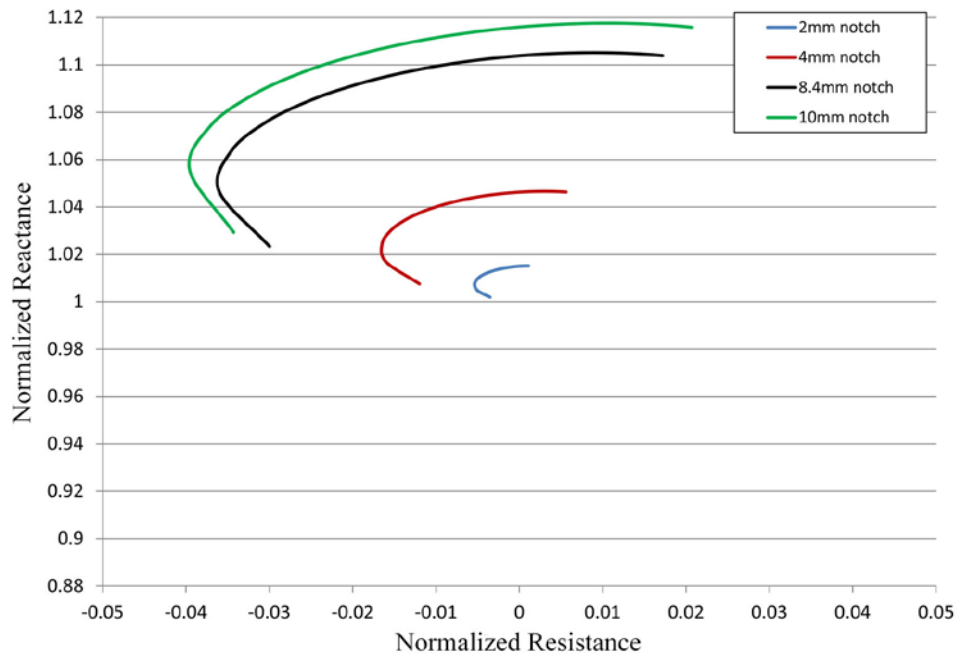
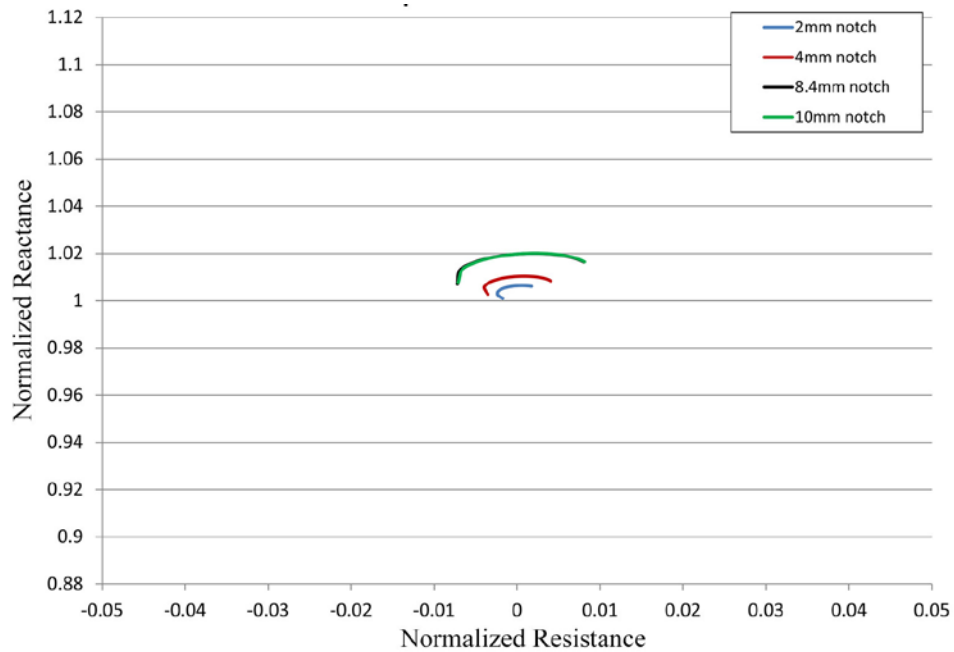


Figure C.1. Impedance Plane Response for Ferrite-Core Probe Over Air-Filled Rectangular Notches (0% Conductivity) with 3:1 Aspect Ratio and 150 μm Width Over Frequency Range from 5 kHz to 100 kHz in Clockwise Direction



C.2

Figure C.2. Impedance Plane Response for Ferrite-Core Probe Over Conductive Rectangular Notches (5% Conductivity) with 3:1 Aspect Ratio and 150 μm Width Over Frequency Range from 5 kHz to 100 kHz in Clockwise Direction

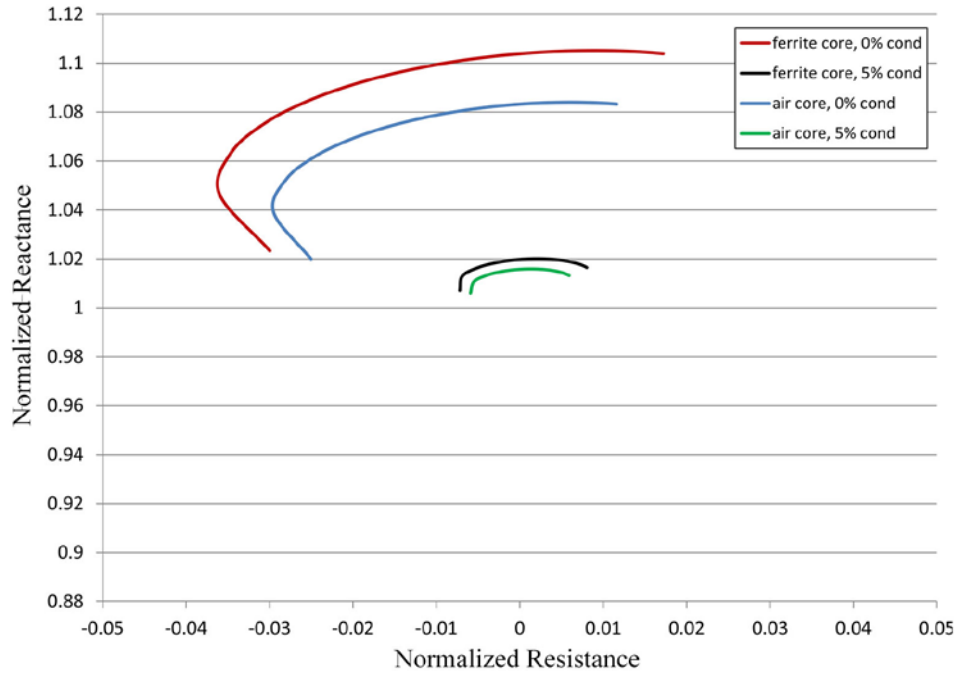


Figure C.3. Impedance Plane Response for 8.4 mm Deep Rectangular Notches with 3:1 Aspect Ratio and 150 μm Width Over Frequency Range from 5 kHz to 100 kHz in Clockwise Direction

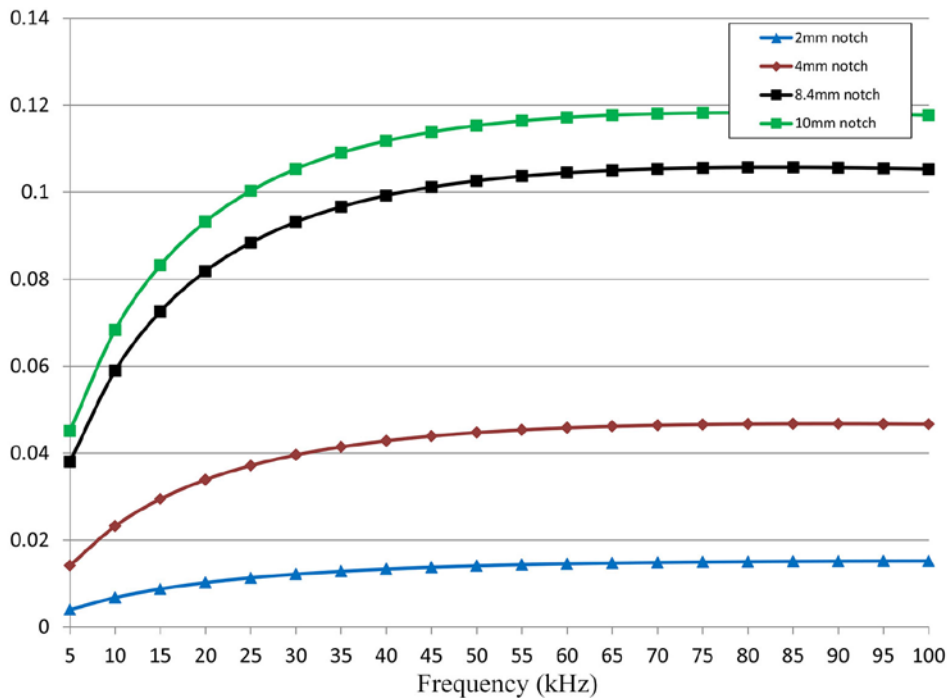


Figure C.4. Change in Normalized Coil Impedance for Ferrite-Core Probe Over Air-Filled Rectangular Notches (0% Conductivity) with 3:1 Aspect Ratio and 150 μm Width

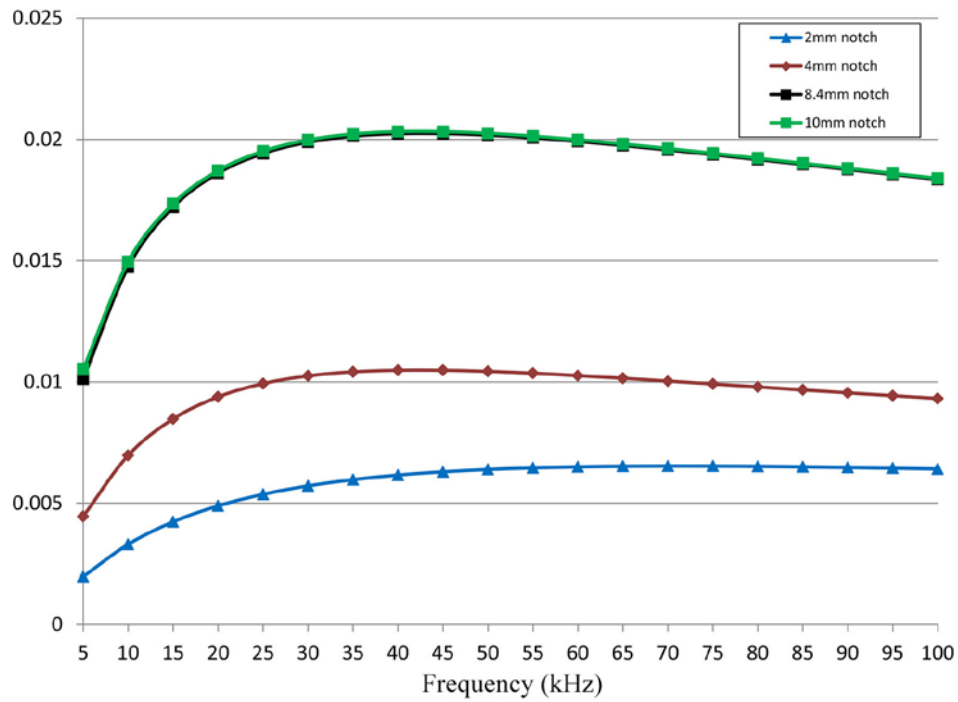
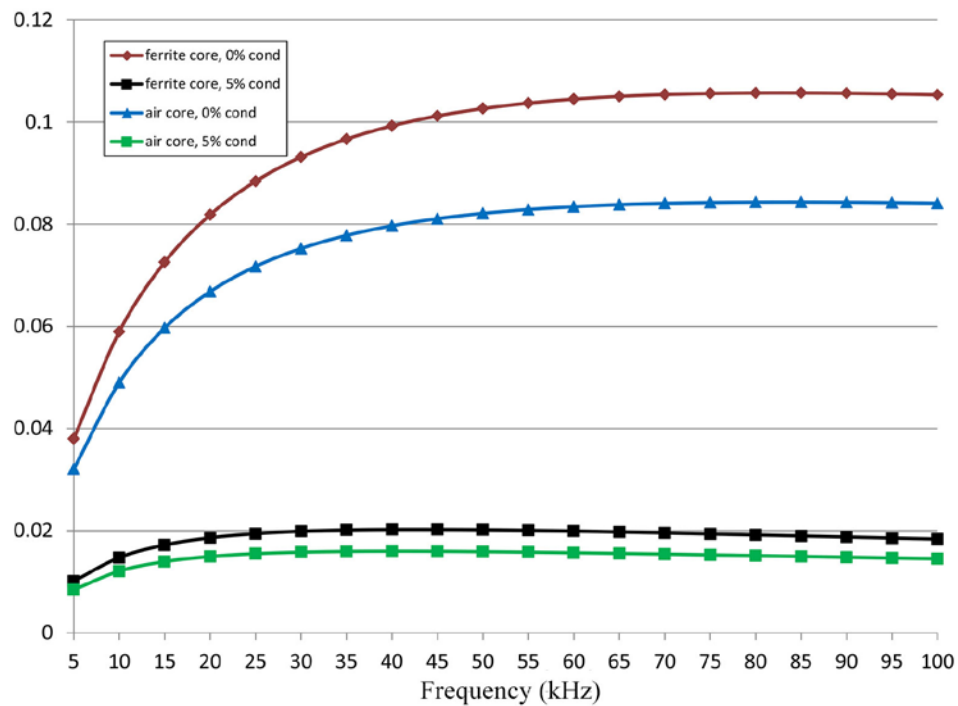


Figure C.5. Change in Normalized Coil Impedance for Ferrite-Core Probe Over Conductive Rectangular Notches (5% Conductivity) with 3:1 Aspect Ratio and 150 μm Width



C.4

Figure C.6. Change in Normalized Impedance for 8.4 mm Deep Rectangular Notches with 3:1 Aspect Ratio and 150 μm Width

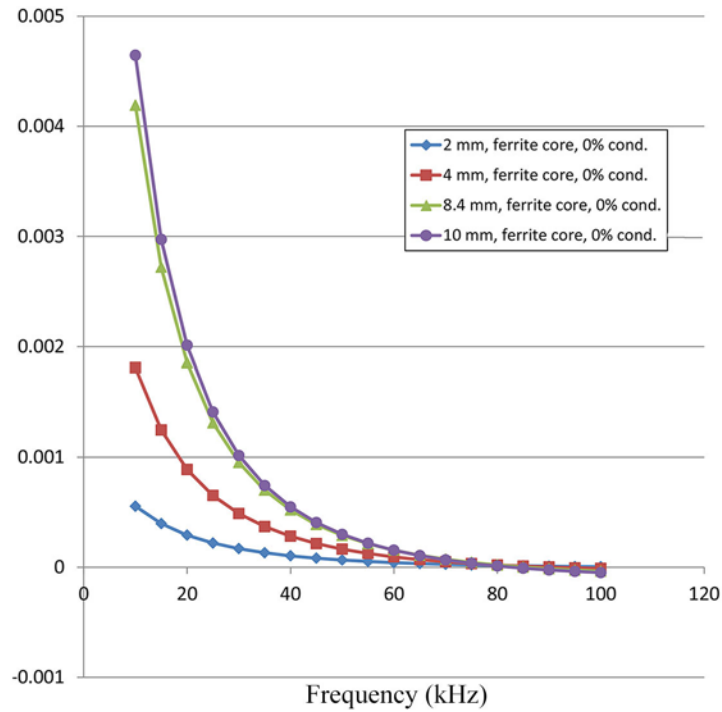


Figure C.7. Derivative of the Change in Normalized Coil Impedance for Ferrite-Core Probe Over Air-Filled Rectangular Notches (0% Conductivity) with 3:1 Aspect Ratio and 150 μm Width

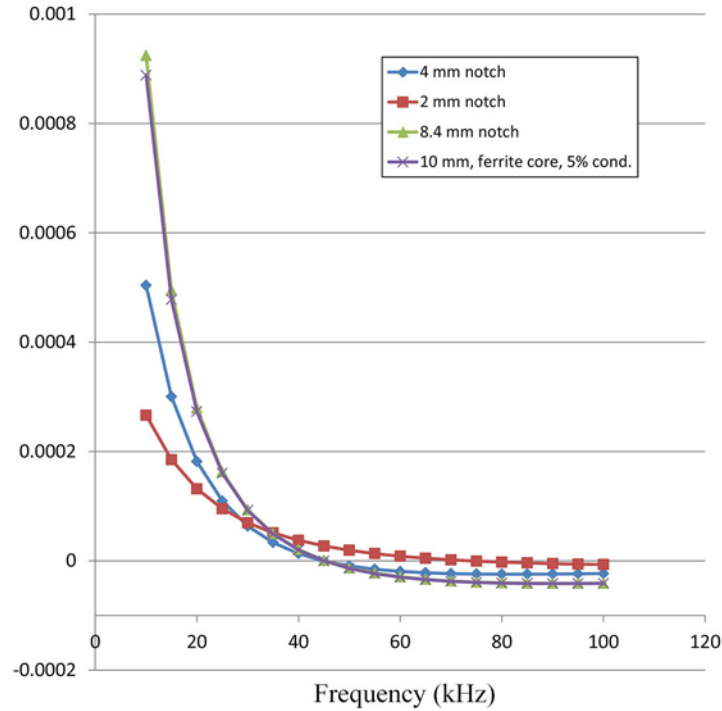


Figure C.8. Derivative of the Change in Normalized Coil Impedance for Ferrite-Core Probe Over Conductive Rectangular Notches (5% Conductivity) with 3:1 Aspect Ratio and 150 μm Width

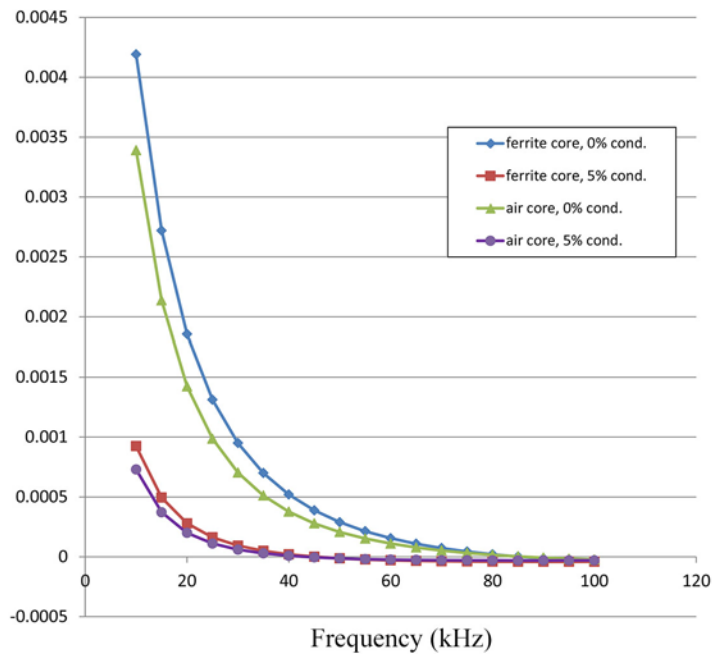


Figure C.9. Derivative of the Change in Normalized Coil Impedance for 8.4 mm Deep Rectangular Notches with 3:1 Aspect Ratio and 150 μm Width

C.6

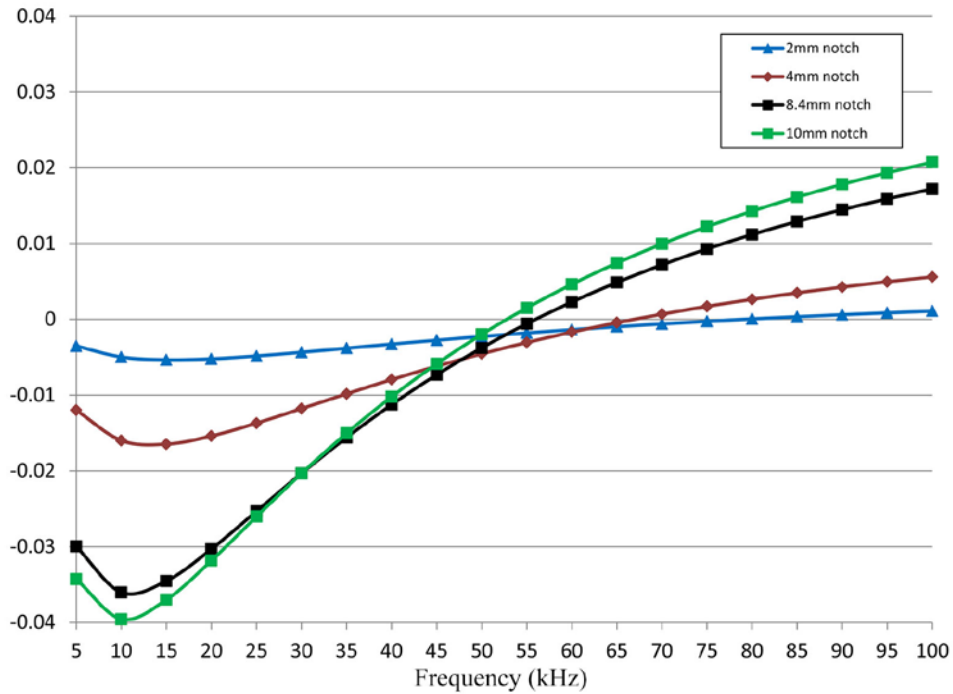


Figure C.10. Change in Normalized Coil Resistance for Ferrite-Core Probe Over Air-Filled Rectangular Notches (0% Conductivity) with 3:1 Aspect Ratio and 150 μm Width

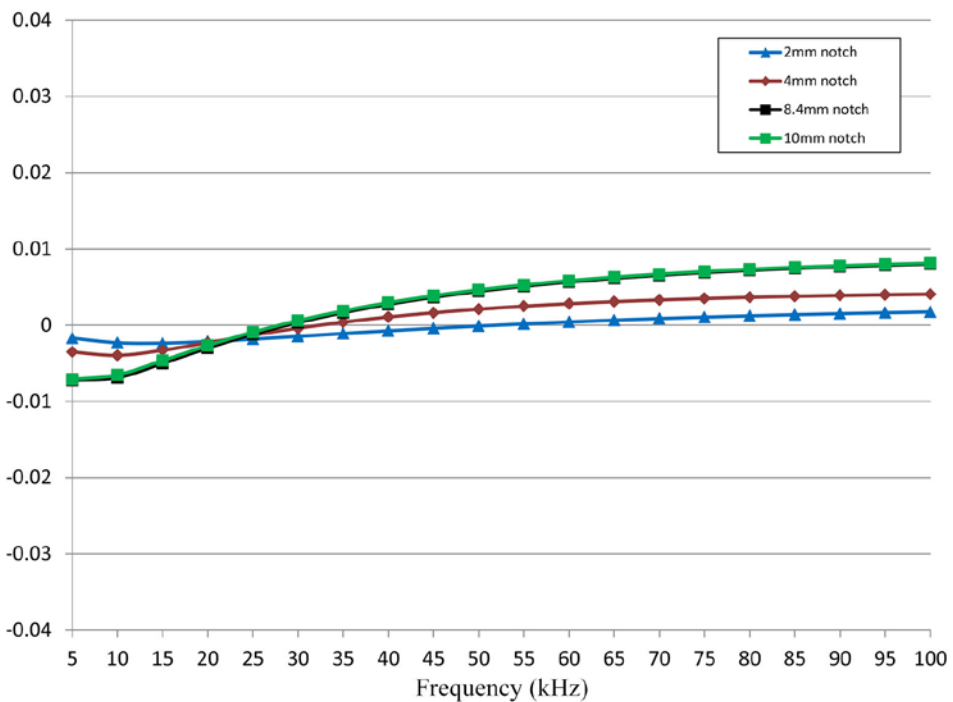


Figure C.11. Change in Normalized Coil Resistance for Ferrite-Core Probe Over Conductive Rectangular Notches (5% Conductivity) with 3:1 Aspect Ratio and 150 μm Width

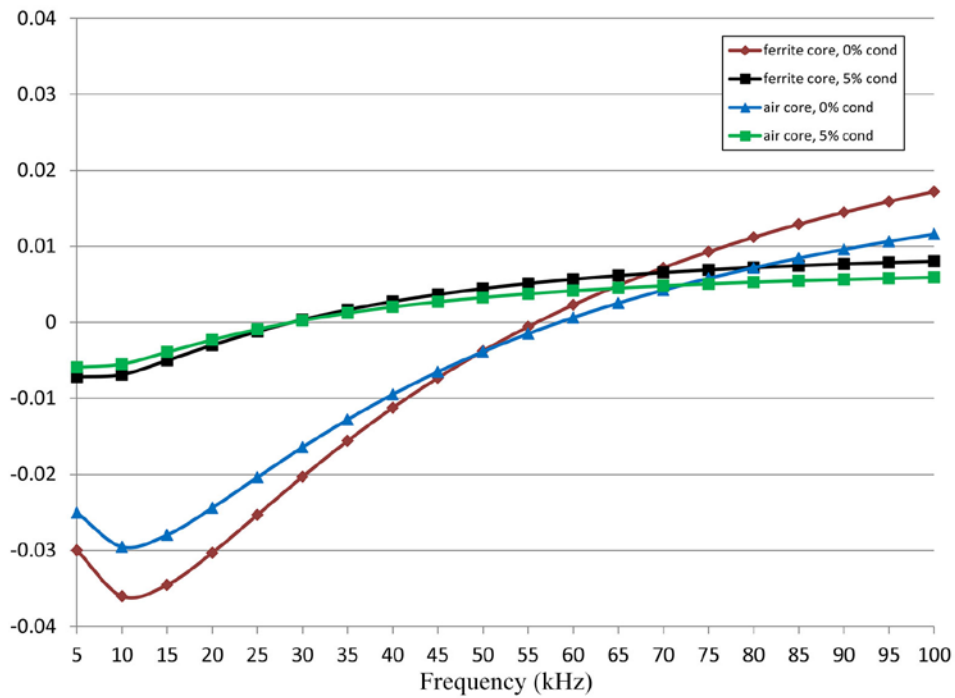


Figure C.12. Change in Normalized Coil Resistance for 8.4 mm Deep Rectangular Notches with 3:1 Aspect Ratio and 150 μ m Width

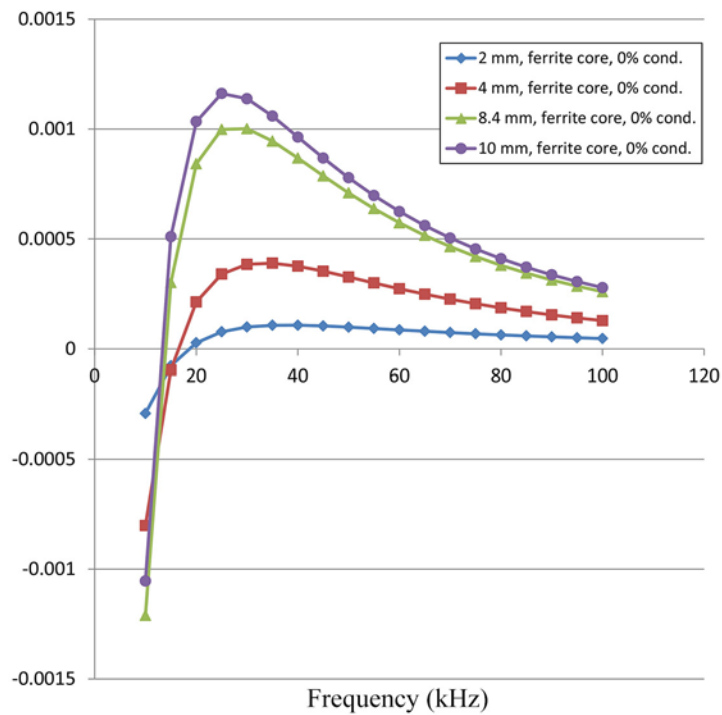


Figure C.13. Derivative of the Change in Normalized Coil Resistance for Ferrite-Core Probe Over Air-Filled Rectangular Notches (0% Conductivity) with 3:1 Aspect Ratio and 150 μ m Width

C.8

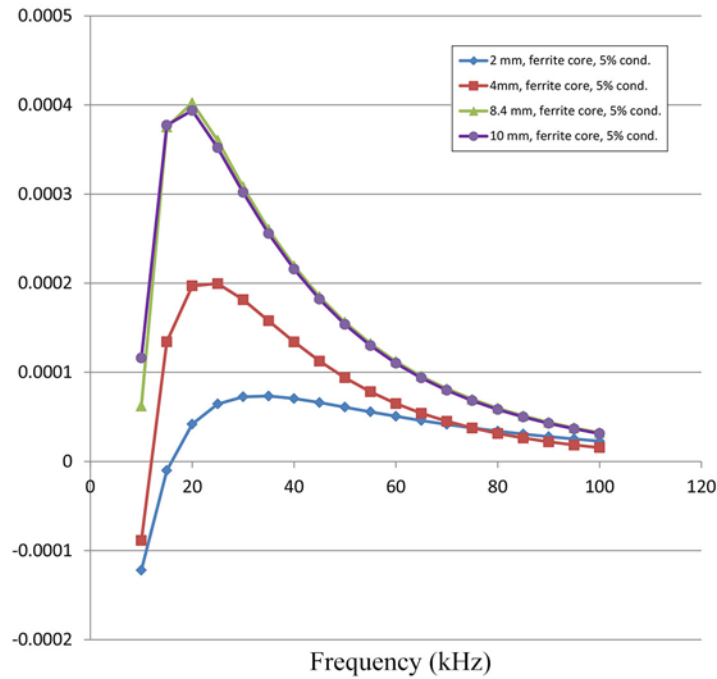


Figure C.14. Derivative of the Change in Normalized Coil Resistance for Ferrite-Core Probe Over Conductive Rectangular Notches (5% Conductivity) with 3:1 Aspect Ratio and 150 μm Width

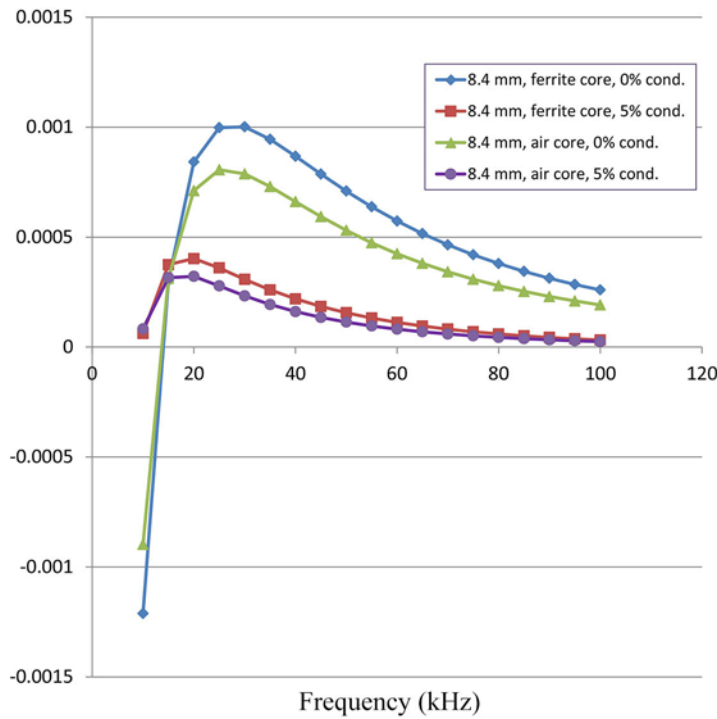


Figure C.15. Derivative of the Change in Normalized Coil Resistance for 8.4 mm Deep Rectangular Notches with 3:1 Aspect Ratio and 150 μm Width

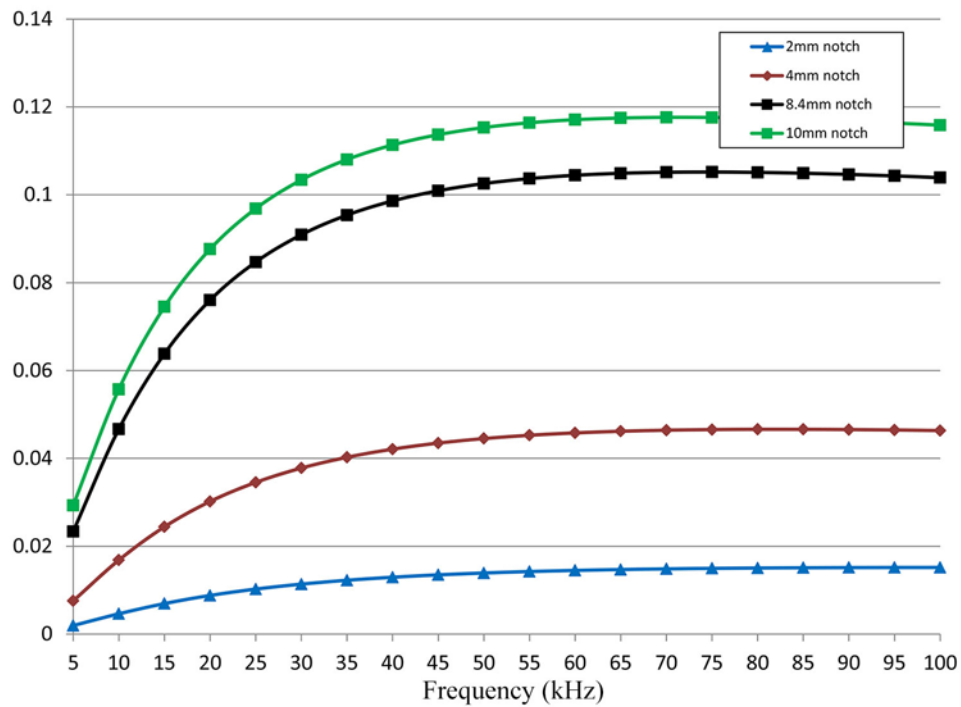


Figure C.16. Change in Normalized Coil Reactance for Ferrite-Core Probe Over Air-Filled Rectangular Notches (0% Conductivity) with 3:1 Aspect Ratio and 150 μm Width

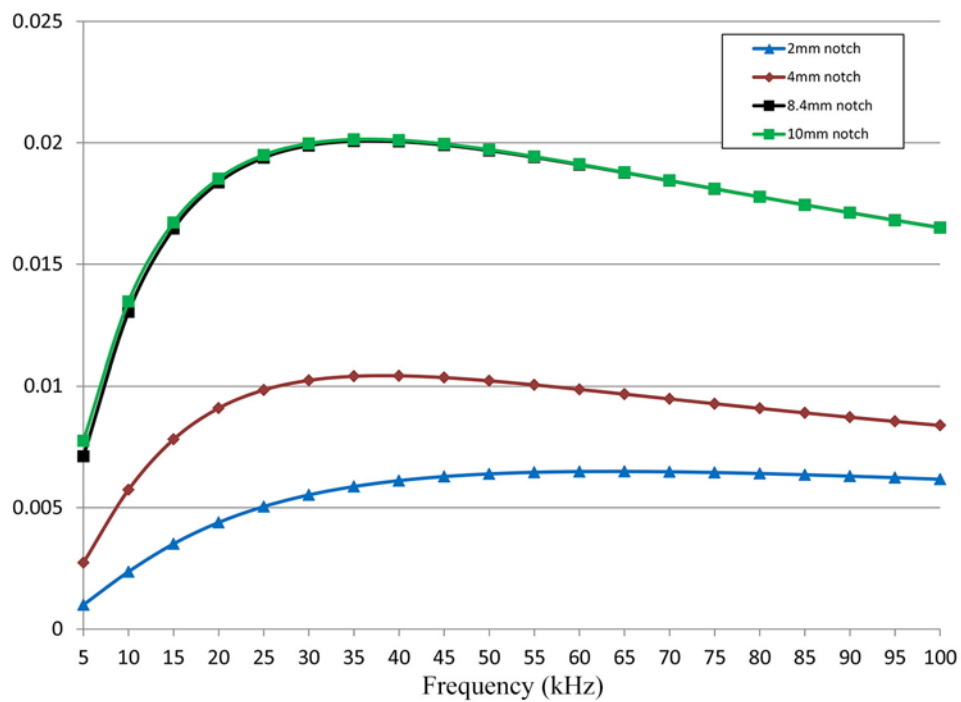


Figure C.17. Change in Normalized Coil Reactance for Ferrite-Core Probe Over Conductive Rectangular Notches (5% Conductivity) with 3:1 Aspect Ratio and 150 μm Width

C.10

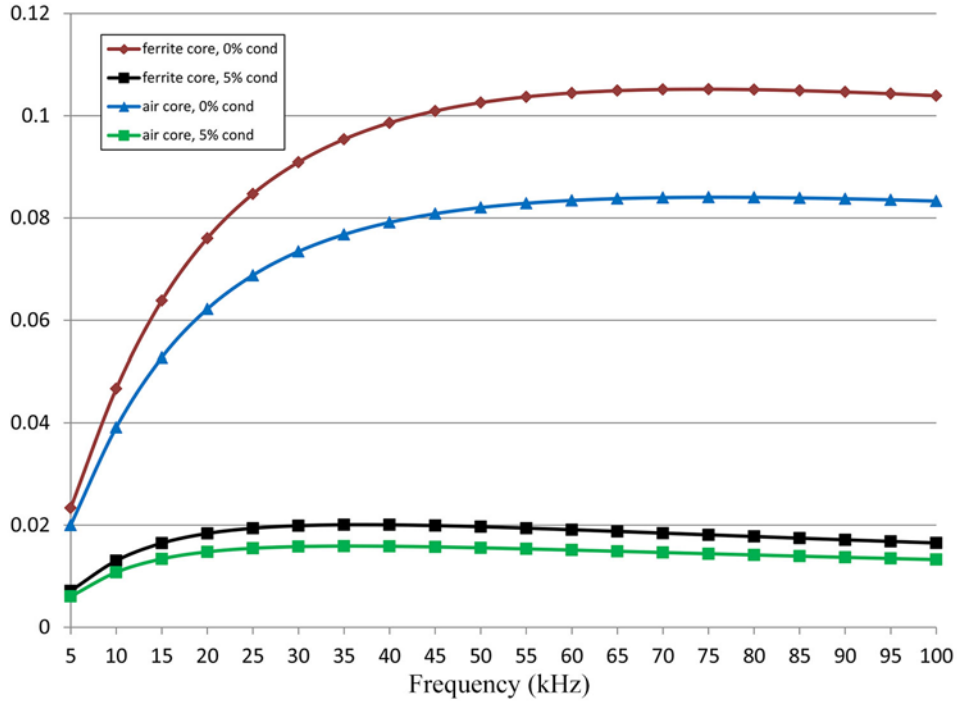


Figure C.18. Change in Normalized Coil Reactance for 8.4 mm Deep Rectangular Notches with 3:1 Aspect Ratio and 150 μm Width

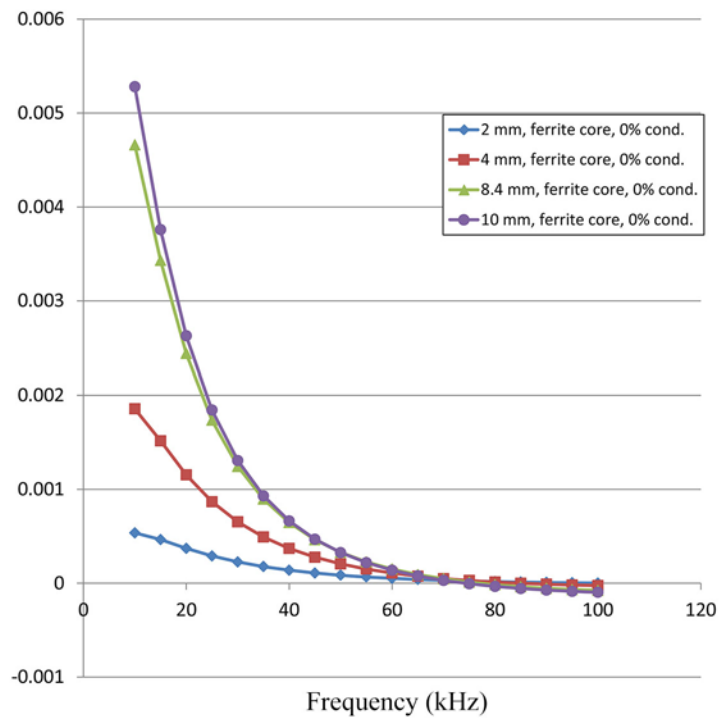


Figure C.19. Derivative of the Change in Normalized Coil Reactance for Ferrite-Core Probe Over Air-Filled Rectangular Notches (0% Conductivity) with 3:1 Aspect Ratio and 150 μm Width

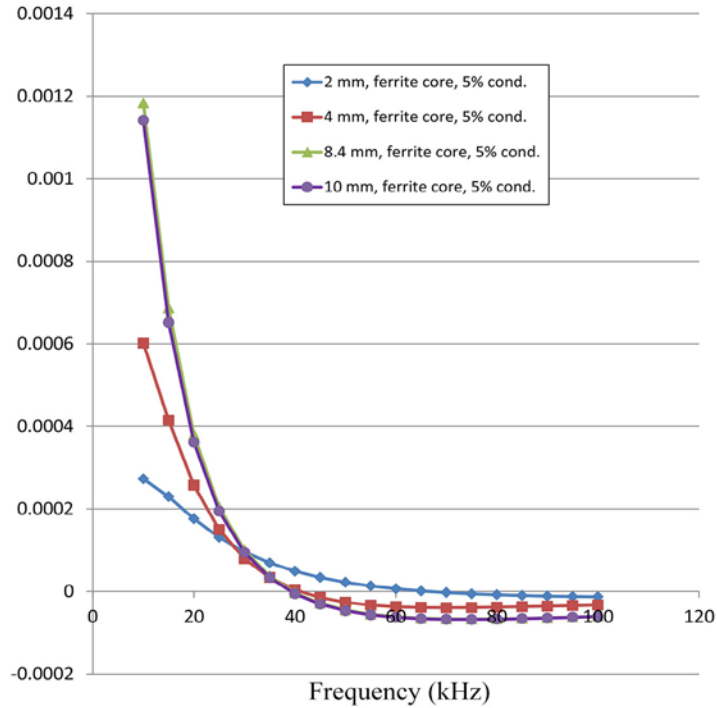


Figure C.20. Derivative of the Change in Normalized Coil Reactance for Ferrite-Core Probe Over Conductive Rectangular Notches (5% Conductivity) with 3:1 Aspect Ratio and 150 μm Width

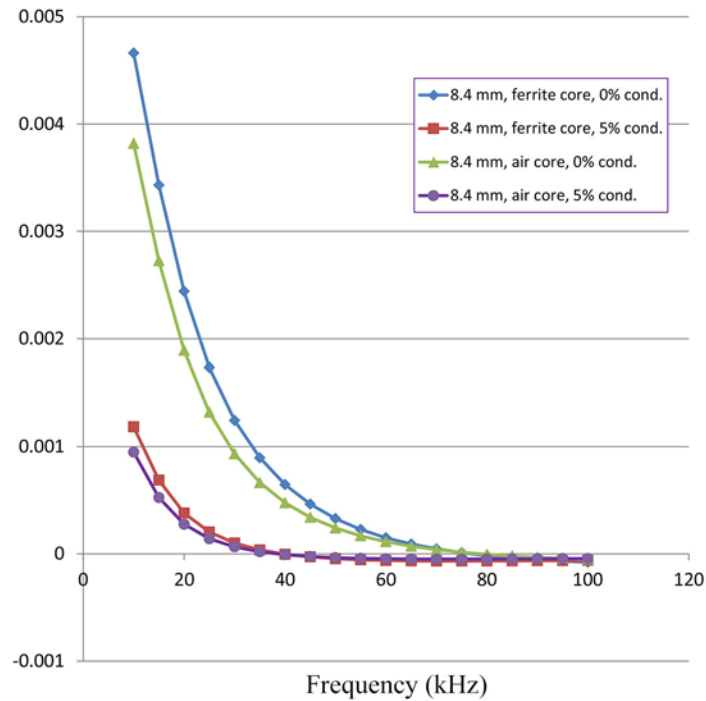


Figure C.21. Derivative of the Change in Normalized Coil Reactance for 8.4 mm Deep Rectangular Notches with 3:1 Aspect Ratio and 150 μm Width

C.12

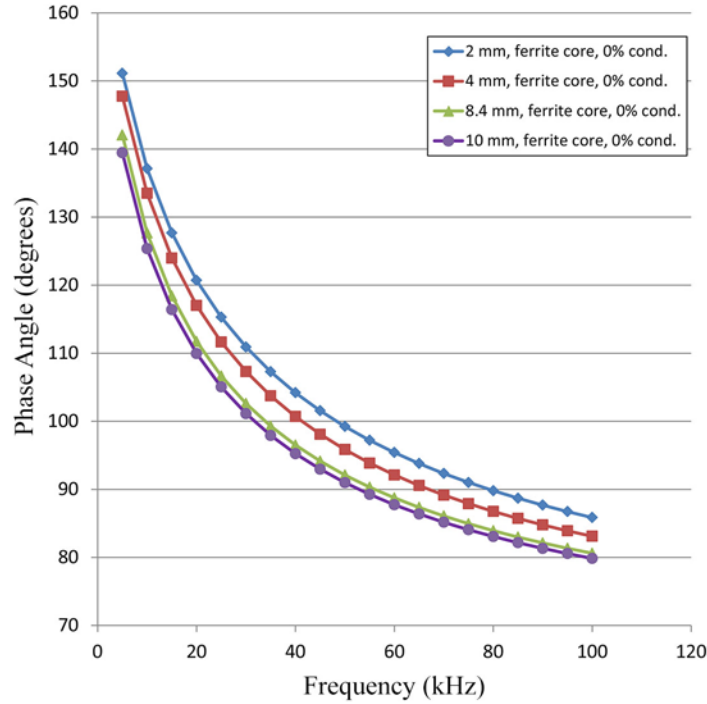


Figure C.22. Phase Angle of Change in Normalized Coil Impedance for Ferrite-Core Probe Over Air-Filled Rectangular Notches (0% Conductivity) with 3:1 Aspect Ratio and 150 μm Width

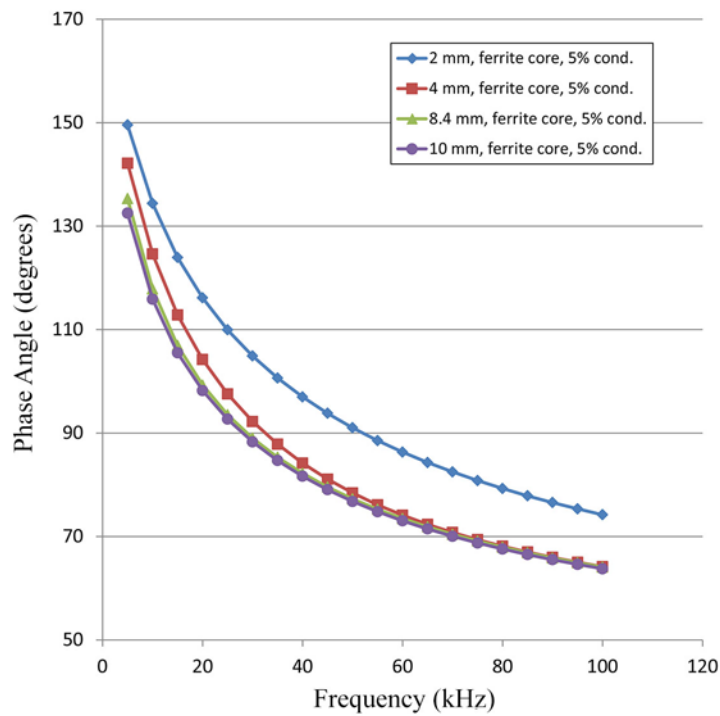


Figure C.23. Phase Angle of Change in Normalized Coil Impedance for Ferrite-Core Probe Over Conductive Rectangular Notches (5% Conductivity) with 3:1 Aspect Ratio and 150 μm Width

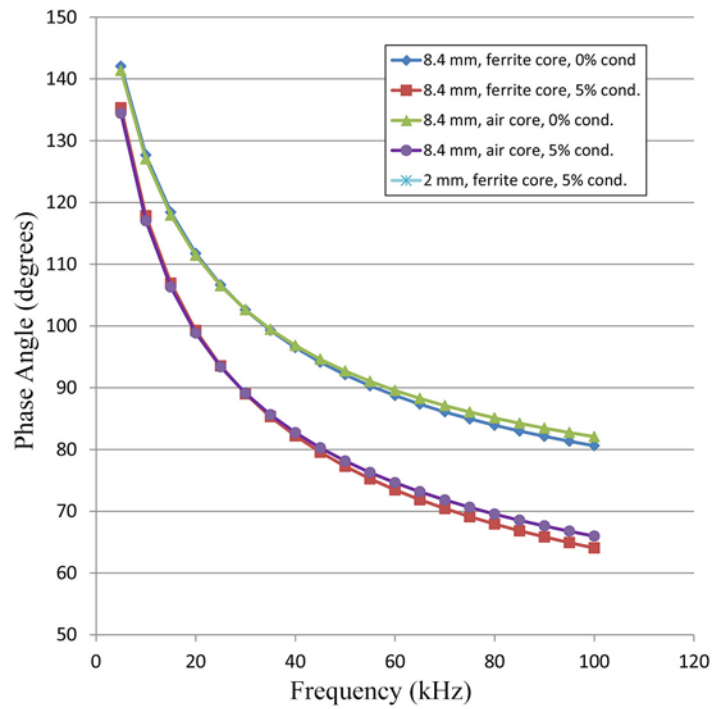


Figure C.24. Phase Angle of Change in Normalized Coil Impedance for 8.4 mm Deep Rectangular Notches with 3:1 Aspect Ratio and 150 μ m Width

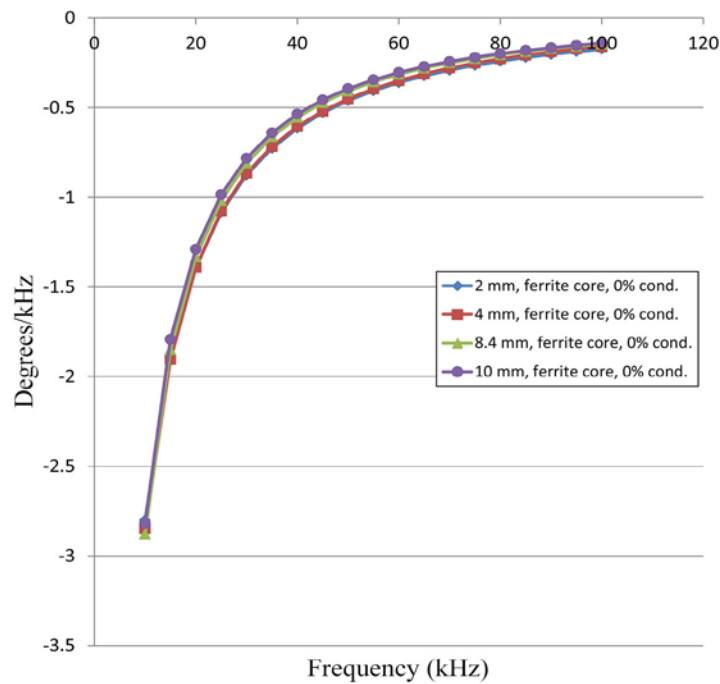


Figure C.25. Derivative of Phase Angle of Change in Normalized Coil Impedance for Ferrite-Core Probe Over Air-Filled Rectangular Notches (0% Conductivity) with 3:1 Aspect Ratio and 150 μ m Width

C.14

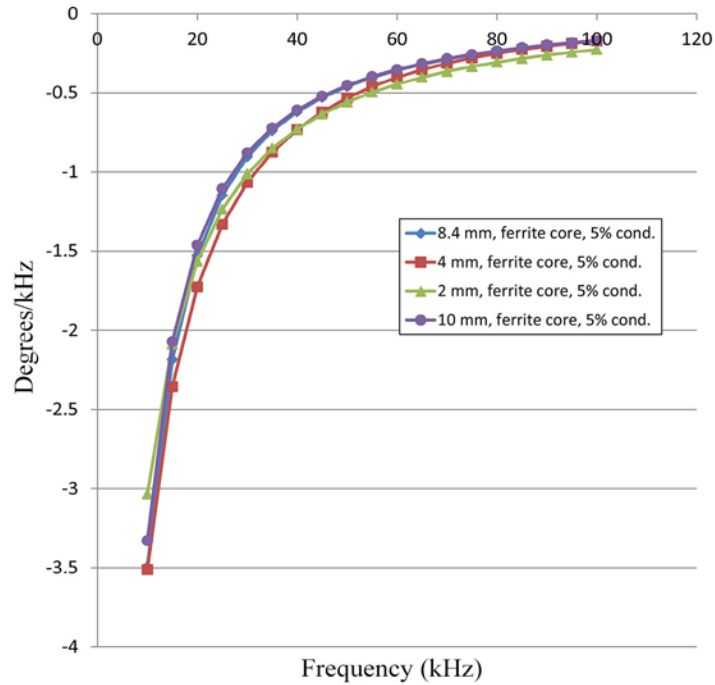


Figure C.26. Derivative of Phase Angle of Change in Normalized Coil Impedance for Ferrite-Core Probe Over Conductive Rectangular Notches (5% Conductivity) with 3:1 Aspect Ratio and 150 μm Width

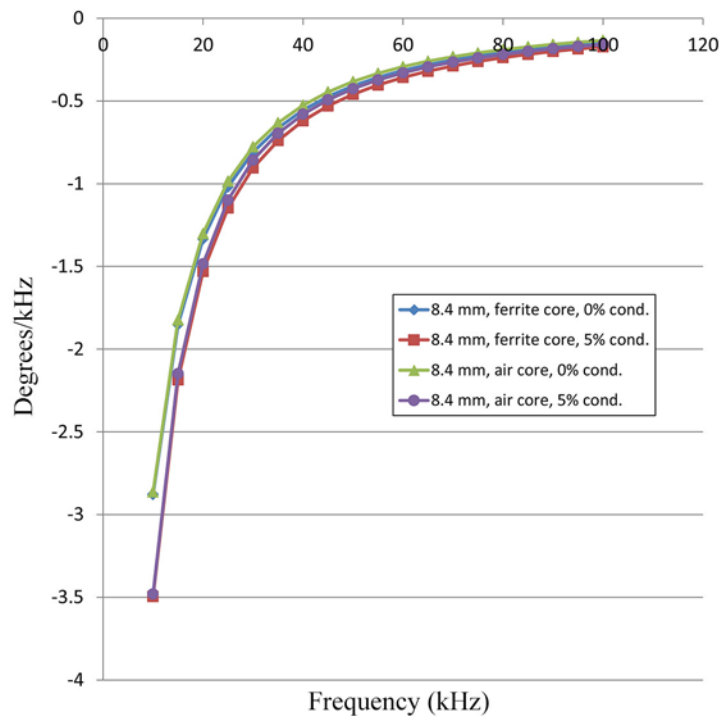


Figure C.27. Derivative of Phase Angle of Change in Normalized Coil Impedance for 8.4 mm Deep Rectangular Notches with 3:1 Aspect Ratio and 150 μm Width

Appendix D: Zr-4 Tube Specimens

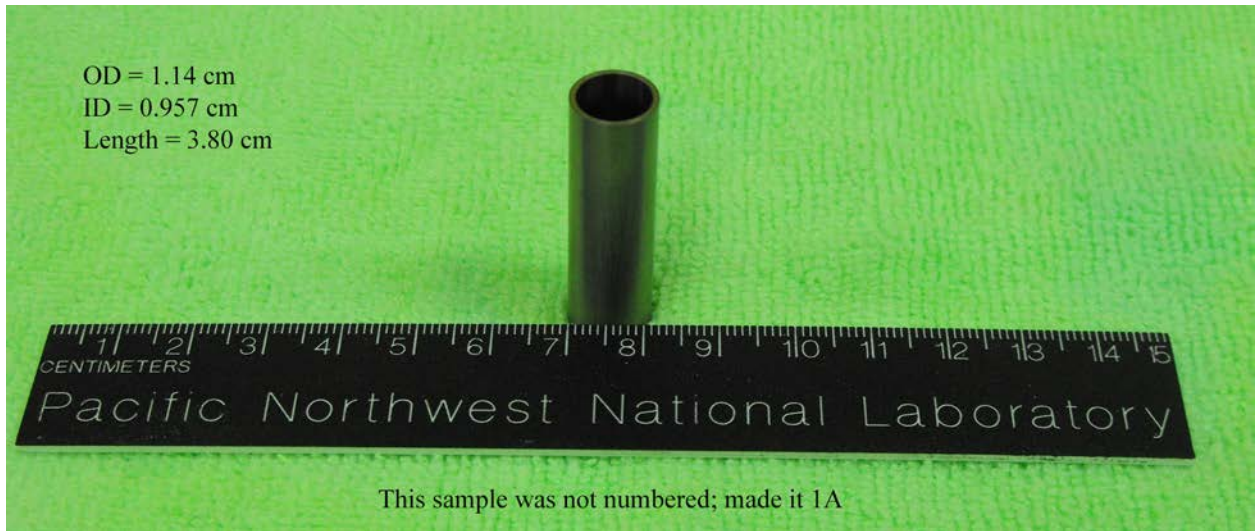


Figure D.1. Photograph of Zr-4 Tube Specimen 1A (vertical orientation)

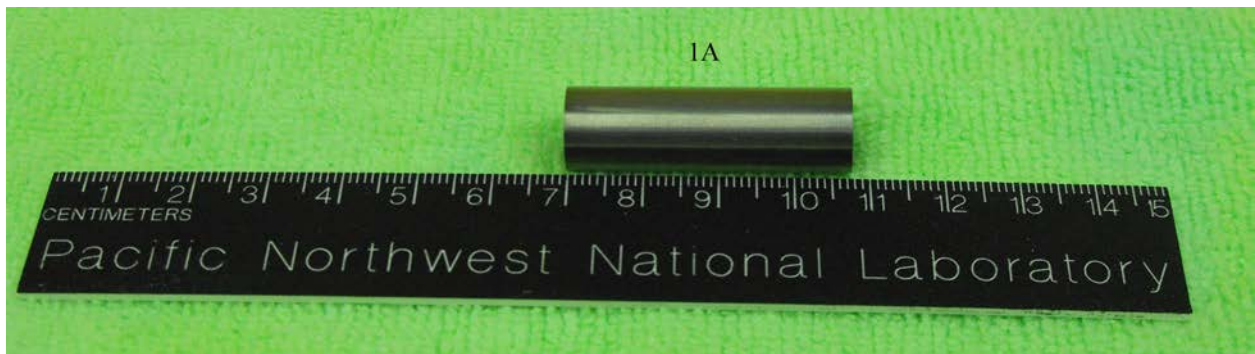


Figure D.2. Photograph of Zr-4 Tube Specimen 1A (horizontal orientation)

D.2



Figure D.3. Photograph of Zr-4 Tube Specimen 2A (vertical orientation)



Figure D.4. Photograph of Zr-4 Tube Specimen 2A (horizontal orientation)

Distribution

**No. of
Copies**

- # Name
Organization
Address
City, State and ZIP Code
- # Organization
Address
City, State and ZIP Code
 - Name
 - Name
 - Name
 - Name (#)
- # Name
Organization
Address
City, State and ZIP Code

**No. of
Copies**

- # **Foreign Distribution**
 - # Name
Organization
Address
Address line 2
COUNTRY
- # **Local Distribution**
 - Pacific Northwest National Laboratory
 - Name Mailstop
 - Name Mailstop
 - Name Mailstop
 - Name Mailstop
 - Name (PDF)

